Dissertation
zur Erlangung des Doktorgrades
der Mathematisch-Naturwissenschaftlichen Fakultät
der Christian-Albrechts-Universität zu Kiel

Geophysical methods for the investigation of soils

vorgelegt von

Tina Wunderlich

Kiel, 2012

Christian-Albrechts-Universität zu Kiel
Institut für Geowissenschaften

Referent: Prof. Dr. W. Rabbel
Koreferent: Prof. Dr. H.-J. Götze
Tag der mündl. Prüfung: 19.4.2012
Zum Druck genehmigt: 19.4.2012

Der Dekan

Abstract

In-field variability of soil parameters such as clay and water content is of interest in agriculture and soil science. Geophysical measurements using multi-sensor platforms can be used to determine the variability of geophysical parameters with high resolution time and cost efficiently. To transform the geophysical parameters into soil parameters of interest so-called geophysical pedotransfer functions (GPTFs) are used.

The aim of the work at hand is the development and enhancement of geophysical processing techniques for pedological mapping. The work is concentrating on (1) the applicability of known and the development of new GPTFs using laboratory measurements under controlled conditions, (2) the areal mapping of the electrical conductivity of topsoil and subsoil using an inversion, (3) the separation of the influences of water and clay content on the electrical conductivity and (4) the development and first application of approaches for pedological mapping with geophysical methods.

With regard to (1) there are already several GPTFs linking electrical conductivity and permittivity to clay and volumetric water content available in literature. Validation of these models using data measured under controlled conditions in laboratory showed that the simple empirical and volumetric mixing models yield good agreement between model and data. Complicated effective medium models that incorporate pore-scale geometrical features are only slightly better with respect to the RMS error. Furthermore a linear relationship between electrical conductivity and permittivity was observed, which can be used successfully to determine the permittivity distribution from an inverted geoelectric profile. The resulting velocity distribution shows good agreement with in-situ measured velocity. Additional data from laboratory measurements are the waveforms of GPR reflections. Their shape and amplitude are strongly dependent on clay and water content of the soil. For increasing clay and water content a frequency downshift was observed that can be described with a simple theoretical model. Using the spectral ratio of a reference wavelet and the reflection leads to the determination of the quality factor. Its relationship with clay and water content can be described by a logarithmic multivariate function. Based on this the imaginary part of permittivity can be determined, which is a measure of the loss due to polarisation relaxation. The relationship between the real and imaginary part of permittivity can be described by a linear function whose slope is dependent on clay content only. Therefore this relationship can be used to determine the clay content of a soil if both parts of permittivity are known.

Point (2) uses a widely applied geophysical instrument, the EM38DD, that measures the apparent electrical conductivity as an integral value within the depth interval from 0 to about 1.5 m. Using an inversion of EMI data measured in two heights and in two coil orientations the electrical conductivities of two layers and the depth of the interface between the layers can be determined. Regularisation of the inversion is done through a priori information. The results show good agreement with geoelectric profiles.

Concerning (3), the inverted spatial variations of the electrical conductivity of the topsoil and the spatial variations of measured radioelement concentrations of Uranium and Thorium are used to determine patterns of clay and water content using principal component analysis.

In (4) the above mentioned points are combined to yield areal variations of water and clay content based on geophysical data. The inverted electrical conductivity of single layers is the basis and together with additional data such as GPR or geoelectric profiles the tested and developed GPTFs from (1) are applied. A comparison of different methods showed that the distribution of water content is determined similar with all methods and that the values differ by maximal 10 %, whereas the quantitative prediction of clay content suffers from problems during the determination of the quality factor.

Zusammenfassung

Die Variation von Bodenparametern innerhalb eines Feldes, wie z. B. Wasser- und Tongehalt, ist in Landwirtschaft und Bodenkunde von Interesse. Die flächenhafte Variation von geophysikalischen Parametern kann durch geophysikalische Messungen mit Multi-Sensor Plattformen in hoher Auflösung schnell und kostengünstig bestimmt werden. Um von den gemessenen geophysikalischen Parametern auf die gewünschten Bodenparameter zu schließen, müssen sogenannte geophysikalische Pedotransfer-Funktionen (GPTFs) benutzt werden.

Das Ziel der vorliegenden Arbeit ist die Entwicklung und Verbesserung geophysikalischer Auswertemethoden zur flächenhaften bodenkundlichen Kartierung. Dabei konzentriert sich die Arbeit auf (1) die Anwendbarkeit von bekannten und die Entwicklung von neuen GPTFs anhand von Labormessungen unter kontrollierten Bedingungen, (2) die flächenhafte Kartierung der elektrischen Leitfähigkeit von Ober- und Unterboden mit Hilfe einer Inversion, (3) die flächenhafte Trennung von Wassergehalts- und Tongehaltseinfluss auf die elektrische Leitfähigkeit und (4) die Entwicklung und erste Anwendung von Ansätzen zur bodenkundlichen Kartierung mit Hilfe geophysikalischer Methoden.

In Bezug auf (1) sind in der Literatur bereits einige GPTFs zu finden, die den Zusammenhang zwischen elektrischer Leitfähigkeit und Dielektrizitätszahl und Wasser- und Tongehalt beschreiben. Die Anwendung von diesen Modellen auf unter kontrollierten Bedingungen gemessenen Labordaten zeigt, dass die relativ einfachen empirischen und volumetrischen Mischungsmodelle gute Übereinstimmung zwischen Messwerten und Modell liefern. Kompliziertere effektive Medien-Modelle, die auch geometrische Eigenschaften auf Porengrößenskala einschließen, ergeben nur eine geringe Verbesserung des RMS Fehlers. Des Weiteren wurde ein linearer Zusammenhang zwischen elektrischer Leitfähigkeit und Dielektrizitätszahl beobachtet, der erfolgreich dazu benutzt werden kann, aus einem invertierten Geoelektrikprofil die Verteilung der Dielektrizitätszahlen zu bestimmen. Die daraus resultierende Geschwindigkeit stimmt gut mit in-situ gemessenen Geschwindigkeiten überein. Zusätzliche Informationen können aus den Wellenformen und Amplituden der im Labor gemessenen GPR Reflektionen gezogen werden, da diese stark abhängig von Wasser- und Tongehalt sind. Mit zunehmendem Ton- und Wassergehalt wurde eine Frequenzerniedrigung beobachtet, die mit einem einfachen theoretischen Modell beschrieben werden kann. Mit Hilfe der Spektrendivision von Referenz- und reflektierter Wellenform kann der Qualitätsfaktor bestimmt werden, dessen Zusammenhang mit Wasser- und Tongehalt durch eine logarithmische multivariate Funktion beschrieben werden kann. Ausgehend davon wird dann der Imaginärteil der Dielektrizitätszahl berechnet werden, der die Verluste im Zuge der Polarisationsrelaxation beschreibt. Der Zusammenhang zwischen Real- und Imaginärteil der Dielektrizitätszahl kann durch eine lineare Funktion beschrieben werden, deren Steigung nur vom Tongehalt abhängt. Also kann diese Beziehung benutzt werden um den Tongehalt zu bestimmen, falls beide Teile der Dielektrizitätszahl bekannt sind.

In (2) werden die Messungen eines häufig eingesetzten Messgeräts, des EM38DD, untersucht. Es misst einen integralen Wert der scheinbaren elektrischen Leitfähigkeit zwischen 0 und ca. 1.5 m Tiefe. Mit einer Inversion von Messdaten, die mit zwei Spulenorientierungen und in zwei Höhen gemessen wurden, können die elektrischen Leitfähigkeiten von zwei Schichten und die zugehörige Tiefe der Schichtgrenze bestimmt werden. Die Inversion wird durch a priori Infor-

mationen regularisiert und zeigt gute Übereinstimmung mit geoelektrischen Profilen.

Bezüglich (3) wird die invertierte räumliche Variation der Leitfähigkeit der oberen Schicht und die zusätzlich gemessene räumliche Variation von Uran- und Thorium-Konzentrationen benutzt, um die räumlichen Muster von Wasser- und Tongehalt mit Hilfe der Hauptkomponentenanalyse zu bestimmen.

In (4) treffen die bereits vorgestellten Punkte zusammen, um aus flächenhaften geophysikalischen Daten auf die Verteilung von Wasser- und Tongehalt zu schließen. Die invertierte elektrische Leitfähigkeit der einzelnen Schichten dient dabei als Grundlage, um zusammen mit zusätzlichen Methoden, wie z.B. Radarmessungen oder geoelektrischen Profilen, und der Anwendung von den unter (1) getesteten und neu entwickelten GPTFs den Wasser- und Tongehalt zu bestimmen. Ein Vergleich unterschiedlicher Methoden zeigt, dass die Verteilung des Wassergehalts mit allen Methoden ähnlich bestimmt wird und die Abweichung bei maximal 10 % liegt, während die quantitative Vorhersage des Tongehaltes durch Probleme bei der Bestimmung des Qualitätsfaktors beeinflusst wird.

Contents

1. Introduction

Soil is a non-renewable resource with fundamental functions (e.g. filtering, storing or transforming of nutrients) that have to be preserved, because they are a basis for the feeding of humans and animals. The quality of soils e.g. for the cultivation of crops is influenced by several factors, such as texture, organic matter, salinity and nutrients, as well as biologic, climatic, topographic and anthropogenic factors, e.g. soil compaction (Corwin and Lesch 2005). The in-field variability of these soil properties is a critical point in agriculture resulting in spatial variation of crop. Using GPS systems and digital harvesting maps in precision agriculture the local amount of fertiliser is optimised. However, this does not give information about the sources of the variability, such as variations in water or clay content.

Soil properties are conventionally determined by taking samples and analysing them in the laboratory. Of course this is time and cost consuming. Additionally, the obtained information about soil properties are representative for single points only, and not for larger volumes.

In contrast, geophysical multi-sensor platforms towed behind a tractor or off-road car can be used to map large areas in short time. Thus, geophysics offers high-resolution maps of geophysical parameters while the soil scientists or farmers require high-resolution maps of soil properties. To translate geophysical parameters into soil parameters the relationships between them have to be known. These relations are manifold and seldom unique, which leads to problems concerning a reliable translation. Some of the assumed relationships between geophysical and soil parameters are listed in Tab. 1.1. Only one geophysically measured parameter, the γ-concentration, has a unique link to a soil parameter, i.e. clay content. All other geophysical parameters are influenced by several soil properties. Thus, there is a need to investigate these relationships and to determine quantitative equations to transform the parameters taking the influences of several soil properties into account.

The investigation and quantification of the assumed relationships was one objective of the iSOIL project („Interactions between soil related sciences, linking geophysics, soil science and digital soil mapping“) in the Seventh Framework Programme of the European Commission. This project included 20 partners (universities, research centres, small and medium enterprises) from 9 European countries with experience in geophysics, soil science and digital soil mapping. The work at hand was done in the framework of the iSOIL project and investigates the relationships between geophysical and soil parameters that are marked in green in Tab. 1.1. The soil properties of interest are the water content, which is closely connected to saturation and porosity, and the clay content.

To investigate these relationships under controlled conditions soil samples were taken and studied in laboratory. The samples were taken from three iSOIL field sites that were chosen to cover a wide range of European soil types. Two of them are located in Germany and one in Czech Republic (Fig. 1.1). After a large-scale geophysical survey measuring the electrical conductivity and radioelement concentration, each five plots (30 x 70 m^2) in Rosslau and Lany and one in Bad Lauchstädt have been selected for detailed geophysical measurements and soil sampling.

Rosslau is located in Saxony-Anhalt north of the river Elbe. The measurement site is part of a floodplain with fluvial sediments covered by grassland. The lower southern part close to the river is dominated by clayey soils, whereas the higher northern part is comprised of sands. One of five plots is located in the sandy part, whereas the others are located in the southern clayey part. Bad Lauchstädt is also located in Saxony-Anhalt and is home of a static fertilisation experiment. Its soil type is Chernozem (Löss-Schwarzerde), having medium clay content. The plot here is located on a fallow land covered by grass. The field site Lany in Czech Republic is located about 30 km west of Prague having the soil type Cambisol. It is the only field site where crops are cultivated. Here again five plots are distributed over the whole field.

For detailed geophysical measurements on the 11 plots a multi-sensor platform was towed behind a tractor or an off-road car. Instruments used were the EM38DD (Geonics Ltd.), a γ-spectrometer (GSCar by GF Instruments), a GPR (Ground Penetrating Radar) system with 400 and 900 MHz antennas (GSSI) and an array of fluxgate magnetometers (Foerster). Additional stationary geoelectric profiles were measured on each plot and TDR (Time Domain Reflectometry) and GPR velocity measurements where applicable. After completion of field measurements large soil samples of about 50 kg were taken from each plot from two depths (10-30 cm and 30-50 cm). In Lany one additional sample was taken from one plot from 0-10 cm depth. Small samples for soil analyses (e.g. texture, organic matter content) were taken by UFZ (Helmholtz Centre for Environmental Research, Leipzig, Germany) at the same plots.

	σ / ρ EMI & Geoelec.	κ_M Magnetics	v / ε GPR	A / α GPR	v_p, v_s Seismics	γ γ-ray spectrometry	τ, c, ρ_0, ρ_∞ SIP
θ (water content)	x		x	x	x		x
S (saturation)	x		x	x	x		x
Φ (porosity)	x		x	x	x		x
ρ_b (density)					x		
TDS (salinity)	x		x	x			
c_{org} (org. content)	x	x	x		x		
c_c (clay content)	x	x	x	x		x	x
FeC (Fe content)		x					
T (temperature)	x						x
κ_h (hydraulic permeability)	x						x

Tab. 1.1: Overview about the assumed relationships between geophysically measured parameters (top row) and soil parameters (left column). The green cells show the relationships that will be considered in the work at hand. (EMI: Electromagnetic induction, GPR: Ground penetrating radar, SIP: Spectral induced polarisation)

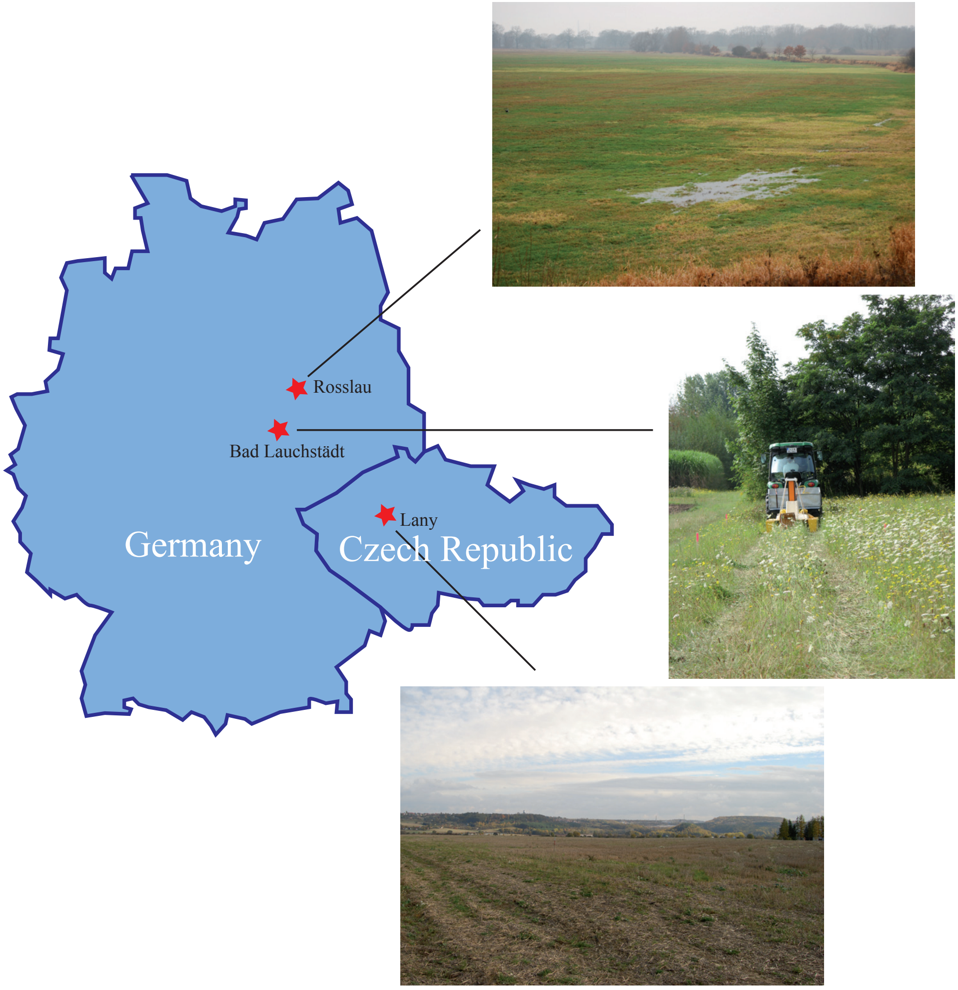

Fig. 1.1: iSOIL field sites in Germany and Czech Republic (Photo of Bad Lauchstädt: Ulrike Werban).

Several so-called geophysical pedo-transfer functions (GPTFs) are already available in literature. Not all of them were originally developed for soils, but for hard rocks, and thus their applicability to soils has to be examined.

The prediction of water content from electrical conductivity and dielectric permittivity is the aim of chapter 2. Here the soil samples, having different clay contents, will be used to conduct geophysical measurements under controlled saturation conditions in the laboratory. The influence of the clay content on both geophysical parameters is explicitly incorporated in some of the examined relationships, whereas others have fitting parameters to match different soil textures.

Another approach to determine water and clay content from geophysical measurements is the use of the waveforms and amplitudes of GPR reflections, because both are strongly influenced by water and clay content. This is presented in chapter 3, also based on the laboratory measurements on large soil samples.

If suitable GPTFs were found, the next step would be the transition from controlled laboratory conditions to areal field measurements. A widely applied method to measure the electrical conductivity on large areas is the use of the electromagnetic induction instrument EM38DD. Its output is the apparent electrical conductivity measured as an integral value within the depth interval from 0 to about 1.5 m. However, the electrical conductivities of topsoil and subsoil might be significantly different from the measured integral value. To assign an electrical conductivity value to a certain depth interval, e.g. of the topsoil, an inversion can be used. The inversion takes measurements of apparent electrical conductivities in different configurations as input and determines the electrical conductivities of topsoil and subsoil and the depth of the interface between the layers (Chapter 4). The resulting maps of electrical conductivity can then be transformed into maps of soil parameters using GPTFs.

The calculation of clay content maps can be supported by the unique relationship between clay content and γ-concentrations. This direct link is not part of the study at hand, but it can be used implicitly for the separation of the influences of water and clay content on the electrical conductivity. This is done by assuming that the electrical conductivity is influenced by water and clay content, whereas the γ-concentration is affected by the clay content only (Tab. 1.1). A decomposition of maps of electrical conductivity and radioelement concentrations into principal and independent components leads to maps of relative water and clay content distributions, which are shown in chapter 5. Because the radioelement concentrations are representative for the uppermost 30 cm of the soil, the inverted electrical conductivity of the topsoil is used.

Chapter 6 gives proposals about the application of the investigated GPTFs on large-scale field data to determine maps of water and clay content. The basis for all transformations is the areal map of electrical conductivity derived by the EMI inversion. With the help of additional information by GPR and geoelectrical profiles the examined and developed GPTFs are used to calculate maps of water and clay content.

Taking soil samples at several points and determining the clay and water content will be needed for the evaluation and calibration of the resulting maps. Also in-situ measurements of electrical conductivity in shallow boreholes will be helpful for ground-truthing.

Chapter 7 gives a summary of the results of this study and a short outlook on the points that need to be further investigated.

2. Geophysical pedo-transfer functions relating electrical conductivity and permittivity to water content

2.1 Introduction

In soil sciences and agriculture there is a strong need to map e.g. the water and clay content of soils on large scales with relatively high resolution time and cost efficiently. The standard way of this sort of investigation is to take soil samples and analyse their texture in laboratory. To measure water content TDR (time domain reflectometry) sensors applied in situ are widely used. Nevertheless, covering large areas with these point measurements is time consuming. Additionally, the soil properties of interest are only available at discrete points and give no information about larger volumes. Geophysical measurements can in turn cover large areas relatively fast using mobile platforms, where even several sensors can be applied simultaneously. But the problem is then the conversion from geophysically measured parameters to the soil parameters of interest, e.g. clay and water content. Therefore, one of the tasks of iSOIL was the development of geophysical pedo-transfer functions (GPTFs) to describe the relationship between the parameters.

These relationships are not unique, e.g. the electrical conductivity is dependent on several factors such as water content, clay content, temperature and salinity (Tab. 1.1). Increasing water content increases the bulk electrical conductivity of the soil because water has high electrical conductivity due to ionic conductivity from dissolved solids. In addition, if this water has higher salinity, i.e. more dissolved solids, it increases the conductivity even stronger. This is also true for higher temperatures, whereas this influence might be neglected on a field scale in Middle Europe with moderate climate. The clay content of a soil leads to an additional increase of the electrical conductivity, because clays have a surface conductivity due to their large surface area with electrical double layers (Taylor and Barker 2006).

Several GPTFs are already available in literature describing the relationship between soil and geophysical parameters. However, some have not been developed for soils, but rather for rocks that is the material present in oil industry applications.

This chapter focuses on the relationships between electrical conductivity, permittivity and water content. The influence of the clay content is explicitly or implicitly included in some models by additional parameters.

The aim of this chapter is to evaluate the applicability of these relationships to soils using measurements under controlled conditions in the laboratory. It is tested if they can be used reliably to predict the water content from geophysical measurements for various soil textures that are representative for middle Europe. The measurement procedure will be described in the next section followed by a review and application of some of the models (GPTFs) that are available in literature. Based on the application of existing models a best-fitting model will be developed and the results will be applied to field data.

2.2 Methodology

2.2.1 Geophysical measurements

For the iSOIL project three sites with different soil textures were chosen for investigation (see chapter 1 for details of the sites). In Rosslau and Lany five plots à 70 x 30 m^2 and in Bad Lauchstädt one plot were selected for detailed geophysical measurements. On these 11 plots in situ measurements of γ-spectrometry, EM38DD, magnetics, GPR and geoelectrics were conducted. Small soil samples were taken and analysed amongst others with respect to texture, CEC (cation exchange capacity) and C_{org} (organic carbon content). Additionally we took large soil samples from each plot from two depths (10-30 cm and 30-50 cm). In Lany one extra sample from 0-10 cm depth was collected. The texture of the 23 samples can be displayed in a soil texture diagram and based on this differentiated into 4 groups (Fig. 2.1). A second factor for the classification into groups should also be the type of clay minerals, but unfortunately this information is not available.

The 23 soil samples were dried at room temperature and crumbled to obtain homogeneous soil samples. For the laboratory measurements a plastic cylinder was constructed with a height of 75 cm and a diameter of 23.5 cm. Plate electrodes, made from stainless steel, were attached at bottom and top, and at 1/3 and 2/3 of the cylinder height ring electrodes were installed (Fig. 2.2a). When the sample is inside the cylinder the plate electrodes are applied for current injection and the voltage is measured between the ring electrodes. The specific electrical resistivity ρ can be determined by

$$\rho = \frac{U}{I} \cdot \frac{A}{L} \quad , \tag{2.1}$$

where U is the voltage, I the current, A the circular surface area ($A = \pi \cdot (d/2)^2$) and L=25 cm the distance between the ring electrodes. The electrical conductivity is the reciprocal of ρ. In order to suppress electrode polarization effects the resistivity measurements were performed with alternating current of 55 Hz. Previous independent test measurements had shown that this frequency is so low that the resulting resistivity values can be assumed to represent DC resistivity. For measurement of the GPR velocity (or dielectric permittivity) a 1.6 GHz GPR antenna was placed on top of the soil sample and the reflections from the bottom plate were recorded (Fig. 2.2b). Tests at the beginning showed that for high clay and water contents of the samples it was not possible to record the reflections from the bottom plate through the whole sample due to high attenuation. Therefore, the cylinder was filled only half with the soil at the beginning of each water content step, then the GPR measurement was conducted, the cylinder was filled completely with the soil sample and the electrical resistivity was measured. After one water content step was completed, the soil was taken out, a defined amount of rain water was added and mixed to achieve a homogeneous sample. Then the measuring procedure was repeated. The addition of rain water was conducted until it was not further possible to mix the sample (even by a motorised mixer). To control the water content small subsamples were taken from the first and last water content step and dried in the oven for 48 hours at a temperature of 105°. Additionally the amount of added water and the whole sample were weighted for each step.

As an output from the measurements we yield data for all 23 samples for the electrical conductivity and the traveltime t for the GPR reflection coming from the bottom plate for water contents ranging from 0 to 37 vol%.

The GPR velocity was calculated from the traveltime and the travelpath taking the distance between transmitter and receiver into account. The velocity and the dielectric permittivity are connected as follows:

$$\varepsilon_r = \left(\frac{c}{v}\right)^2 , \tag{2.2}$$

where $\varepsilon_r = \varepsilon/\varepsilon_0$ is the relative permittivity, ε the (absolute) permittivity, ε_0 the permittivity of free space, c the velocity of light and v the determined velocity of the soil sample.

Other data originating from the GPR reflection measurements are the measured waveforms. They will be investigated with respect to attenuation of electromagnetic waves and the quality factor in chapter 3.

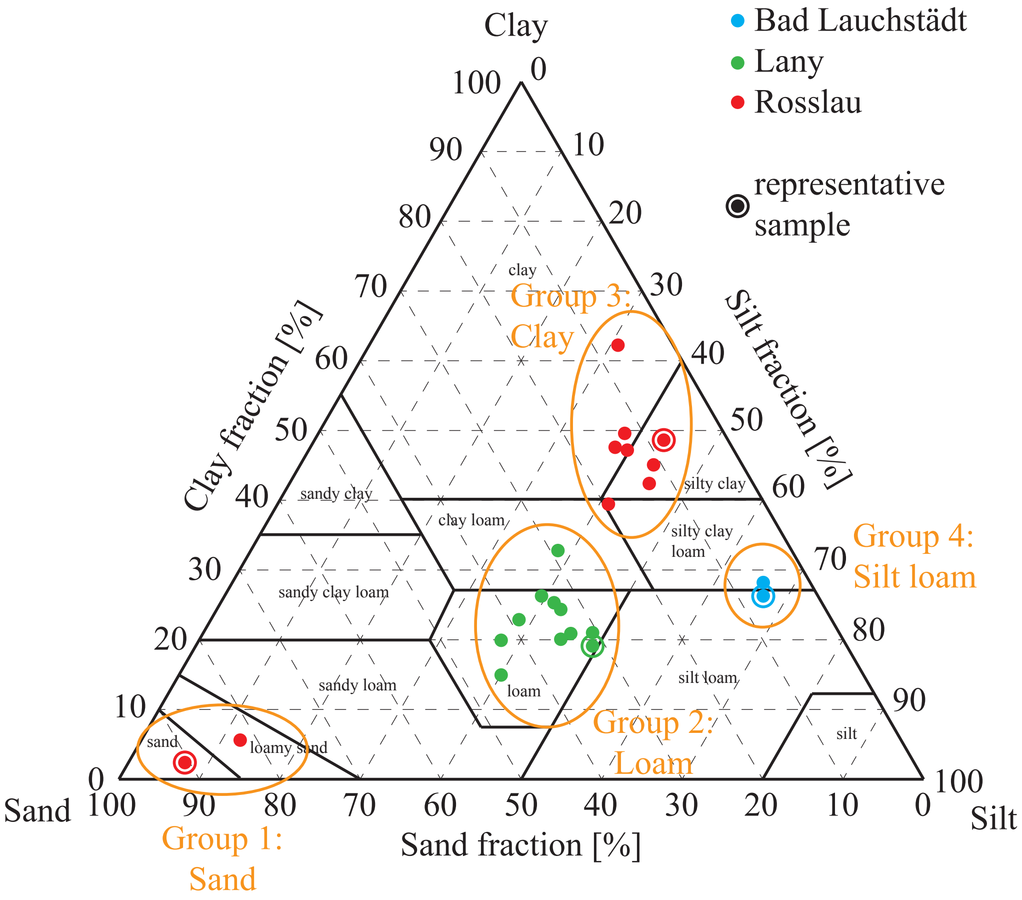

Fig. 2.1: Soil texture triangle showing the 23 samples separated into 4 groups (The classes are based on the soil texture triangle from the United States Department of Agriculture (USDA, www.usda.gov)).

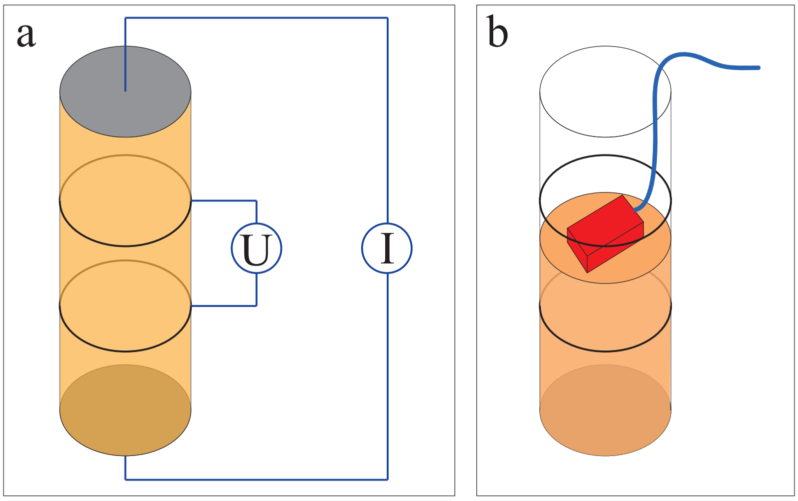

Fig. 2.2: Sketch of the plastic cylinder with ring and plate electrodes for measurements of electrical conductivity (a) and half filled with 1.6 GHz GPR antenna (b).

2.2.2 Models for permittivity

Several models connecting soil and geophysical parameters are available in the literature. The most frequent models are those with a relationship to water content. Three groups can be distinguished that are empirical (and semi-empirical), mixing models and effective medium approximations (Steelman and Endres 2011). An overview about the relationships between permittivity and volumetric water content that are applied to the laboratory data is given in Tab. 2.1. There is also one, which includes the clay content as an additional factor (equation (2.8)). Some formulas do not include the volumetric water content, but the saturation. Saturation (S), volumetric water content (θ) and porosity (Φ) are connected by

$$S = \frac{\theta}{\Phi} \ . \tag{2.3}$$

Empirical models

The empirical models are all third order polynoms of relative permittivity that describe the volumetric water content. Topp et al. (1980) were the first who presented their fitting equation obtained on samples from sandy loam to clay with different fresh and salt water mixtures and saturations (2.4). The permittivities were measured with time domain reflectometry (TDR). Also Nadler et al. (1991) used TDR to measure the permittivity for different layers of silt loam soils. Their equation (2.5) predicts the volumetric water content for high permittivities to be lower than calculated with the equation by Topp et al. (Fig. 2.3). The curve for the Roth et al. (1992) model varies around the Topp curve and the empirical model by Jacobsen and Schjønning (1993) lies between Topp and Nadler curves. The model by Roth et al. (eq. (2.6)) was established using nine mineral soil samples, whereas Jacobsen and Schjønning (eq. (2.7)) used soil textures ranging from coarse sand to sandy clay loam. Additional to their standard third order polynom they also incorporated the effects of dry bulk density, clay and organic carbon content in an enhanced third order polynom (eq. (2.8)).

Volumetric mixing models

The next group are the volumetric mixing models. Lichtenecker and Rother (1931) proposed a general form of a mixing model that predicts the bulk permittivity of a material by the sum of the permittivities of the constituents weighted by their volumetric fraction (eq. (2.9)). This model also includes an exponent that can be used as fitting parameter. A soil sample can be assumed to consist of grains, air and water so that the mixing model for this three-phase system can be derived taking the volume fractions of air, water and grains to be V(air) = $\Phi - \theta$, V(water) = θ and V(grains) = $1 - \Phi$, respectively. The resulting equation is transformed to determine the water content (eq. (2.10), Roth et al. 1990). A special case of this equation is the well-known Complex Refractive Index Model (CRIM) with the exponent being 0.5 (eq. (2.11), Birchak et al. 1974).

Effective medium models

The effective medium models do not only take the volumetric fractions of the components into account, but also geometrical information. In these models the soil is represented as a background material in which particles of a special shape are embedded (Endres and Redman 1996). Sen (1981) gives a general formulation for the embedding of a material 2 into a material 1 for any geometry of the embedded material (eq. (2.12)). The shape is given by the depolarization factor L that is in the range 0 to 1. For spheres it is assumed to be 1/3, for needles 0 and for plates 1 (Sen et al. 1981). Several inclusion schemes are possible. Three of them are used in the following sections: (1) Water coated grain spheres are embedded into an air matrix with air being the interconnected phase (eq. (2.13) and (2.14), (2) Spherical inclusions of air and grain are embedded into water with water being the interconnected phase (eq. (2.15)) and (3) the successive embedding of air spheres into water to result in an effective porefilling and afterwards the inclusion of spherical grains into this porefilling (eq. (2.16) and (2.17)). The mentioned equations were derived for L=1/3, but can be derived from (2.12) also for other depolarization factors. This derivation shall be explained in the following paragraph for the last model.

Empirical models	Topp et al. (1980)	Polynom of 3rd order: $\theta = -5.3\cdot10^{-2} + 2.92\cdot10^{-2}\cdot\varepsilon_b - 5.5\cdot10^{-4}\cdot\varepsilon_b^2 + 4.3\cdot10^{-6}\cdot\varepsilon_b^3$ (2.4)
	Nadler et al. (1991)	Polynom of 3rd order: $\theta = -7.25\cdot10^{-2} + 3.67\cdot10^{-2}\cdot\varepsilon_b - 12.3\cdot10^{-4}\cdot\varepsilon_b^2 + 15\cdot10^{-6}\cdot\varepsilon_b^3$ (2.5)
	Roth et al. (1992)	Polynom of 3rd order: $\theta = -7.28\cdot10^{-2} + 4.48\cdot10^{-2}\cdot\varepsilon_b - 19.5\cdot10^{-4}\cdot\varepsilon_b^2 + 36.1\cdot10^{-6}\cdot\varepsilon_b^3$ (2.6)
	Jacobsen & Schjønning (1993)	Polynom of 3rd order: $\theta = -7.01\cdot10^{-2} + 3.47\cdot10^{-2}\cdot\varepsilon_b - 11.6\cdot10^{-4}\cdot\varepsilon_b^2 + 18\cdot10^{-6}\cdot\varepsilon_b^3$ (2.7) Polynom or 3rd order with effects of ρ_b, C_c and C_{org}: $\theta = -3.41\cdot10^{-2} + 3.45\cdot10^{-2}\cdot\varepsilon_b - 11.4\cdot10^{-4}\cdot\varepsilon_b^2 + 17.1\cdot10^{-6}\cdot\varepsilon_b^3$ (2.8) $- 3.70\cdot10^{-2}\cdot\rho_b + 7.36\cdot10^{-4}\cdot C_c + 47.7\cdot10^{-4}\cdot C_{org}$
Volumetric mixing models	Lichtenecker & Rother (1931)	General mixing model for n phases: $\varepsilon_b^\alpha = \sum_{i=1}^{n} \eta_i\cdot\varepsilon_i^\alpha$ (2.9)
	Roth et al. (1990)	3-phase system: $\theta = \dfrac{\varepsilon_b^\alpha - (1-\Phi)\,\varepsilon_s^\alpha - \Phi\,\varepsilon_a^\alpha}{\varepsilon_w^\alpha - \varepsilon_a^\alpha}$ (2.10)
	Birchak et al. (1974)	Complex Refractive Index Model (CRIM) for $\alpha = 0.5$ and $\varepsilon_a = 1$: $\theta = \dfrac{\varepsilon_b^{1/2} - (1-\Phi)\,\varepsilon_s^{1/2} - \Phi}{\varepsilon_w^{1/2} - 1}$ (2.11)

Tab. 2.1: Overview of empirical, volumetric mixing and effective medium models for permittivity (continued on next pages). θ: volumetric water content, ε: relative permittivity, subscripts b, s, a, w and p denote bulk, solid, air, water and pore, ρ_b: dry bulk density, C_c: clay content, C_{org}: organic matter content, η: volume fraction, α: mixing exponent, Φ: porosity, S: saturation, p: integration variable from 0 to 1, L: depolarization factor, m and n: cementation and saturation exponents

Effective medium models	Sen (1981)	General formula to embed material 2 into material 1: $\frac{\varepsilon_b - \varepsilon_1}{L\cdot\varepsilon_b + (1-L)\cdot\varepsilon_1} = \eta \frac{\varepsilon_2 - \varepsilon_1}{L\cdot\varepsilon_2 + (1-L)\cdot\varepsilon_1}$ (2.12)
	Sen et al. (1981), Steelman & Endres (2011)	Water coated spheres (CS) are embedded in air: $\varepsilon_{CS} = \varepsilon_w \cdot \frac{3\cdot(1-\Phi)\cdot\varepsilon_s + \theta\cdot(\varepsilon_s + 2\varepsilon_w)}{3\cdot(1-\Phi)\cdot\varepsilon_w + \theta\cdot(\varepsilon_s + 2\varepsilon_w)}$ (2.13) $\frac{d\varepsilon(p)}{dp} = \frac{3\cdot(1-\Phi+\theta)\cdot\varepsilon(p)}{(\Phi-\theta) + p\cdot(1-\Phi+\theta)} \cdot \frac{\varepsilon_{CS} - \varepsilon(p)}{\varepsilon_{CS} + 2\varepsilon(p)}$ (2.14) for $\varepsilon(p=0) = \varepsilon_a$ and $\varepsilon(p=1) = \varepsilon_b$
	Feng & Sen (1985), Steelman & Endres (2011)	Spherical inclusions of air and grains are embedded simultaneously in water: $\frac{d\varepsilon(p)}{dp} = \frac{3\cdot\varepsilon(p)}{p(1-\theta) + \theta} \cdot \left[(1-\Phi) \frac{\varepsilon_s - \varepsilon(p)}{\varepsilon_s + 2\varepsilon(p)} + (\Phi - \theta) \frac{\varepsilon_a - \varepsilon(p)}{\varepsilon_a + 2\varepsilon(p)} \right]$ (2.15) for $\varepsilon(p=0) = \varepsilon_w$ and $\varepsilon(p=1) = \varepsilon_b$
	Endres & Redman (1996), Steelman & Endres (2011)	Air spheres are embedded in pore filling (water): $\frac{d\varepsilon(p)}{dp} = \frac{3\cdot(1-S)\cdot\varepsilon(p)}{S + p(1-S)} \cdot \frac{\varepsilon_a - \varepsilon(p)}{\varepsilon_a + 2\varepsilon(p)}$ (2.16) for $\varepsilon(p=0) = \varepsilon_w$ and $\varepsilon(p=1) = \varepsilon_p$ Spherical grains are embedded in porefilling: $\frac{d\varepsilon(p)}{dp} = \frac{3\cdot(1-\Phi)\cdot\varepsilon(p)}{\Phi + p(1-\Phi)} \cdot \frac{\varepsilon_s - \varepsilon(p)}{\varepsilon_s + 2\varepsilon(p)}$ (2.17) for $\varepsilon(p=0) = \varepsilon_p$ and $\varepsilon(p=1) = \varepsilon_b$

Tab. 2.1 (continued)

Effective medium models (cont.)	Brovelli & Cassiani (2010)	Hashin-Shtrikman bounds (for pore space): $\varepsilon_{HSL,p} = \varepsilon_a + \frac{S}{(\varepsilon_w-\varepsilon_a)^{-1} + \frac{1 - S}{3\varepsilon_a}}$ (2.18) $\varepsilon_{HSU,p} = \varepsilon_w + \frac{1 - S}{(\varepsilon_a-\varepsilon_w)^{-1} + \frac{S}{3\varepsilon_w}}$ (2.19) Permittivity for pore space: $\varepsilon_p = \frac{\varepsilon_w}{\varepsilon_{HSU,p} \cdot S^{-n}} \cdot \varepsilon_{HSU,p} + (1 - \frac{\varepsilon_w}{\varepsilon_{HSU,p} \cdot S^{-n}}) \cdot \varepsilon_{HSL,p}$ (2.20) Hashin-Shtrikman bounds (for bulk permittivity): $\varepsilon_{HSL,b} = \varepsilon_s + \frac{\Phi}{(\varepsilon_p-\varepsilon_s)^{-1} + \frac{1 - \Phi}{3\varepsilon_s}}$ (2.21) $\varepsilon_{HSU,b} = \varepsilon_p + \frac{1 - \Phi}{(\varepsilon_s-\varepsilon_p)^{-1} + \frac{\Phi}{3\varepsilon_p}}$ (2.22) Bulk permittivity: $\varepsilon_b = \frac{3 - \Phi}{2} \cdot \Phi^{m-1} \cdot \varepsilon_{HSU,b} + (1 - \frac{3 - \Phi}{2} \cdot \Phi^{m-1}) \cdot \varepsilon_{HSL,p}$ (2.23)

Tab. 2.1 (continued)

Equation (2.12) explains the bulk permittivity (ε_b) after a small volume fraction of material 2 (ε_2) is embedded into material 1 (ε_1). For the next embedding step (k+1) the background permittivity is the bulk permittivity from the previous step (k). Accordingly the equation can be rewritten as

$$\frac{\varepsilon_{k+1} - \varepsilon_k}{L \cdot \varepsilon_{k+1} + (1-L) \cdot \varepsilon_k} = \frac{\Delta V}{V} \frac{\varepsilon_2 - \varepsilon_k}{L \cdot \varepsilon_2 + (1-L) \cdot \varepsilon_k} \quad . \tag{2.24}$$

For very small volume fractions $\varepsilon_{k+1} - \varepsilon_k = d\varepsilon$ and $L \cdot \varepsilon_{k+1} + (1-L) \cdot \varepsilon_k \approx \varepsilon_k$. Thus it is

$$\frac{d\varepsilon}{\varepsilon} = \frac{dV}{V} \frac{\varepsilon_2 - \varepsilon}{L \cdot \varepsilon_2 + (1-L) \cdot \varepsilon} \quad . \tag{2.25}$$

For the inclusion of air into water to result in an effective pore filling the total volume of the porefilling is Φ and the volume of air that has to be included is Φ-θ. The volume fraction dV/V can then be written as

$$\frac{dV}{V} = \frac{(\Phi-\theta)\,dp}{\theta + p\cdot(\Phi-\theta)} = \frac{(1-S)\,dp}{S + p\cdot(1-S)} \quad . \tag{2.26}$$

The parameter p is an integration variable. In each step a small amount dp of air (Φ-θ) is embedded. In the beginning (p=0) the pores are completely filled with water and thus their total volume is θ. At the end of the embedding process (p=1) the total volume of the resulting porefilling is Φ and thus the embedding process is completed. The resulting differential equation of first order has to be integrated from $\varepsilon(p=0) = \varepsilon_w$ to $\varepsilon(p=1) = \varepsilon_p$:

$$\frac{d\varepsilon(p)}{dp} = \frac{(1-S)\cdot\varepsilon(p)}{S + p(1-S)} \cdot \frac{\varepsilon_a - \varepsilon(p)}{L\cdot\varepsilon_a + (1-L)\cdot\varepsilon(p)} \quad . \tag{2.27}$$

The equations for the subsequent embedding of grains into the porefilling and also for the other embedding schemes can be derived in the same way for any depolarization factor L.

In practice the differential equations cannot be solved analytically and for this reason a solver from Matlab (ode45) is used to integrate it numerically.

Another model based on effective medium theory is developed by Brovelli and Cassiani (2010). It uses the Hashin-Shtrikman bounds (Hashin and Shtrikman 1962) that give the narrowest possible range of electromagnetic properties a mixture of materials can have. For the case of full saturation the upper bound is the effective permittivity of isolated spherical grains that are coated by water with water being the interconnected phase. For the lower bound the materials are interchanged (Brovelli and Cassiani 2010). The model by Brovelli and Cassiani uses a weighted sum of these bounds to describe first the porefilling (water + air) and then to incorporate grains into the porefillling (eq. (2.18) - (2.23)). The geometrical features are taken into account by the parameters m and n that are the cementation and saturation exponent of Archie‘s equation (Archie 1942). The advantage of this model is that the same parameterisation is used for electrical conductivity and permittivity.

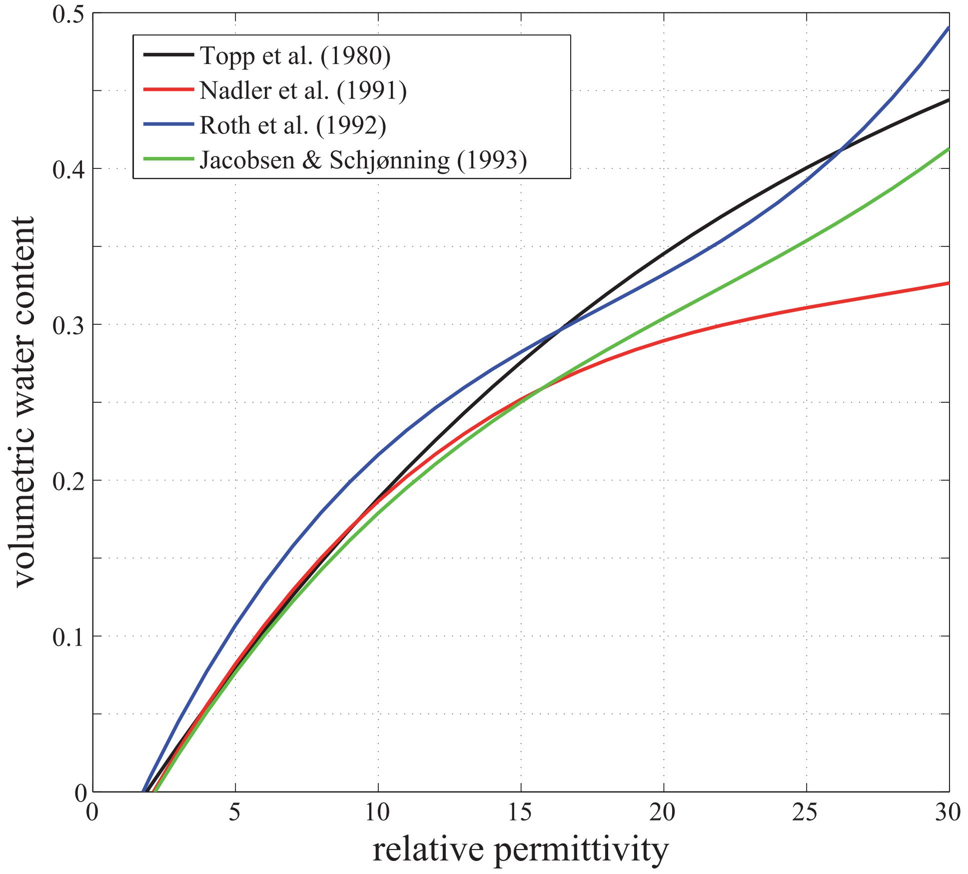

Fig. 2.3: Predictions of volumetric water content for the empirical models (equations (2.4) - (2.7)).

2.2.3 Models for electrical conductivity

For the relationship between electrical conductivity and volumetric water content a smaller number of models is applied. They are listed in Tab. 2.2.

The first well-known empirical model is Archie‘s law (eq. (2.28), Archie 1942) that was originally developed for oil-bearing sandstones. It relates the bulk electrical resistivity to the resistivity of the fluid and the degree of saturation. If the soil has non-negligible clay content this equation is not applicable, because the clay minerals have an additional surface conductivity due to their electrical double layer. Waxman and Smits (1968) developed an empirical model that describes the soil or rock as two parallel resistors. One is the resistance due to the pore fluid and the other the resistance due to clay minerals (Taylor and Barker 2006). In equation (2.29) this is written as the sum of the electrical conductivity of the fluid and the term $(BQ_v)/S$ representing the electrical surface conductivity of the clay. Q_v is the cation exchange capacity (in meq/ml) and B the equivalent ionic conductance of clay exchange ions (in (S·l)/(eq·m)). The cation exchange capacity (CEC) represents the number of counter-ions in the Stern layer (a layer of adsorbed cations to balance the net negative charge of the clay mineral surface) that may

be exchanged with other ions in the pore water (Taylor and Barker 2006). The equivalent ionic conductance of clay exchange ions is a function of the electrical resistivity of the pore fluid (Worthington 1993). For simplification the term $(BQ_v)/S$ is fitted as a single parameter, namely the electrical conductivity of the solids (i.e. the surface conductivity of the clay particles, σ_s, eq. (2.30)). The fitting of σ_w and σ_s is not unique, because both parameters are unknown.
For the group of effective medium models two approaches are applied to the data. The first is the Hanai-Bruggeman equation (eq. (2.31)+(2.32), Bruggeman 1935, Hanai 1960), which embeds a parallel resistor combination of air and solids (the so-called dispersed phase) into a water background (Taylor and Barker 2006). Because air is assumed to have infinite electrical resistivity it does not appear notably in the equations. The second effective medium model is the model by Brovelli and Cassiani (2010) that was already mentioned in the previous section.

Empirical models	Archie (1942), Taylor & Barker (2006)	$\rho = a \cdot \rho_w \cdot \Phi^{-m} \cdot S^{-n}$ (2.28)
	Waxman & Smits (1968), Taylor & Barker (2006)	$\sigma = a \cdot \Phi^{-m} \cdot S^{n} \cdot (\sigma_w + \frac{BQ_v}{S})$ (2.29) $\sigma = a \cdot \Phi^{-m} \cdot S^{n} \cdot (\sigma_w + \sigma_s)$ (2.30)
Effective medium models	Bruggeman (1935), Hanai (1960), Taylor & Barker (2006)	$\rho = \rho_w \cdot S^{-m} \cdot \Phi^{-m} \cdot (\frac{1 - \rho_w/\rho_d}{1 - \rho/\rho_d})^{-m}$ (2.31) $\rho_d = \rho_s \frac{1 - S \cdot \Phi}{1 - \Phi}$ (2.32)
	Brovelli & Cassiani (2010)	same parameterisation as for the permittivity

Tab. 2.2: Overview of empirical and effective medium models for electrical conductivity/resistivity. ρ: electrical resistivity, σ: electrical conductivity ($\sigma = 1/\rho$), subscripts s, w and d denote solid, water and dispersed phase, Φ: porosity, S: saturation, m and n: cementation and saturation exponents, a: parameter for fitting, B: equivalent ionic conductance of clay exchange ions, Q_v: cation exchange capacity per unit pore volume

2.2.4 Significance of error improvement between models

The fit of the models will be evaluated using the absolute RMS (root mean square) error, which is calculated by

$$\mathrm{RMSE} = \frac{\| \theta_{obs} - \theta_{mod} \|_2}{n} \quad , \tag{2.33}$$

where θ_{obs} and θ_{mod} are the observed and modelled volumetric water contents and n the number of measurements.

The significance of the error improvement between two models can be determined using the F-Test. This test takes the degrees of freedom $\nu = n-m$ (n: number of measurements, m: number of model parameters) of the different models into account, because in most cases more complicated models, i.e. with a higher number of model parameters, give better RMS errors.

As a first step the prediction errors of two models will be calculated by

$$e_{i,k} = \theta_{i,k}^{obs} - \theta_{i,k}^{mod} \tag{2.34}$$

for i=1...n and k=1, 2 (model 1 and model 2). Then the variance of the error can be estimated using ν degrees of freedom (Menke 1989) and assuming a mean error of zero taking the probably general poor fit of the model into account:

$$\mathrm{var}_k = \frac{1}{\nu} \sum_i (e_{i,k})^2 \quad . \tag{2.35}$$

The statistic F is then the ratio of the variances of both models (Gränicher 1994):

$$F = \frac{\mathrm{var}_1}{\mathrm{var}_2} \quad . \tag{2.36}$$

The best fitting model of each group will be used as model 2 and compared to all other models. The resulting F is compared to the F distribution using a table of 5 % confidence limit (e.g. Gränicher 1994). If the calculated F is greater or equal to the corresponding critical value of the F distribution, the improvement of model 2 over model 1 is significant.

2.3 Results

In this section the mentioned models linking permittivity and electrical conductivity to volumetric water content will be applied to the laboratory data. First the models for permittivity and second the models for electrical conductivity will be investigated. The model by Brovelli and Cassiani (2010) describing permittivity and conductivity in the same framework will be shown in an extra section. Afterwards a best-fit model as a combination from the known models will be developed and the relationship between permittivity and electrical conductivity will be investigated.

For each sample the RMS error between observed and calculated volumetric water content is determined. For simplification the samples have been sorted into 4 groups regarding Fig. 2.1 and only the result of the representative sample of each group is plotted.

2.3.1 Models for permittivity

In all mentioned models for the permittivity the following constants are used: $\varepsilon_s = 5$ as the relative permittivity of grains (solid), $\varepsilon_w = 81$ as the relative permittivity of water and $\varepsilon_a = 1$ as the relative permittivity of air. The permittivity of solid soil particles varies between 4.5-6.5 (Brovelli and Cassiani 2008), but cannot be determined by our measurements. Thus a mean value of 5 is used, which is appropriate for sand and loamy soils (Steelman and Endres 2011). For clay the permittivity of the solids can be higher, but for unification a value of 5 is also used for the clayey samples.

Empirical models

The curves of the empirical models are the same for every sample, because they do not have additional parameters. Only the enhanced third order polynom by Jacobsen and Schjønning includes also ρ_b, c_c and c_{org}. The bulk density for all samples was estimated to be 1.5 g/cm^3, whereas the clay and organic matter content have been measured independently for each sample. For group 1 the shape of the curves reflects the shape of the data points, but the water content is overestimated (Fig. 2.4). For all other groups the shape of the curves does not fit to the data, but nevertheless the RMS error is smaller than for the sandy samples. The mean absolute RMS errors for each group and each model are summarised in Tab. 2.3. The lowest RMS error is achieved for the sandy samples by the enhanced model of Jacobsen and Schjønning. The standard third order polynom of the same authors gives the best fit for loam and silt loam, whereas the model of Topp et al. fits best the clayey samples. For clay all models yield similar RMS errors. The Roth et al. model strongly overestimates the volumetric water content for all soil groups. The significance of the error improvement between different models was tested using the F-test (section 2.2.4). Light green cells in Tab. 2.3 mark those models whose degradation of the RMS error is not significant compared to the best fitting model. This shows that the models of Jacobsen & Schjønning (1993) are suitable to fit all soil textures satisfactorily. It also demonstrates that there is no model, which is significantly dominating over the others with respect to a good fit. The use of a more complicated model, i.e. the enhanced model of Jacobsen & Schjønning, in comparison to an easier model, e.g. the simple third order polynom of the same authors, does not lead to a significant better fit. Thus, for the empirical models the standard polynom of Jacobsen and Schjønning seems to be the best in most cases.

Group	RMSE Topp et al.	RMSE Nadler et al.	RMSE Roth et al.	RMSE Jacobsen & Schjønning	RMSE Jacobsen & Schjønning (enhanced)
1: Sand	0.061	0.043	0.073	0.041	0.026
2: Loam	0.036	0.037	0.064	0.031	0.033
3: Clay	0.031	0.034	0.038	0.037	0.033
4: Silt loam	0.034	0.035	0.061	0.029	0.036

Tab. 2.3: Mean absolute RMS errors for the empirical models for each group. The best model RMSE is highlighted in dark green for each group. The light green cells represent models, whose fit is not significantly worse compared to the best model.

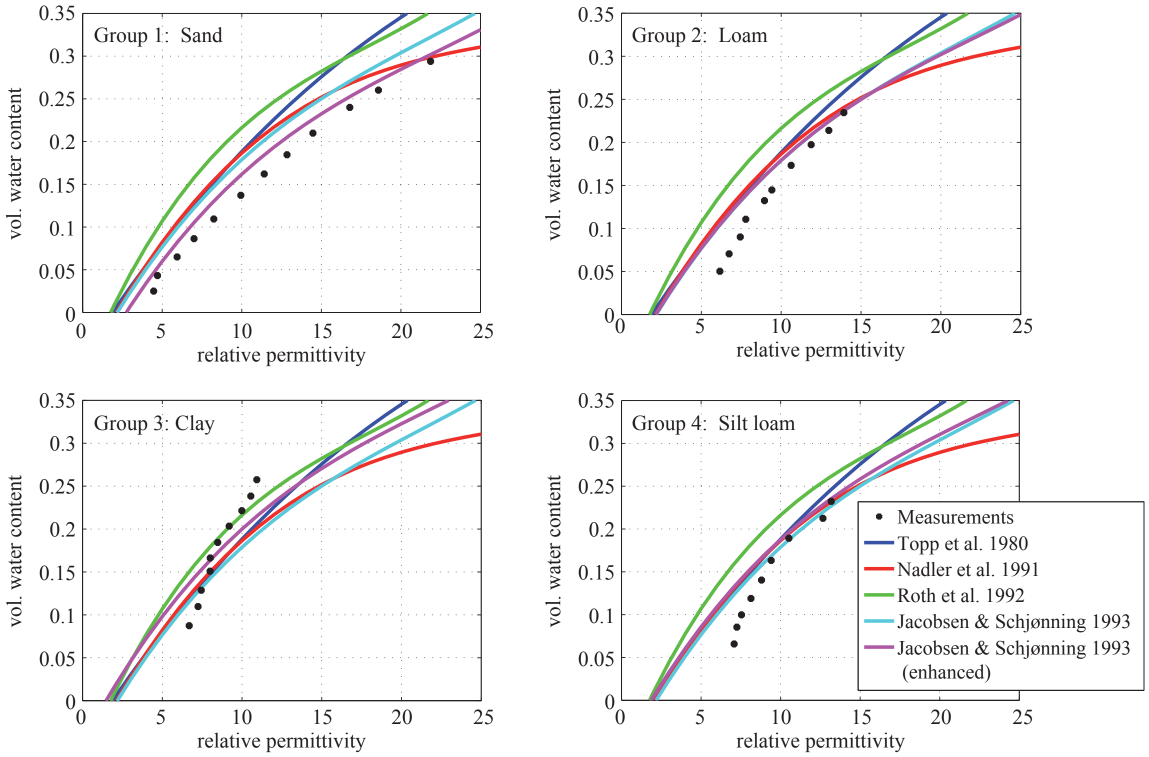

Fig. 2.4: Volumetric water content as a function of relative permittivity and empirical relationships for the representative sample of each group.

Volumetric mixing models

The three-phase volumetric mixing models have been applied with fixed mixing exponent α=0.46 (Roth et al. 1990, eq. (2.10)) and α=0.5 (CRIM, eq. (2.11)). Additionally α was used as a fitting parameter to achieve the best fit between data and model. The resulting curves are shown in Fig. 2.5 and the mean absolute RMS errors are listed in Tab. 2.4. For all groups the CRIM model is superior over the Roth et al. model. Except for the clayey (and partly the silt loam) samples a significant improvement of the fit can be achieved by using α as a fitting parameter. For clays the best fitting α is close to the values by Roth et al. and CRIM. The values of the best fitting α suggest that they might be related to clay content. Plotting α for each sample against clay content results in high correlation with correlation coefficient R = -0.86 (Fig. 2.6). The equation of the fitting line is

$$\alpha = -0.46 \cdot c_c + 0.71, \tag{2.37}$$

where the clay content c_c is given as mass fraction (and not in %).

If this equation is used to determine the proper α for each sample, the RMS errors between model and data are the same as for the best-fit model. This means that the above-mentioned equation is suitable to determine α directly from clay content.

Group	RMSE Roth et al.	RMSE CRIM	RMSE „best fit“	α „best fit“
1: Sand	0.053	0.045	0.013	0.71
2: Loam	0.037	0.030	0.018	0.61
3: Clay	0.029	0.029	0.028	0.48
4: Silt loam	0.045	0.036	0.019	0.63

Tab. 2.4: Mean absolute RMS errors for the 3-phase volumetric mixing models and the best fitting α (mixing exponent) for each group. The best model RMSE is highlighted in dark green for each group. The light green cells represent models, whose fit is not significantly worse compared to the best model.

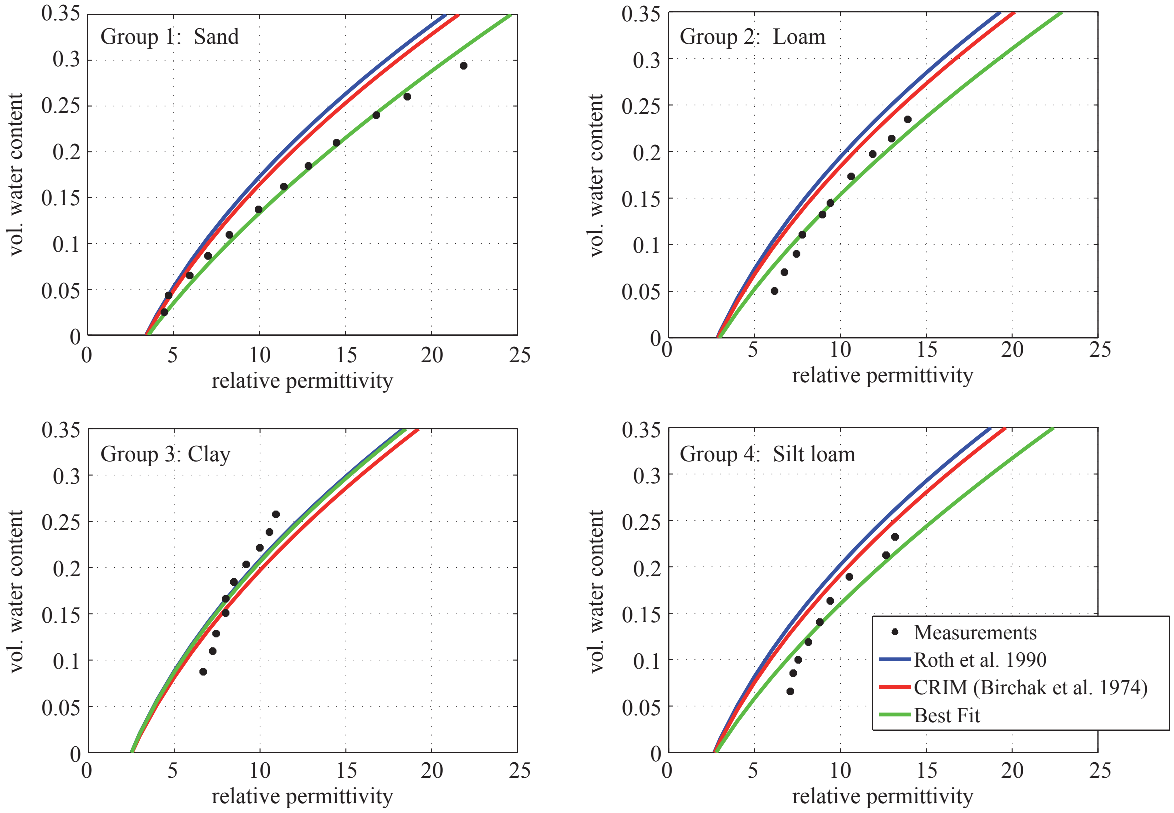

Fig. 2.5: Volumetric water content as a function of relative permittivity and volumetric mixing models for the representative sample of each group.

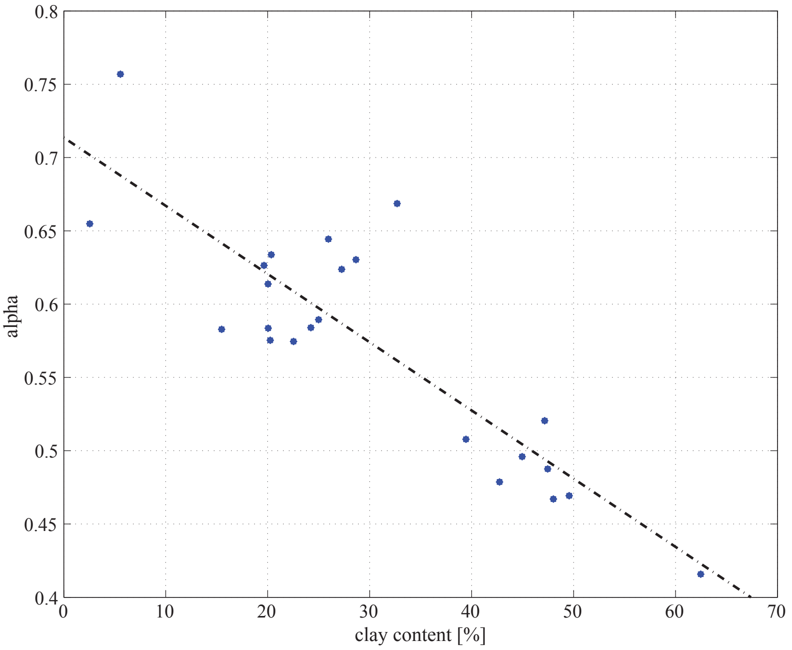

Fig. 2.6: Correlation between clay content and the best fitting parameter α (mixing exponent) for all samples.

Effective medium models

For the fitting of the effective medium models the three mentioned embedding schemes were used, but with a variable depolarization factor L. This factor was varied between 1/2 and 1/9 to achieve the best fit. The results for the representative samples are plotted in Fig. 2.7 and the mean RMS errors and the mean best fitting L are summarized in Tab. 2.5.

For the representative sample of group 1 (sand) the fit of all models is perfect with RMS errors between 0.005-0.009. Although the fit for the other sample of this group is not as good, this group has in general the lowest RMS errors (Tab. 2.5). But also the other groups reveal good fits except from group 3 (clay). Surprisingly the depolarization factor is not 1/3 (spheres) for the sandy samples as expected, but for the other groups for the embedding schemes of Feng and Sen (1985) and Endres and Redman (1996). Clay particles are normally assumed to be plates and sand particles to be spheres. For these data shown here the depolarization factors seem to have a different meaning.

The model of Sen et al. (1981) has for most textures the best fit, whereas the model of Feng and Sen (1985) is not significantly worse (light green cells in Tab. 2.5).

	Sen et al.		Feng and Sen		Endres and Redman	
Group	RMSE	L	RMSE	L	RMSE	L
1: Sand	0.012	1/5	0.013	1/5	0.024	1/5
2: Loam	0.019	1/4	0.019	1/3	0.018	1/3
3: Clay	0.030	1/4	0.036	1/3	0.037	1/3
4: Silt loam	0.018	1/5	0.023	1/3	0.020	1/3

Tab. 2.5: Mean absolute RMS errors for the effective medium models with best fitting L for each group. The best model RMSE is highlighted for each group. The light green cells represent models, whose fit is not significantly worse compared to the best model.

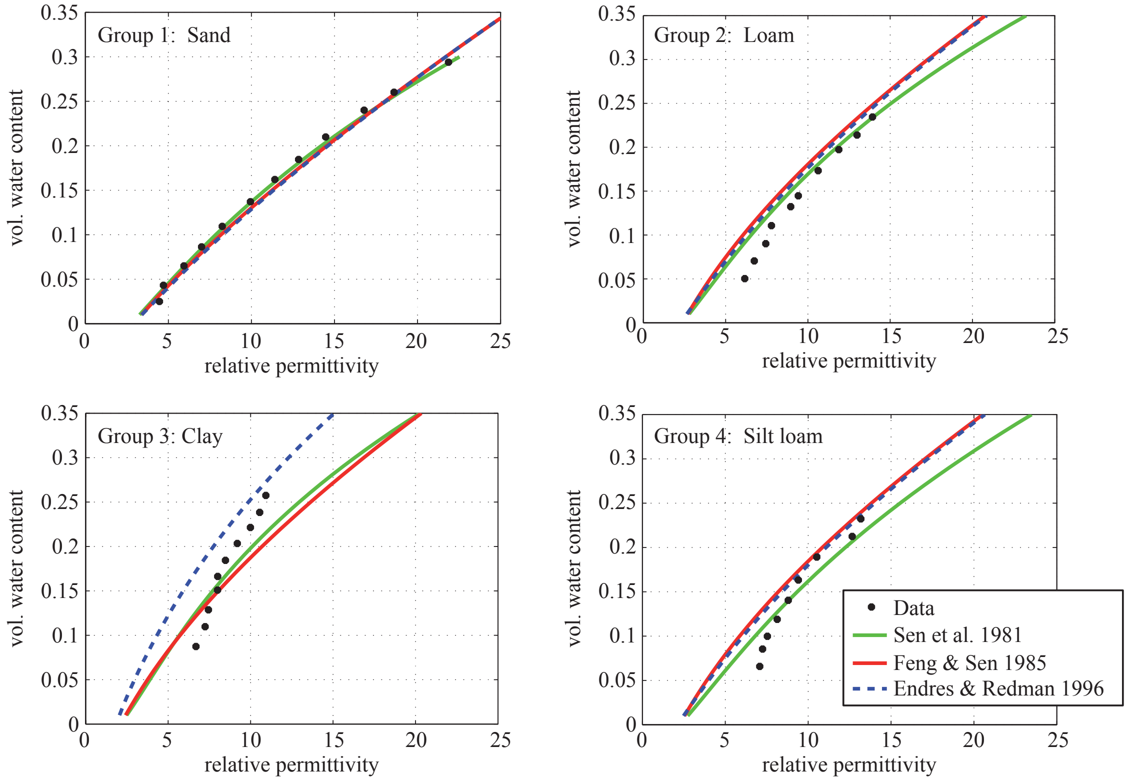

Fig. 2.7: Volumetric water content as a function of relative permittivity and effective medium models for the representative sample of each group.

2.3.2 Models for electrical conductivity

In contrary to the permittivity the values for the electrical conductivity of water and solids are unknown. The electrical conductivity of the rain water was measured for some experiments and hence a range of possible values is available. The electrical conductivity of air is assumed to be 0. For the parameters a, m and n from Archie and Waxman-Smits equations the possible range was restricted in the optimisation procedure to that found in literature for soils. An overview about the used ranges is given in Tab. 2.6.

Empirical models

The two empirical models for the electrical resistivity are Archie‘s law and the Waxman-Smits-equation. As expected Archie‘s law fits the sand sample perfectly, whereas it cannot fit the samples with non-negligible clay content (Fig. 2.8). For these samples the Waxman-Smits model gives good results, especially for lower resistivities.

The mean absolute RMS errors for volumetric water content and the mean fitting parameters are listed in Tab. 2.7.

Parameter	Range	Reference (based on)
a	0.4 - 1.6	Worthington 1993
m	1.3 - 3	Friedman 2005
n	0.4 - 2	Taylor and Barker 2006
ρ_w	40 - 100 Ωm	own measurements
ρ_s	40 - 500 Ωm	-

Tab. 2.6: Ranges of fitting parameters that are used for the restriction of models. Note that the used ranges are rounded and do not exactly represent the values in the mentioned references.

	Archie					Waxman-Smits					
Group	RMSE	m	n	a	ρ_w [Ωm]	RMSE	m	n	a	ρ_w [Ωm]	ρ_s [Ωm]
1: Sand	0.023	1.37	1.49	0.46	43.16	0.036	1.31	1.75	0.41	99.72	497
2: Loam	0.084	1.30	1.56	0.40	40	0.007	1.84	1.84	0.87	84.50	320
3: Clay	0.091	1.51	2.00	0.58	49.04	0.025	2.02	2.00	1.00	79.89	274
4: Silt loam	0.083	1.30	1.77	0.40	40	0.010	2.00	1.98	1.00	80.05	271

Tab. 2.7: Mean absolute RMS errors and obtained fitting parameters for the empirical models for each group. The best model RMSE is highlighted for each group.

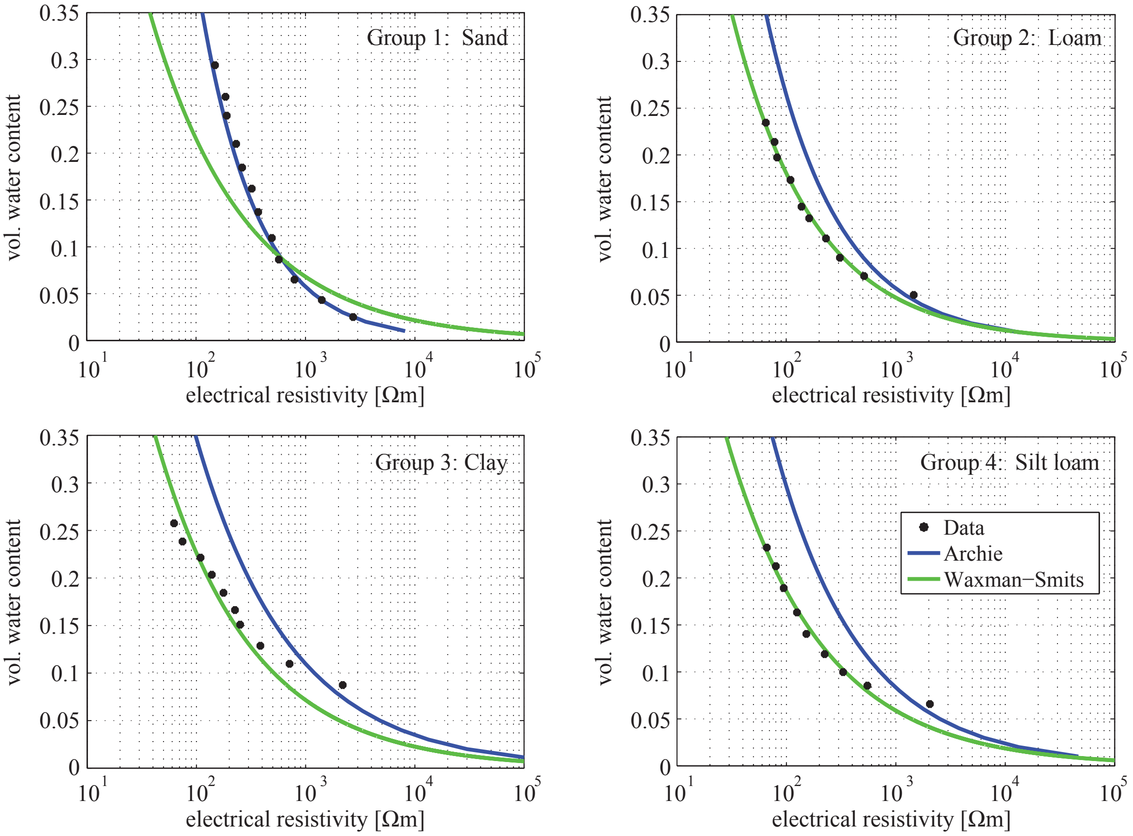

Fig. 2.8: Volumetric water content as a function of electrical resistivity and empirical models for the representative sample of each group.

Effective medium models

The Hanai-Bruggeman equations (2.31) and (2.32) can be solved for the saturation. This analytical solution is given by Berg (1995) and because of its length will not be repeated here. An optimisation procedure has been applied to fit the equation to the data, but given the restricted ranges of the parameters a reasonable solution could only be obtained for the sandy soil. Fig. 2.9 shows the result together with Archie and Waxman-Smits models. The Hanai-Bruggeman curve follows the Archie curve for high water contents but cannot reproduce the bending of the data curve for lower water contents. The determined fitting parameters are ρ_w = 45.54 Ωm, ρ_s = 500 Ωm and m = 1.3. The absolute RMS error of the volumetric water content is 0.062.

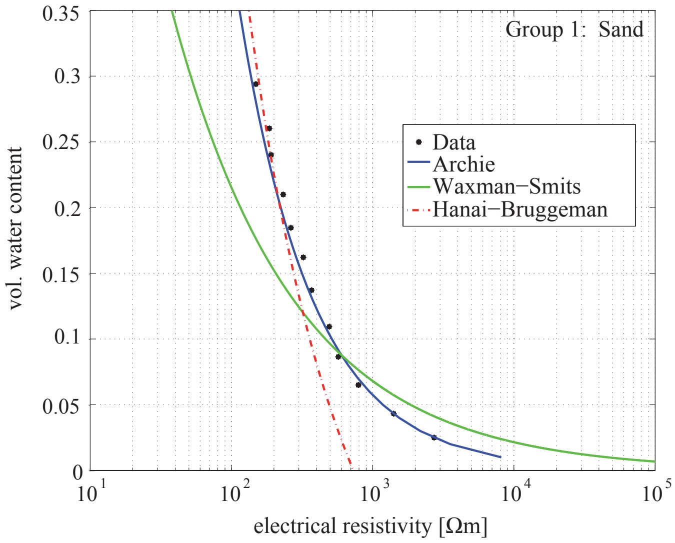

Fig. 2.9: Volumetric water content as a function of electrical resistivity and empirical and effective medium model for the representative sample of group 1 (sand).

2.3.3 Model for permittivity and conductivity with the same parameterisation

The effective medium model of Brovelli and Cassiani (2010) was applied to the data using m, n, ρ_w and ρ_s as restricted fitting parameters. Both permittivity and electrical conductivity were fitted simultaneously and m and n were chosen to achieve the best compromise between the fits of both parameters. Except for group 3 (clay) the fits are good with respect to the agreement of the shape of the curve and the data (Fig. 2.10). The RMS errors for all samples are satisfactory. The mean absolute RMS errors and the fitting parameters are listed in Tab. 2.8.

Because m and n are the cementation and saturation exponent of Archie‘s law and can thus be determined from electrical resistivity data alone, they can be used to predict the permittivity. This might be used to calculate the permittivity (and with this the GPR velocity) distribution based on a geoelectric profile (see section 2.3.6).

To test this application with the laboratory data the Brovelli and Cassiani equation was calculated using m and n that were determined by fitting Archie‘s law. The resulting curves are shown in Fig. 2.11 together with the fitted Brovelli and Cassiani curves for comparison. The absolute RMS error of the fit for the permittivity is 0.019, which is worse than the RMS error for this sample fitting the curve independently (RMSE=0.006). Nevertheless the result is still convincing that this procedure might work. The only condition is that Archie‘s law has to be suitable to fit the data, which is not the case for samples with non-negligible clay content.

Group	RMSE(ε)	RMSE(ρ)	m	n	ρ_w [Ωm]	ρ_s [Ωm]
1: Sand	0.017	0.037	1.30	1.45	73.52	285.18
2: Loam	0.028	0.025	1.30	1.83	74.54	40
3: Clay	0.031	0.051	1.70	1.95	48.57	40
4: Silt loam	0.025	0.034	1.34	1.55	57.55	40

Tab. 2.8: Mean absolute RMS errors and obtained fitting parameters for the Brovelli and Cassiani model for each group.

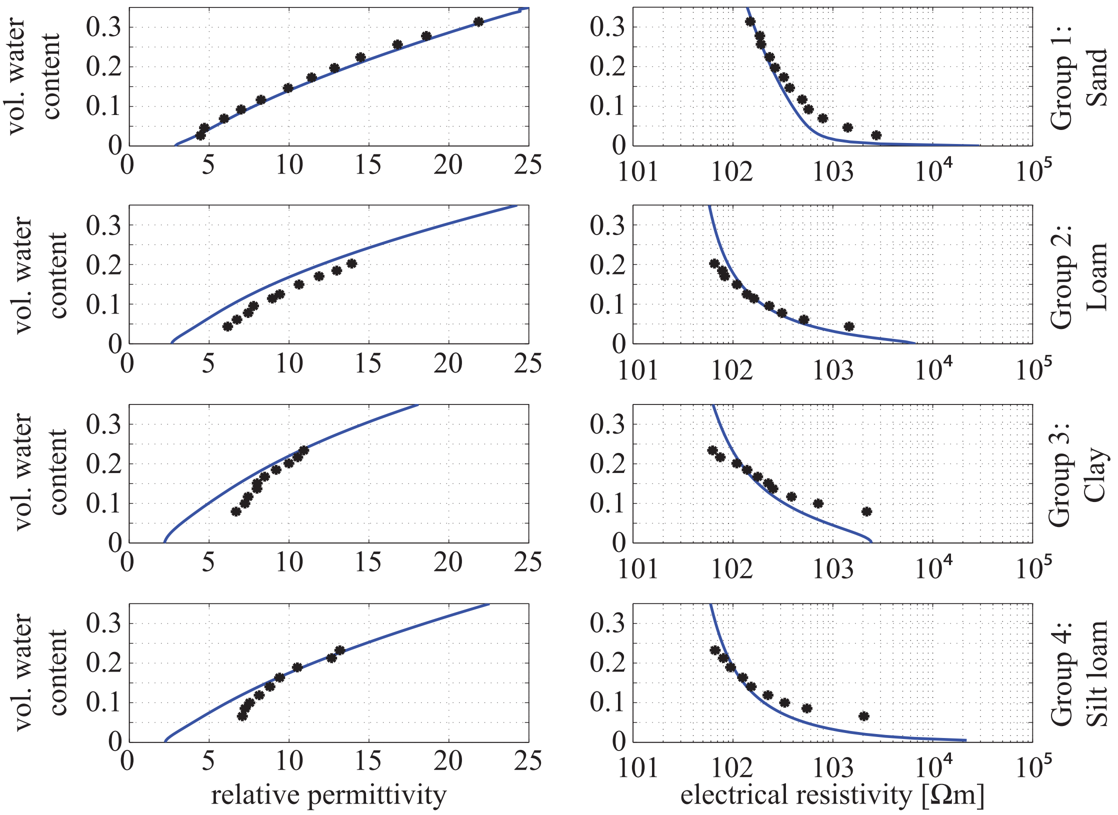

Fig. 2.10: Volumetric water content as a function of permittivity (left) and electrical resistivity (right) and Brovelli and Cassiani equation.

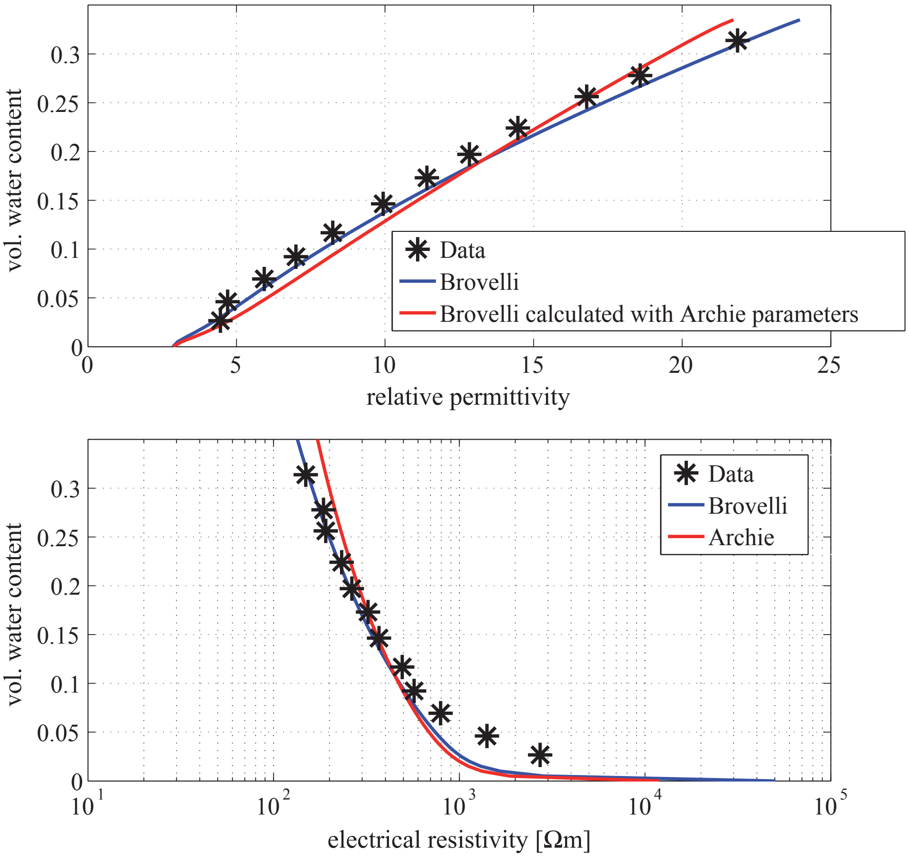

Fig. 2.11: The representative sample of group 1 (sand) with the curves of the fitted Brovelli and Cassiani equation (blue) and with the Brovelli and Cassiani equation calculated with the previously determined Archie parameters (red) for relative permittivity (top) and electrical resistivity (bottom).

2.3.4 Development of a new model

Fitting Archie‘s equation and the Brovelli and Cassiani model to the electrical resistivity of all samples revealed that Archie‘s law is better applicable to lower water contents, whereas the Brovelli and Cassiani model achieved better fits for the higher water content range. Hence both models were combined and a smooth transition was achieved by multiplying opposite sigmoid functions to both models and then calculating the sum. Schematically the resulting equation for the electrical conductivity can be written as

$$f_\sigma = f_A(\theta, a_A, n_A, m_A) \cdot \mathrm{sigm}(\theta, -a_S, b_S) + f_B(\theta, n_B, m_B, \sigma_{gr}, \sigma_w) \cdot \mathrm{sigm}(\theta, a_S, b_S) \, , \qquad (2.38)$$

where

$$\mathrm{sigm}(\theta, a, b) = \frac{1}{1+e^{-a(\theta-b)}} \quad . \qquad (2.39)$$

The subscripts A, B and S stand for Archie, Brovelli and sigmoid, respectively, θ is the volumetric water content and σ_{gr} and σ_w are the electrical conductivities of grains and water. The parameter a_S controls the slope of the sigmoid function and b_S the inflection point of the curve with respect to water content and thus the transfer from Archie to Brovelli and Cassiani equation. The different curves are shown as an example in Fig. 2.12.

For the permittivity the original form of the Brovelli and Cassiani model is used. Several combinations of the Brovelli and Cassiani equation with other models (e.g. CRIM) have been tried, but did not improve the fit.

Although m and n have the same meaning in Archie‘s law and the Brovelli and Cassiani equation they are fitted for both models independently, because for the Brovelli and Cassiani equation they also have to satisfy the fit of the permittivity. The fitted curves for each group are shown in Fig. 2.13 and the obtained mean fitting parameters and mean absolute RMS errors for water content are summarised in Tab. 2.9.

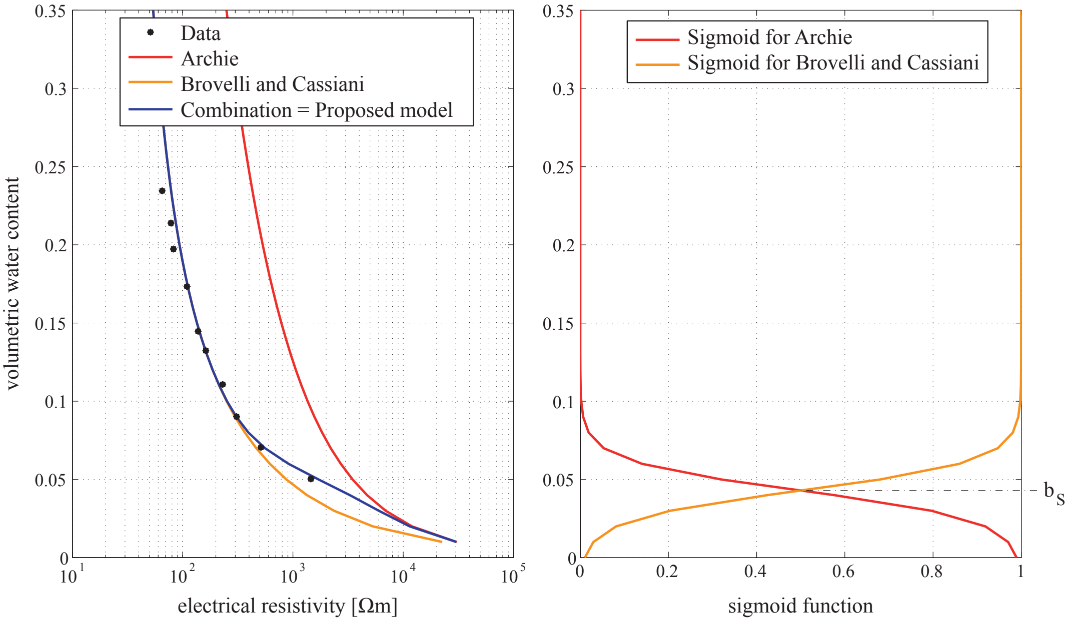

Fig. 2.12: Data with Archie and Brovelli curves and the combination of them using multiplicative sigmoid functions (left). The right side shows the two opposite sigmoid functions and the inflection point.

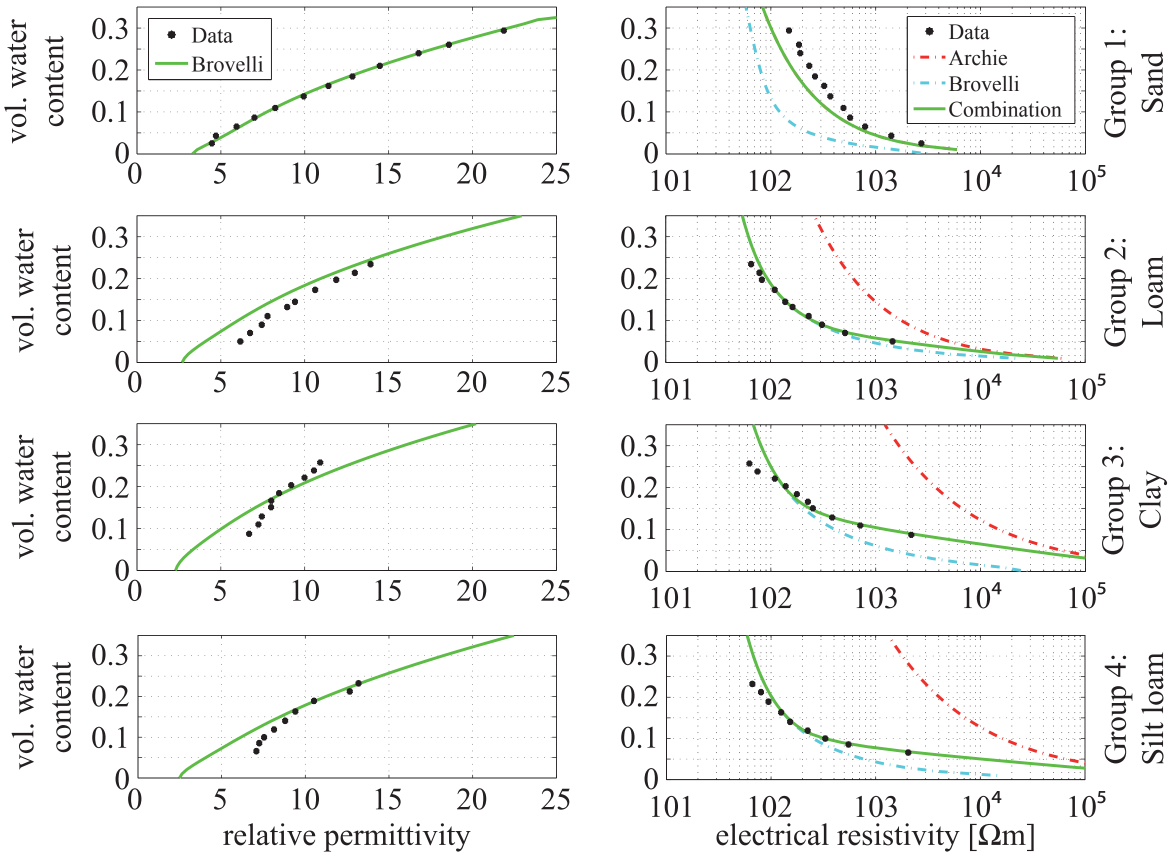

Fig. 2.13: Volumetric water content as a function of permittivity (left) and electrical resistivity (right) and best fitting model using a linear combination of Archie's law and Brovelli and Cassiani equation for the representative sample of each group. Note that for the resistivity of group 1 the Archie curve is overlain by the combination curve.

Group	RMSE(ε)	RMSE(ρ)	a_A	m_A	n_A	m_B	n_B	σ_w [mS/m]	σ_{gr} [mS/m]	a_S	b_S
1: Sand	0.030	0.054	0.41	1.31	1.49	1.34	1.72	10	15.22	169.4	0.22
2: Loam	0.047	0.020	1.08	2.27	1.60	1.30	1.98	22.92	24.45	79.52	0.03
3: Clay	0.039	0.073	1.40	2.71	1.90	1.30	1.93	19.49	20.26	109.03	0.05
4: Silt loam	0.057	0.019	1.09	2.28	1.79	1.30	1.98	25	25	205.92	0.05

Tab. 2.9: Mean absolute RMS errors and obtained fitting parameters for the proposed model for each group.

2.3.5 Relationship between electrical conductivity and relative permittivity

The data of electrical conductivity and relative permittivity for all water contents revealed an almost linear relationship. The linear correlation coefficient between conductivity and permittivity is high (R>0.89) for all samples (Fig. 2.14). Hence the relationship between both parameters can be described by a linear function of the form

$$\varepsilon = a \cdot \sigma + b, \tag{2.40}$$

where a is the slope and b the intercept. These two resulting mean parameters and the mean correlation coefficients for each group are listed in Tab. 2.10. The quality of the correlation is obviously not dependent on soil texture (i.e. mainly clay content), whereas the slope and the intercept seem to have a dependency on clay content. Fig. 2.15 a shows the intercept versus the slope for all samples. The colour indicates the clay content of the sample. Samples with high clay content have a linear relationship with larger intercept and smaller slope compared to samples with low clay content. Using these data points a multivariate regression has been performed to yield an equation describing the clay content (c_c) as a function of the slope (a) and intercept (b):

$$c_c = -4.55a + 0.02b + 14.42 \ . \tag{2.41}$$

The correlation between observed and calculated clay content is high (R=0.92) and the absolute RMS error of the clay content is 5.95% (Fig. 2.15 b).

Group	Correlation coefficient R	Slope a	Intercept b	Clay content
1: Sand	0.973	2.03	3.81	4.06 %
2: Loam	0.980	0.38	6.12	22.38 %
4:Silt loam	0.973	0.46	6.22	27.96 %
3: Clay	0.951	0.23	7.23	47.73 %

Tab. 2.10: Mean correlation coefficient, mean slope a and mean intercept b of the linear relationship between σ and ε for each group (eq. (2.40)). The groups are arranged in order of increasing mean clay content.

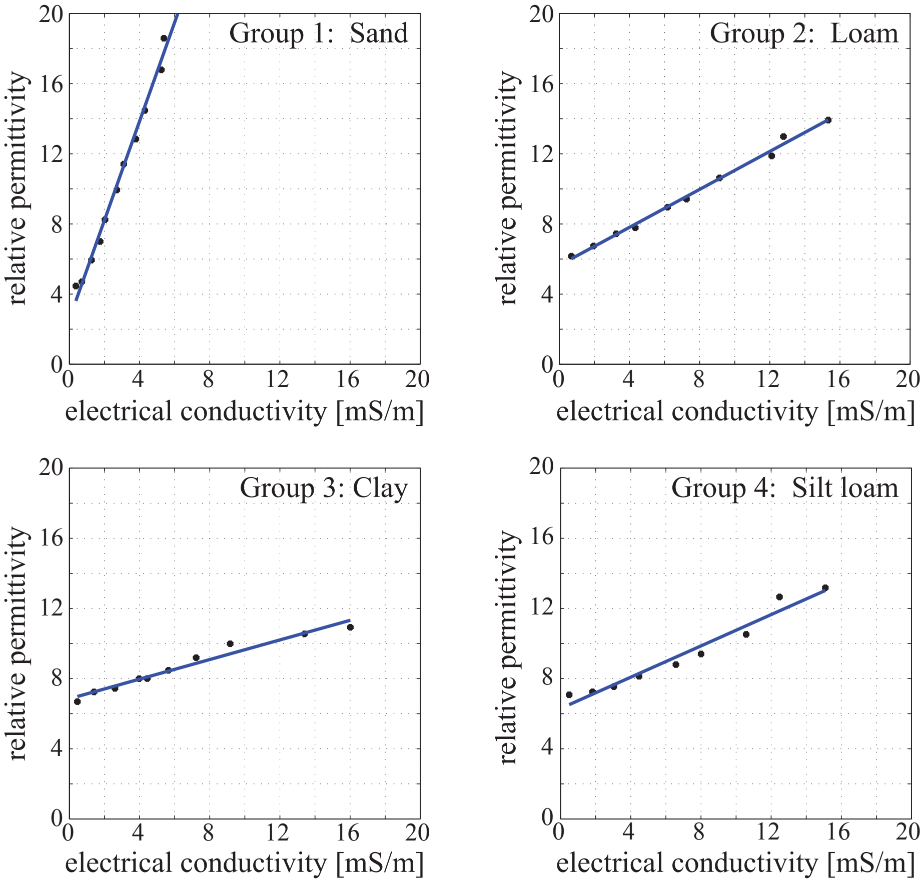

Fig. 2.14: Relative permittivity versus electrical conductivity and fitted linear relationship for the representative sample of each group.

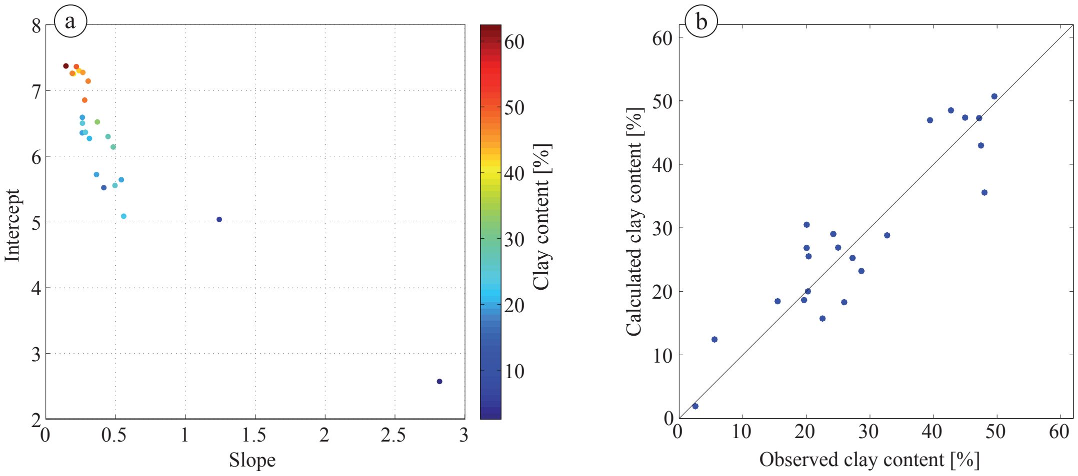

Fig. 2.15: a: The intercept versus slope of the fitted linear function colourcoded by the clay content. b: Calculated clay content (with eq. (2.41)) versus observed clay content.

2.3.6 Field test

The above-mentioned results have been found with the help of soil samples. These soil samples have been taken by digging out soil with a shovel. This destroys the soil texture and thus does not represent in-situ conditions any more. The aim of this section is to apply the results from sections 2.3.3 and 2.3.5 to field data as a test if the relationships are also valid and applicable for in-situ data.

The basis for this is an inverted geoelectric profile, from which the GPR velocity distribution can be calculated. The GPR velocity is normally measured at single points using a common-midpoint (CMP) configuration that results in spatially very sparse information. Using an inverted geoelectric profile instead gives a distribution of the electrical conductivity that can be converted into a distribution of relative permittivity and thus GPR velocity with higher resolution than can be achieved by CMP measurements.

At the field site Rosslau on the plot with the lowest clay content a geoelectric profile of 31 m length with an electrode distance of 1 m was measured. It was inverted using the Program Res-2dInv by Loke (2011) and the resulting electrical resistivity values were converted to electrical conductivity given in mS/m (Fig. 2.16 a) down to a depth of 3 m.

The first approach to convert electrical conductivity into GPR velocity is to use the obtained linear relationship between both parameters. In this case it is the one of the representative sample of group 1. The resulting distribution of relative permittivity is shown in Fig. 2.16 b and the distribution of GPR velocity in Fig. 2.16 c using equation (2.2).

The second approach uses the Brovelli and Cassiani (2010) equation with its parameters m, n, σ_w and σ_s obtained by the laboratory measurements. The underlying assumptions are that the changes of electrical conductivity and permittivity are only due to differences in water saturation and not in the soil material (i.e. clay content) and that the porosity does not change. The first step is to calculate the corresponding saturation for each electrical conductivity data point. The result is shown in Fig. 2.17 b. At locations corresponding to high electrical conductivity only saturation values larger than 1 could be obtained, which are outside the feasible range for saturation (0 to 1). This indicates that either the parameters m, n, σ_w and/or σ_s are inappropriate or that one or both of the assumptions do not hold in these areas. This could be explained by a change of porosity and/or a change of material. Nevertheless, for the remaining parts the determined saturation values are then used to calculate the permittivity distribution (Fig. 2.17 c) again using m and n and the relative permittivity of the solid material ε_s=5. The GPR velocity distribution calculated from the relative permittivity is shown in Fig. 2.17 d.

The resulting velocity distributions of both approaches show the same features, but are quite different in amplitude. Using the linear relationship the velocity does not exceed about 13 cm/ns and varies very smoothly with depth. The velocity obtained using the Brovelli and Cassiani model has much higher values, especially in the upper part, and has a relatively sharp boundary to lower values at around 1.5 - 2 m.

To validate the resulting velocities three in situ CMP (common midpoint) measurements have been performed (see locations in Fig. 2.16 and Fig. 2.17). The velocities for different depths were determined by fitting hyperbola of certain velocities to the observed reflection hyperbola. The velocities from the CMPs are shown in Fig. 2.18 as green points. The GPR velocities from the two conversion approaches are plotted as green lines for comparison. The velocity profiles calculated with the linear relationship match very well the in situ observations. The velocities from the second approach are usually too large, except of some depths from the third CMP. The absolute RMS errors between in situ and calculated velocities are 1.1 cm/ns for the first and 3.6 cm/ns for the second approach. An error of about 1 cm/ns is acceptable and is also in the accuracy range of CMP measurements, but an error of more than 3 cm/ns is too high.

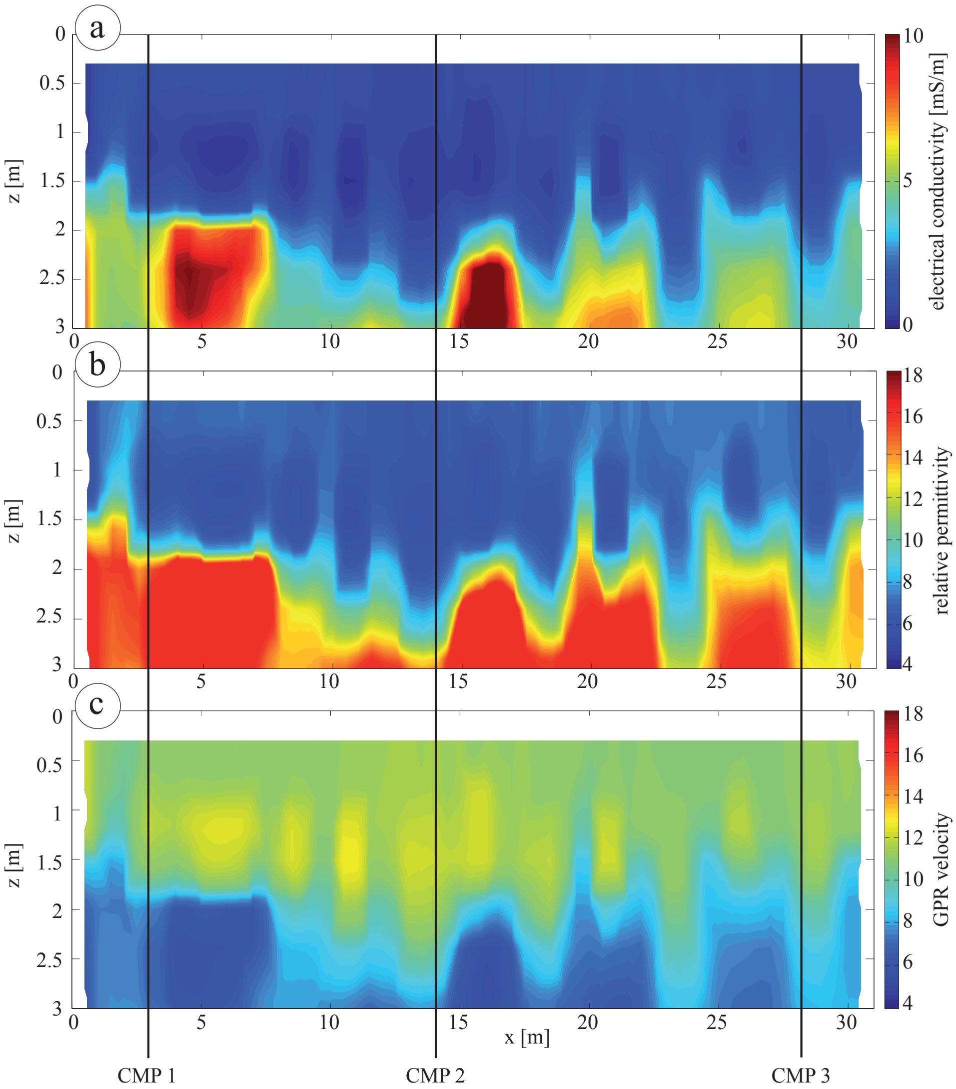

Fig. 2.16: The inverted geoelectric profile (a) is converted to relative permittivity (b) using the linear relationship obtained in laboratory and then transformed into the distribution of GPR velocity (c). Black lines mark the locations of in situ CMP velocity measurements.

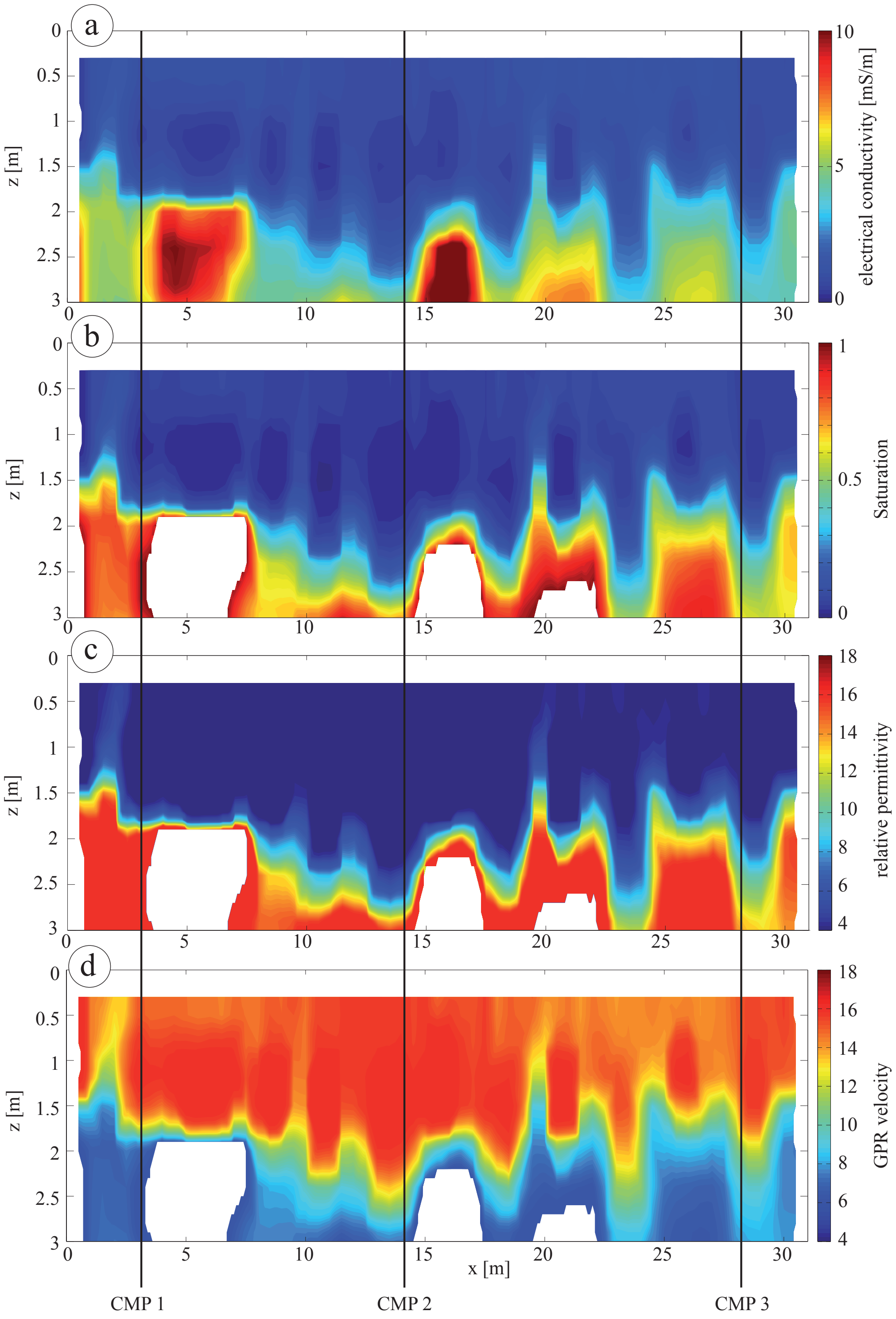

Fig. 2.17: The inverted geoelectric profile (a) is converted to saturation (b) and from that to relative permittivity (c) using the Brovelli and Cassiani model and the parameters obtained in laboratory. This is then transformed into the distribution of GPR velocity (d). Black lines mark the locations of in situ CMP velocity measurements.

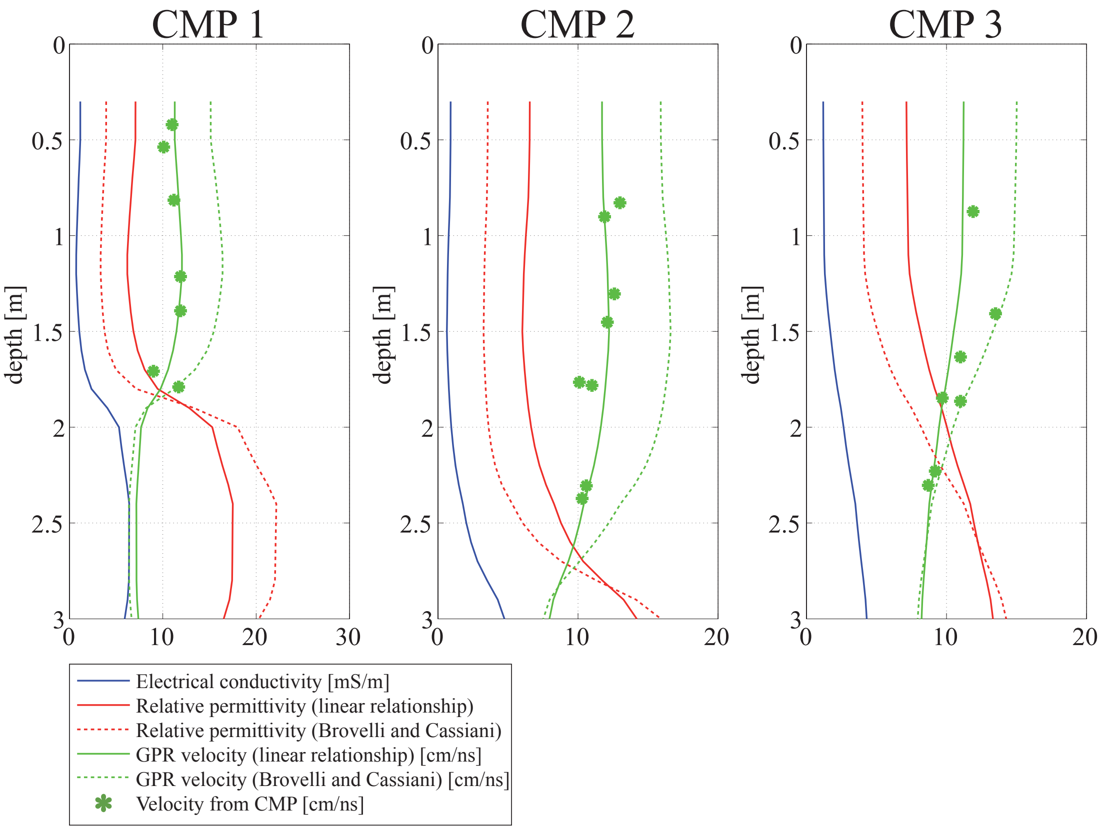

Fig. 2.18: Comparison between the calculated velocity using two approaches (green lines) and the in situ measured velocity (by CMP measurements, green *) for all CMPs. The electrical conductivity (blue lines) and the relative permittivities of both approaches (red lines) are shown for completion.

2.4 Discussion

The application of empirical, volumetric mixing and effective medium models linking electrical conductivity and permittivity to volumetric water content showed that in most cases the simpler models, i.e. the empirical or simple volumetric mixing models, yield almost as good results with respect to the RMS error as the more complicated effective medium models.
For the permittivity the volumetric mixing model for three phases with one optimal fitting parameter results in only slightly worse RMS errors (0.013-0.028) than the more complicated effective medium models (0.012-0.030). The effective medium model by Sen at al. (1981) that embeds water-coated grains into an air matrix gave the best results for all soil textures. This was also found by Steeman and Endres (2011) who investigated sand, sandy loam and silt loam soils. Their study also revealed the only slightly worse prediction of volumetric water content using volumetric mixing models in comparison to the applied effective medium models. These findings make clear that even simple pedophysical relationships are appropriate to describe the link between permittivity and water content, which is thus not strongly dependent on the geometry and hence on the soil texture (i.e. mainly clay content). Steelman and Endres (2011)

used GPR field data from different antennas and investigated the velocity of the direct ground wave to obtain the permittivity of the soil. The fact that they had similar results to the results in this study using a different method of permittivity determination confirms the reliability of the findings. Furthermore were the empirical models determined using TDR and are also satisfactorily applicable to the data from our laboratory measurements. This again confirms our way of data acquisition and processing.

For the prediction of volumetric water content from electrical conductivity Archie‘s law (Archie 1942) gave good results for sandy soil, as expected, and the empirical equation of Waxman and Smits (1968) including surface conductivity achieved very good results for the samples with non-negligible clay content. The problem using their equation is that both water and surface conductivity are unknown and have to be determined by optimisation. At the same time they are added together in the equation, which leads to an ambiguity in the determination of the parameters. The effective medium model based on Hanai (1960) and Bruggeman (1935) only gave feasible results for the sandy sample. For all other samples the optimisation procedure only gave imaginary values for the fitting parameters and even trying to fit the data by hand was not successful. This problem might be further investigated in the future.

The advantage of the effective medium model by Brovelli and Cassiani (2010) is that the same parameterisation is used to describe electrical conductivity and permittivity. Fitting both parameters simultaneously results in RMS errors that are comparable to the errors for the volumetric mixing models for permittivity, but are worse for electrical conductivity compared to the empirical equations. Nevertheless the fits are acceptable. The same parameterisation for both parameters can be used to calculate e.g. the corresponding permittivity for a given electrical conductivity. Brovelli and Cassiani (2010) used pore-scale simulations with given cementation exponent m to test the potential of their model to predict the corresponding permittivity. They found a very good agreement of calculated permittivity and simulated data. However, for real data, as in this chapter, this might be a critical task, because if no permittivity data is available and only electrical conductivity data will be used to determine the fitting parameters, these might be different from the ones determined using both data sets. Then the predicted permittivity would of course be wrong.

The obtained parameters for the sandy sample fitting electrical conductivity and permittivity simultaneously were applied to field data calculating the permittivity and thus the GPR velocity distribution from an inverted geoelectric profile. The comparison with in situ CMP velocity measurements showed that the Brovelli and Cassiani model strongly overestimates the velocity. This might be caused by violation of the underlying assumptions, i.e. that the porosity and material (mainly clay content) do not change. Better agreement was achieved by applying the linear equation linking electrical conductivity and permittivity that was derived using the laboratory measurements. The resulting distribution of GPR velocities can be used as velocity model for migration, which is only feasible for large velocity variations. For smooth velocity models the simple application of a one dimensional velocity distribution or even constant velocity is sufficient.

The linear relationship between electrical conductivity and permittivity was already observed by Malicki and Walczak (1999), Hilhorst (2000) and Persson (2002) using TDR measurements. Malicki and Walczak defined the so-called salinity index, which is the slope ($d\sigma/d\varepsilon$) of the

empirically derived linear relationship. This index can be used to determine the electrical conductivity of the pore fluid, which is assumed to be a measure of soil salinity. Hilhorst (2000) also developed a model to predict the electrical conductivity of the pore water, but based on theoretical considerations. He also stated that this model applies to free water only. Thus, as a rule of thumb, the volumetric water content has to be larger than 0.1 for the model to be valid. In our laboratory measurements we used rain water for saturation with more or less equal electrical conductivity (10-25 mS/m). Nevertheless the slopes of the observed linear relationships are quite different and are dependent on clay content. This might be explained by soluble components in the soil matrix, such as residual salts, carbonates or silica (Malicki and Walczak 1999) that increase the electrical conductivity of the pore fluid. Malicki and Walczak found that the slope $d\sigma/d\varepsilon$ is dependent on sand content, which is almost inversely proportional to the clay content, that was also observed in our results.
The newly developed model that describes the electrical conductivity with a combination of Archie‘s law for low water contents and the Brovelli and Cassiani model for higher water contents gave satisfactory fits, but no major improvement of the RMS error appeared in comparison to the single models. Nevertheless, in the lower water content range the shape of the new curve for electrical conductivity agrees better with the measured data than the original Brovelli and Cassiani equation, because the transition to Archie‘s law in this range leads to stronger bending of the curve.

Regarding the procedure of the laboratory measurements there are some critical points to be discussed. One is the change of porosity that occurred during the measurements at different water content steps, because the sample had to be taken from the cylinder, to be mixed and then filled back inside. Due to the partly large content of fine grains (i.e. clay and silt) this was not easy and differences in the fill height occurred, which led to a change of porosity. As a worst case scenario this might lead to an uncertainty in relative permittivity of about 5 % and in electrical conductivity of 3 %, which are acceptable and might also occur due to measurement and processing errors. The second critical point is the mixing of the soil samples that of course destroyed the internal structure of the soil. Thus the electromagnetic behaviour of the sample must not be that of the soil in situ. Nevertheless this factor does not seem to have a large influence, because the results are comparable to findings in literature as already mentioned earlier.

2.5 Conclusion

Laboratory measurements of electrical conductivity and permittivity have been done on 23 samples of different soil texture. The samples were saturated with rain water in steps of 2-3 vol% and the geophysical parameters have been measured for each step. Several models linking electrical conductivity and permittivity to volumetric water content have been applied to the data to test their feasibility in predicting the water content from geophysical measurements. Using permittivity easily applicable volumetric mixing models gave good results with mean absolute RMS errors between 0.013 and 0.028 compared to slightly better fits using a more complicated effective medium model. Thus the influence of geometric factors, as accounted for in the effective medium models, seems to have a negligible effect. Regarding the electrical conductivity the simple empirical models yielded better RMS errors for the prediction of the volumetric water content than an effective medium model, e.g. from Brovelli and Cassiani (2010). The advantage of this second model is the same parameterisation for permittivity and electrical conductivity that can be used to determine the other parameter if only one is known. For the laboratory data this worked well, whereas an application of this relationship to field data gave no satisfactory result. A linear relationship between electrical conductivity and permittivity was observed that can be used to determine the permittivity and thus the GPR velocity distribution from an inverted geoelectric profile, which was successfully demonstrated using field data.

3. Influences of clay and water content on the shape and amplitude of GPR signals

3.1 Introduction

The attenuation of electromagnetic waves and, thus, the penetration depths of GPR reflection measurements are highly influenced by particle size distribution and water content of soils. In areas with high water content and/or high clay content electromagnetic waves will be strongly attenuated, mainly due to increased electrical conductivity. Other factors in GPR attenuation are losses from scattering, which will not be considered in this chapter, and relaxation losses of the dielectric polarisation that are quantified by the imaginary part of permittivity. The real part of permittivity is the main factor determining propagation velocity of electromagnetic waves.

Both real and imaginary parts of permittivity and electrical conductivity are strongly influenced by water content. Additionally, electrical conductivity will not only be increased by water content, but also by clay content due to the surface conductance of clay minerals. Soils with higher clay content will also have a higher amount of bound water, which in turn has a different permittivity than free water. All these factors will influence the wavelet of GPR reflections in time delay, amplitude and shape.

The quality factor Q, which is well known from seismic applications (e.g. Tonn 1991), can be determined from changes of the wavelet amplitude and signal shape along the travel path of the GPR wave. It characterises the ratio of energy gained and lost of a soil sample (Liu et al. 1998). The Q factor can be regarded as an additional independent physical parameter that can be used to characterise soils. The imaginary part of permittivity describing the relaxation of polarisation can then be determined from Q in combination with the electrical conductivity measured at very low frequencies.

Because all these influencing factors are interconnected, the aim of this study is to investigate their relationships under controlled conditions. We conducted laboratory measurements on 23 large soil samples (about 50 kg each) taken from field sites with different soil types. Electrical conductivity and GPR velocity were measured routinely on all soil samples at several steps of water content. The direct and reflected waveforms were then used to determine the Q factor for different water and clay contents based on the spectral ratio method. The relationship between these parameters is quantified by an empirical multivariate function. The results are evaluated by forward modelling of synthetic radargrams and by analysing the decay of the frequency of the spectral maximum amplitude based on a simplified theoretical approach.

The study aims to improve the quantitative understanding of the relationships between soil parameters and geophysical field observables. It suggests the application of the Q factor and the imaginary part of permittivity as further diagnostic parameters to determine water and clay content in situ.

3.2 Methodology

3.2.1 Measurement procedure

The measurement procedure in the laboratory is the same as explained already in the previous chapter. The final output is the electrical conductivity and permittivity for each sample at several water content steps and the recorded waveforms of the GPR reflections. The clay content was determined by standard laboratory procedures performed at the Helmholtz Centre for Environmental Research (UFZ), Leipzig.

3.2.2 Electromagnetic Properties

The two real parameters representing lost and stored energy at a specific angular frequency ω are the effective permittivity and effective conductivity, defined as

$$\varepsilon_{ef}(\omega) = \varepsilon'(\omega) + \frac{\sigma''(\omega)}{\omega} \tag{3.1}$$

and

$$\sigma_{ef}(\omega) = \sigma'(\omega) + \omega\varepsilon''(\omega) \, , \tag{3.2}$$

where $\varepsilon'(\omega)$ and $\sigma'(\omega)$ are the real parts of dielectric permittivity and electrical conductivity, and $\varepsilon''(\omega)$ and $\sigma''(\omega)$ are the respective imaginary parts (e.g. Knight and Endres 2005).
$\varepsilon'(\omega)$ is the dielectric polarisation including electronic polarisation, molecular polarisation and orientational polarisation (Powers 1997), whereas the imaginary part of permittivity, $\varepsilon''(\omega)$, represents the energy loss by polarisation relaxation (Knight and Endres 2005). The real part of electrical conductivity, $\sigma'(\omega)$, defines ohmic conduction and the imaginary part, $\sigma''(\omega)$, Faradaic diffusion caused by induction (Knight and Endres 2005; Klitzsch 2004). All these parameters are frequency dependent, but for high frequencies, as in GPR applications, $\sigma''(\omega)$ can be assumed to be negligible and $\sigma'(\omega)$ to be the DC conductivity (Knight and Endres 2005). Thus equations (3.1) and (3.2) reduce to

$$\varepsilon_{ef}(\omega) \approx \varepsilon'(\omega) \tag{3.3}$$

and

$$\sigma_{ef}(\omega) = \sigma_{DC} + \omega\varepsilon''(\omega) \, . \tag{3.4}$$

The propagation velocity of electromagnetic waves can be approximated by

$$v \approx \frac{c}{\sqrt{\varepsilon_r}} \, , \tag{3.5}$$

where c is velocity of light, $\varepsilon_r = \varepsilon'/\varepsilon_0$ is relative permittivity and $\varepsilon_0 = 8.85418782 \cdot 10^{-12}$ F/m is the permittivity of free space.

3.2.3 Quality factor

The effective permittivity represents all energy stored and the effective conductivity all energy lost. The quality factor Q is now defined “as the ratio of total energy restored and the energy loss in one cycle” (Liu et al. 1998):

$$Q = \frac{\omega \varepsilon_{ef}(\omega)}{\sigma_{ef}(\omega)} \approx \frac{\omega \varepsilon'(\omega)}{\sigma_{DC} + \omega \varepsilon''(\omega)} \quad . \tag{3.6}$$

Equation (3.6) shows that Q is frequency dependent. But many publications assume a constant Q corresponding to a linear dependence of the exponent of attenuation on frequency in the GPR frequency range (e.g. Turner and Siggins 1994, Bano 1996, Liu et al. 1998, Grandjean et al. 2000, Irving and Knight 2003). A frequency independence of Q can be justified by having a closer look at the single terms of equation (3.6). Because we are working at high frequencies and relatively low electrical conductivities, we can assume that $\omega\varepsilon''(\omega)$ dominates over σ_{DC}. Taking $\varepsilon'(\omega)$ and $\varepsilon''(\omega)$ to have the same frequency dependence (Jonscher 1977) leads to a frequency independent quality factor. The validity of these assumptions is confirmed below by the spectral analysis included in the spectral ratio method of the Q determination..

The quality factor Q is well known in seismic data processing (e.g. Tonn 1988). But also in GPR it has been widely used for characterising dielectric loss or attenuation and wavelet dispersion of electromagnetic waves (e.g. Turner and Siggins 1994; Bano 1996; Liu et al. 1998; Irving and Knight 2003).

Tonn (1988, 1991) provides a comparison of different methods of determining Q from seismic data. These methods were applied to synthetic and real data providing information about the usefulness and applicability to different sorts of seismic data. The considered methods can be divided into time domain (amplitude decay, analytic signal, risetime) and frequency domain methods (spectral ratio). Most of the time domain methods suffer from instability or have the tendency to be biased by the choice of processing parameters. Also, the assumption of a constant Q underlying the standard methods needed to be checked in our case during the interpretation. Regarding these aspects, the spectral ratio method appeared to be the most adequate. The results of Tonn on the reliability of Q determination are based on seismic data and should not be transferred directly to GPR. Therefore, the results of the spectral ratio method were to be checked by independent forward modelling after the inversion.

In the spectral ratio method Q is determined by comparing a wavelet before and after its passage through an absorbing medium. In praxis, the reference wavelet at the starting point is usually determined from the recorded direct wave that is spectrally compared to a reflected wavelet affected by absorption. Both wavelets have to be cut out from the recorded trace and transformed into frequency domain using a discrete Fourier transform. The frequency spectra of reference wavelet ($A_0(\omega)$) and reflection ($A_1(\omega)$) are now available for every angular frequency $\omega = 2\pi \cdot f$. Plotting the logarithm of the ratio of the amplitude spectra versus angular frequency results in a function that can be fitted by a straight line if Q is constant. Fig. 3.1 shows an example of this sort of curve. For frequencies smaller than about 0.6 GHz and higher than 1.6 GHz the fitted line deviates from the calculated values, which is possibly caused by the band limitation of the source signal. Therefore, the results apply to a frequency band of 0.6 to 1.6 GHz. The linear equation, describing the spectral ratio of the reflected and reference signal for constant Q media, was derived by Bath (1974) and reads

$$\ln\left(\frac{|A_1(\omega)|}{|A_0(\omega)|}\right) = \ln\left(\frac{|A_{0,1}(\omega)|}{|A_{0,0}(\omega)|}\right) - \frac{\Delta t}{2Q} \cdot \omega \,, \tag{3.7}$$

where Δt is the traveltime difference between reference and reflection. The first part on the right hand side of equation (3.7) is the amplitude ratio at zero frequency and can be derived from the intercept. The slope is simply the ratio of traveltime difference and two times Q. Thus Q can be calculated directly from the slope of the fitted line. Using only points between 0.6 and 1.6 GHz for fitting, the correlation coefficient is between 0.861 and 0.999 (average 0.99) for all samples, which indicates a reliable matching and confirms that Q is indeed constant in this frequency band.

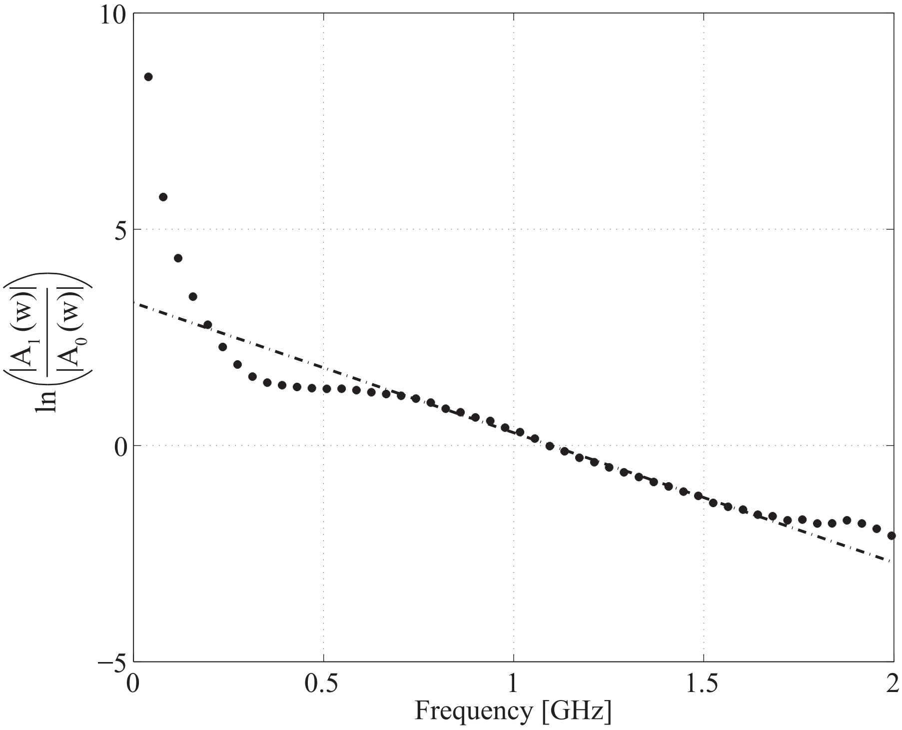

Fig. 3.1: Logarithm of spectral ratio versus frequency (dots) with fitted line (dashed). Note that x-axis is simple frequency and not angular frequency (for display purposes only).

In the present study a special problem consisted in determining an appropriate reference signal. In many cases the isolated ground wave or the first derivative of it can be used (e.g. Bano 2004; Bradford et al. 2009). However, because of the small dimension of the laboratory equipment we measured the interference of air and ground wave. Direct air and ground wave have the same shape (with opposite polarity) and resemble that of the initial wavelet. The shape of the reflection includes a time derivative of the initial wavelet (van der Kruk and Slob 2002; Dai and Young 1997). Therefore, we performed an extra measurement where we recorded the direct airwave isolated at 1 m above the ground. The time derivative of this airwave was then used as a reference wavelet. The reference wavelet and its amplitude spectrum are shown in Fig. 3.2. By this approach only the waveform of the reference signal is reliably determined, whereas the absolute amplitudes are not comparable. However, this is not a critical point. Since the spectral ratio method relies only on the change of ratios with frequency, neither the absolute amplitudes of the reference nor of the reflected wavelet need to be known.

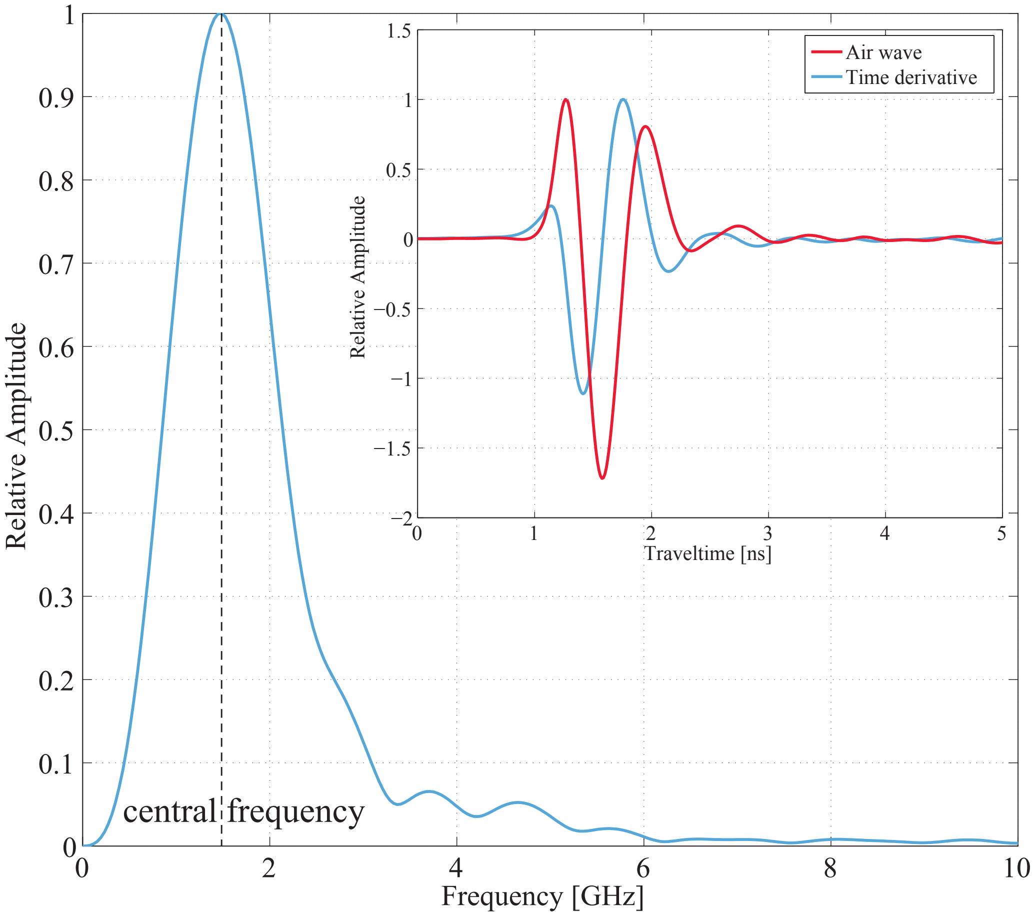

Fig. 3.2: Amplitude spectrum of the first derivative of the direct air wave with central frequency of about 1440 MHz. Inset shows time-domain representation of air wave and its time derivative.

3.2.4 Influence of attenuation on wavelet amplitude and frequency content

The influence of the clay and water content of soils on the shape of the GPR wavelet is illustrated in Fig. 3.3. It shows on the left two traces measured on the same sample at different water contents and on the right two traces measured on samples with different clay but the same water content. The first wavelet of each trace is the interference of direct air and ground wave (green circle). The time of the first break of this wavelet is later than the theoretical traveltime of air and ground wave due to coupling effects (Yelf and Yelf 2006). The reflection is marked with a second circle. The arrival time of the reflection increases with increasing water content. For the same water content, but different clay contents the arrival time does not change visibly (Fig. 3.3 right). But obviously the amplitudes of the reflection attenuate rapidly with increasing clay content and also slightly with increasing water content. This indicates that ε' and Q are affected differently by the clay and water contents of the soil samples.

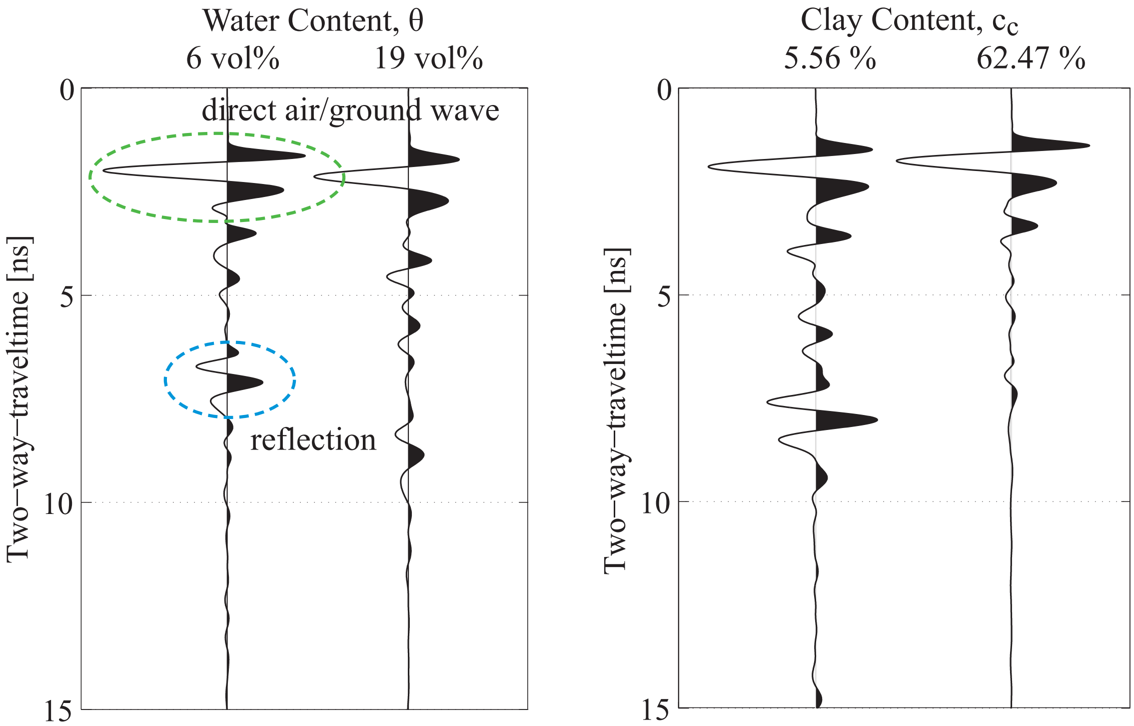

Fig. 3.3: Measured GPR traces on the same soil samples at different water contents (left) and from different samples at the same water content (right). The interference of direct air and ground wave and the reflected wavelet are marked with dashed circles.

Fig. 3.4 compares three spectra of reflected wavelets measured on the same sample at different water contents. The central frequency for the wavelet at lowest water content is about 1200 MHz, at medium water content about 1000 MHz and at highest water content about 820 MHz. There is also a remarkable decrease in amplitude of all frequencies. In order to quantify the frequency shift of the maximum amplitude we approximate the source spectrum prior to attenuation by a bell-shaped Gauss function (e.g. Bronstein et al. 2001)

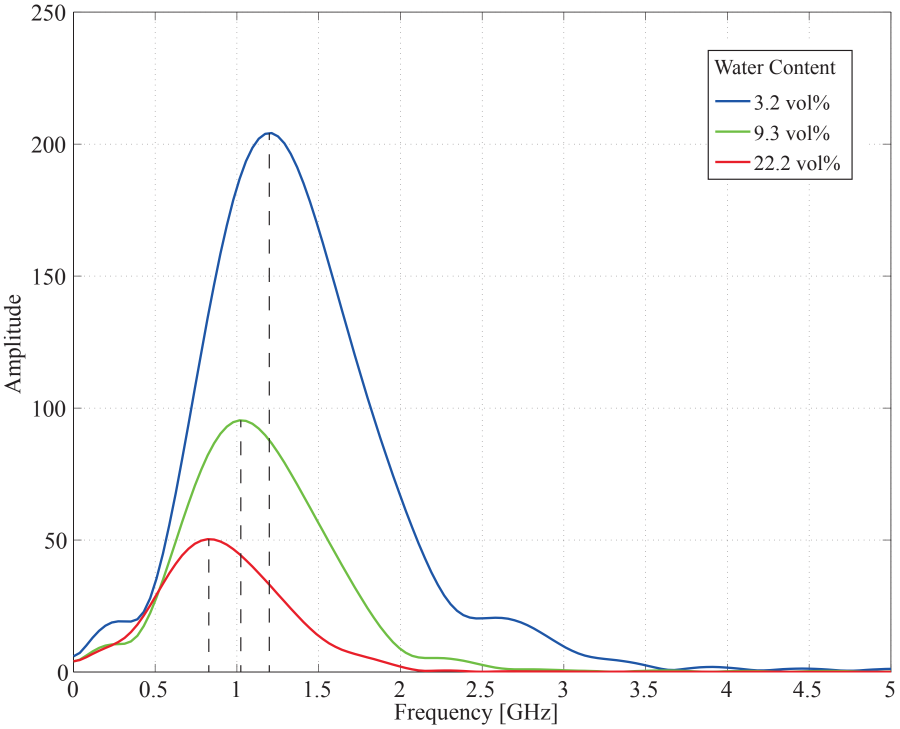

Fig. 3.4: Amplitude spectra of the reflected wavelets measured on the same sample at different water contents. Dashed lines indicate central frequencies.

$$A(f) = A_0 \cdot e^{-\frac{\pi^2 (f-f_0)^2}{\gamma^2}} \quad , \tag{3.8}$$

where γ is the width of the curve (in Hz) and f_0 is the frequency (in Hz) corresponding to the maximum amplitude A_0 (Fig. 3.5).

The attenuation of the electromagnetic waves along a travel distance Δx is described by the attenuation coefficient α and another exponential function modifying the spectrum (Turner and Siggins 1994) in the following way (Fig. 3.5):

$$A(f) = A_0 \cdot e^{-\frac{\pi^2 (f-f_0)^2}{\gamma^2}} \cdot e^{-\alpha \cdot \Delta x} \quad . \tag{3.9}$$

For Q≈const. the attenuation coefficient α can be written as (Turner and Siggins 1994)

$$\alpha = \frac{\pi \cdot f}{Q \cdot v} \; . \tag{3.10}$$

After substitution of α equation (3.9) becomes

$$A(f) = A_0 \cdot e^{-\frac{\pi^2 (f-f_0)^2}{\gamma^2}} \cdot e^{-\frac{\pi \cdot f}{Q} \cdot \Delta t} \quad , \tag{3.11}$$

where Δt is the travel time of the wavelet along ray segment Δx. The central frequency f_c of the attenuated wavelet can be easily determined by calculating the zero point of the first derivative of equation (3.11). This results in

$$f_c = f_0 - \frac{\gamma^2}{2\pi} \cdot \frac{\Delta t}{Q} \quad . \tag{3.12}$$

This equation explains the decrease of signal frequency by absorption as function of travel time and Q. It can be used to estimate Q from field data if the f_0 and γ of the emitted signal are determined by extra measurements in a non-attenuating medium. The underlying assumption of a bell-shaped spectrum is not a serious restriction because the emitter spectrum needs only to be fitted on the low-frequency side near the maximum.

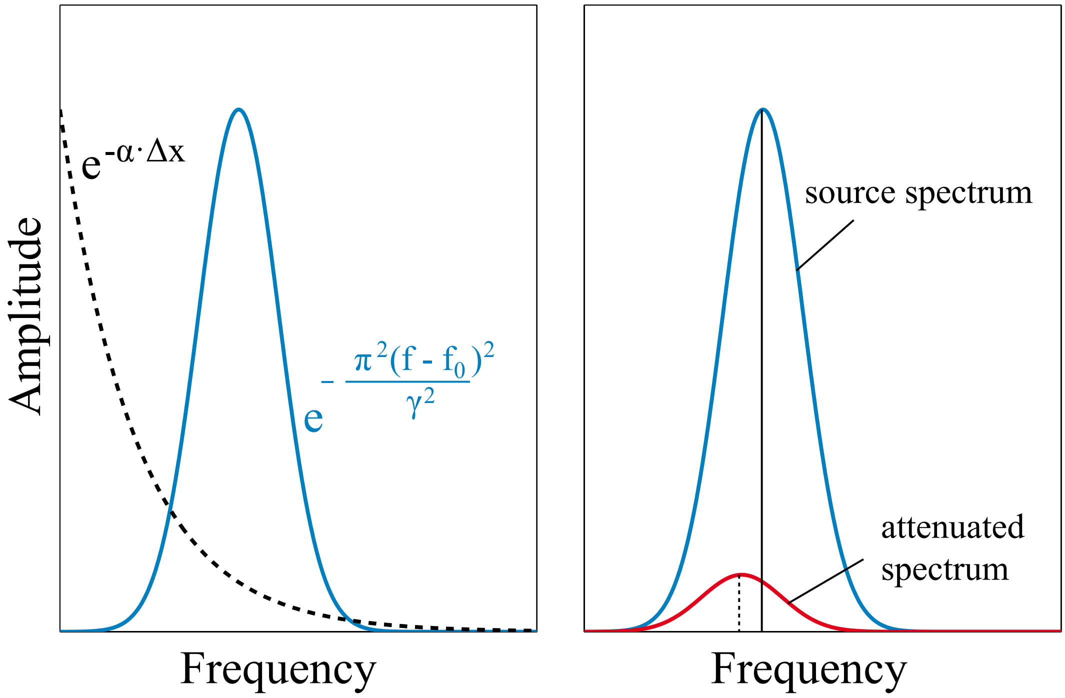

Fig. 3.5: Source spectrum (left, solid line) and attenuation exponential function (left, dashed line) are multiplied to result in the attenuated spectrum (right, red line). The attenuated spectrum has lower maximum amplitude and corresponding frequency than source spectrum (right).

3.3 Results

3.3.1 Quality factor

The spectral ratio method was applied to determine Q of all samples at all water content steps. The observed Q values range from 5 to 15. Exemplary results for samples with low, medium and high clay contents are shown in Fig. 3.6 (left). The sample with low clay content (2.55 %)

shows the highest Q values of the data set. Starting at Q≈15 at minimum water content they decrease to 10 at about 30 vol% of water. The samples with medium clay content (20%) show significantly lower Q values between 10 and 7; for the high clay content samples (62%) Q-values are between 7 and 5.

In order to quantify the observed relations, a multivariate fitting function was applied to the data of Q, volumetric water (θ) and clay content (c_c). Based on least-squares fitting following relation was obtained:

$$\ln(Q) = -0.10 \cdot \ln(\theta) - 0.16 \cdot \ln(c_c) + 3.34 \;. \tag{3.13}$$

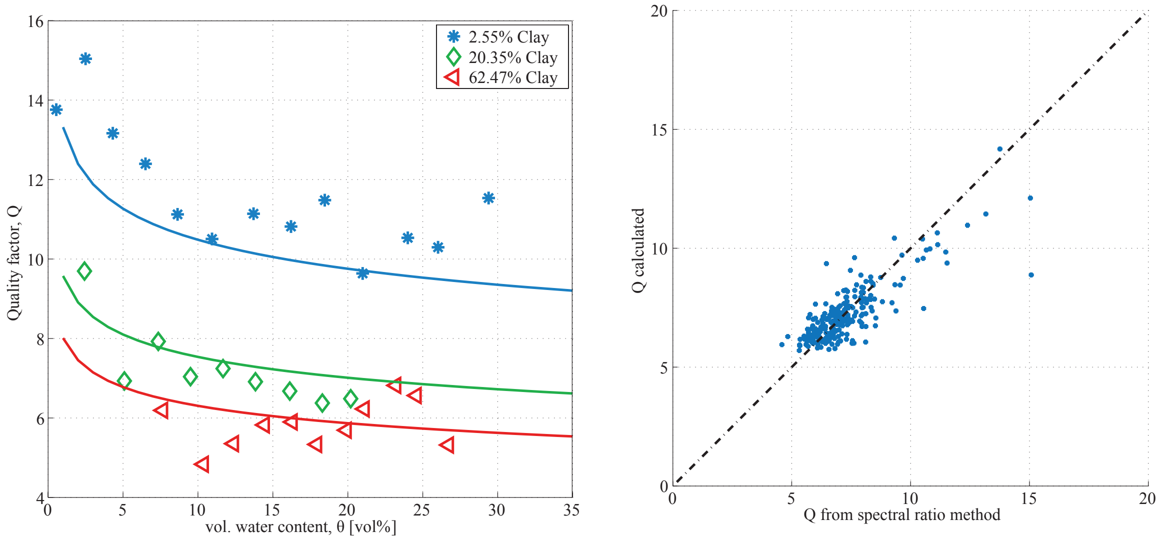

Fig. 3.6: Quality factor versus volumetric water content for low, medium and high clay content samples and fitted curves (left). Correlation between Q derived from spectral ratio method and the calculated Q using equation (3.13) is shown on the right side.

The RMS error of this fit is 9% (Fig. 3.6 right). From the scattering of the measured Q-values with respect of the regression lines the estimated uncertainty of the Q measurements is of the order of δQ ≈ ±1. An inspection of the data showed that the scattering of the Q values is not caused by irregularities in the fitted linear section of the spectral ratio function, but rather by inaccuracies in the identification and extraction of the reflected wavelets from the measured trace. This difficulty occurs in particular at high absorption as is evident from the strong scattering of data points of samples with high clay content (Fig. 3.6). Some inaccuracies may be caused also by the interference of the analysed reflection with arrivals scattered inside the soil container.

3.3.2 Frequency content of wavelets

The absorption leads to strong shifts in the central frequencies of the reflected GPR signals that are shown for all combinations of clay and water content in Fig. 3.7. In order to validate the observed frequency shifts we applied the empirically determined relationship (3.13) linking volumetric water and clay content to Q and computed the expected central frequencies according to equation (3.12). The emitted central frequency f_0 and γ were determined from the first derivative of the direct wave through air (see section on measurements above). A comparison of the observed and calculated central frequencies is shown in Fig. 3.8. The values correlate well in tendency (correlation coefficient 0.9) but show significant scattering of the order of 10% corresponding to the scattering of the Q values. The basic outcome of this part of the study is that the observed frequency shifts and Q values are compatible with each other, and that the frequency shift may be used to estimate Q from GPR field measurements, too.

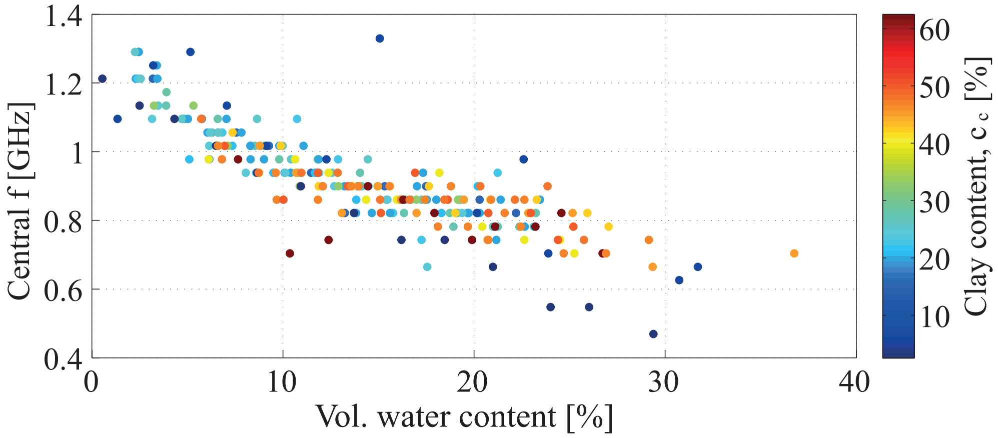

Fig. 3.7: Central frequency versus volumetric water content. The colours represent clay content of the samples.

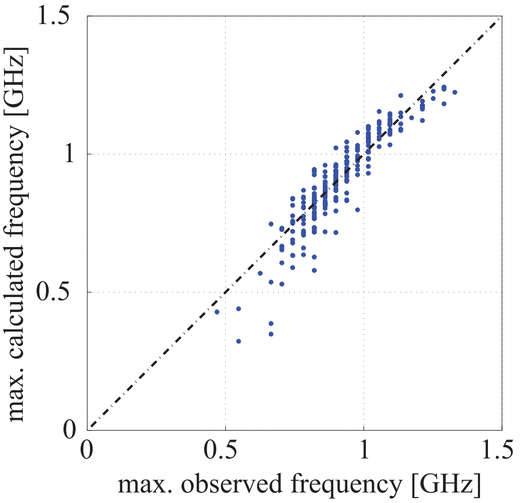

Fig. 3.8: Correlation between observed and calculated central frequencies.

3.3.3 Complex permittivity

Once the Q values and electrical conductivity have been determined it is possible to calculate the losses in polarisation expressed by equation (3.6). The relative values determined for our dataset vary between 0 and 3 (Fig. 3.9 left). The relation of ε” and ε’ is basically linear. The increase of the real part of permittivity results from an increase in the total (free and bound) volumetric water content. In particular, lower ε’ corresponds to a lower content of pore water. The linear increase of the loss in polarisation with water content, expressed in terms of ε”, is not surprising because water is a highly polarisable molecule. The more water molecules are available the more energy may be lost in a polarisation cycle.

The influence of the clay content on ε” is shown in Fig. 3.9 (right) where the graphs of three different soil samples are shown in detail. Obviously, the sample with the highest clay content shows a higher ε” to ε’ ratio than the samples with lower clay content. The ε”-ε’ relation remains linear in all cases. Therefore, a linear approach can be used to fit the observed ε”-ε’ data where the linear constant depends on the clay content only. In this approach the effect of total (free and bound) water content is contained in the varying ε’. After some trials with different types of functions the following type of equation appeared suitable that considers the varying clay content c_c in form of an exponential function:

$$\varepsilon'' = 0.19 \cdot \varepsilon' \cdot c_c^{0.15} - 0.23 \quad . \qquad (3.14)$$

The correlation coefficient between observed ε“ values and values calculated from equation (3.14) is 0.90 (Fig. 3.10). The width of the data cloud (Fig. 3.10) shows that the uncertainty of ε” values is of the order of ± 10%.

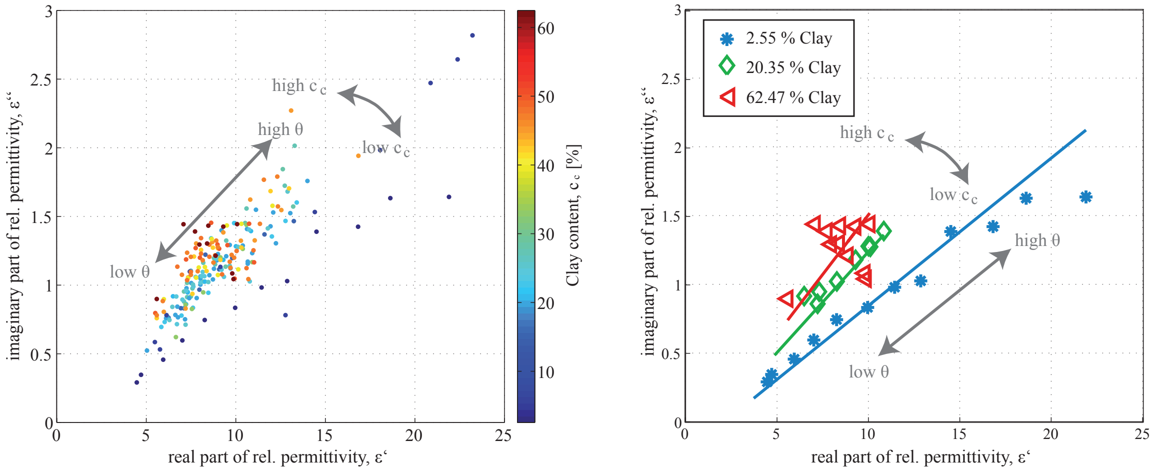

Fig. 3.9: Imaginary part of relative permittivity (ε“) versus real part of relative permittivity (ε‘) for all samples calculated using equation (3.6) and Q from spectral ratio method (left) and three exemplary samples with fitted curves (right).

Our finding agrees with Peplinski et al. (1995) who stated that the increase of ε“ with increasing clay content is an effect of the bound water. Clay has a large surface area that holds the water by negatively charged particle surfaces. Since bound water has a higher ε“ than free water, an increasing clay content will result in an increasing ε“ even if the total water content is constant (Peplinski et al. 1995).

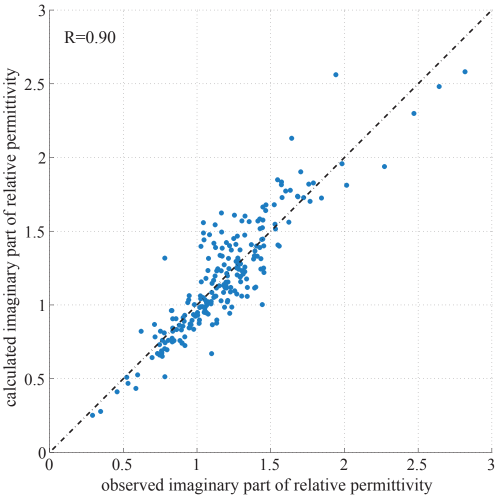

Fig. 3.10: Correlation between observed (using Q from spectral ratio method and equation (3.6)) and calculated (using equation (3.14)) imaginary part of permittivity for all samples.

3.3.4 Application to field data

On a plot with very low clay content in situ CMP (common midpoint) GPR and geoelectrical measurements have been performed. The radargrams of 400 MHz antennas show clear reflections that can be used to determine the velocity of electromagnetic waves. The geoelectric profile was inverted using Res2dInv by Loke (2011) to yield the distribution of electrical conductivities. Fig. 3.11 (left) shows an example of a CMP radargram with marked reflection and reference wavelets as well as the hyperbola that was used for velocity determination. The transformation into frequency domain reveals a frequency shift between the derivative of the reference and the reflection (Fig. 3.11 right).

Three approaches have been tested to determine the clay content of this plot from in situ measurements. The first is the spectral ratio method to determine the quality factor Q, which is found to be ≈ 13. The logarithmic spectral ratio and thus the quality factor is found to be constant between 200 to 600 MHz (Fig. 3.12). Using equation (3.6) the imaginary part of permittivity is determined and the clay content is then calculated with equation (3.14). The predicted clay content is 1.5 %, which is smaller than the true value (2.55 %), but resembles the approximate order of magnitude.

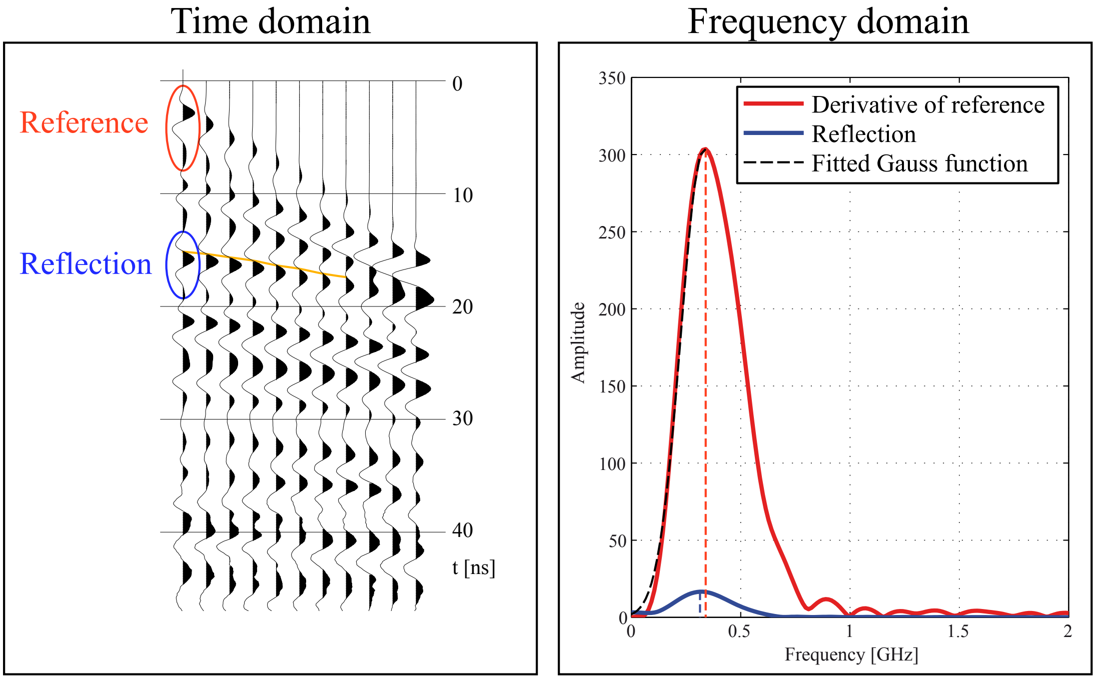

Fig. 3.11: Radargram of a CMP measurement with marked reference and reflected wavelets (left). The hyperbola for the velocity determination is indicated by a yellow line. The right side shows the frequency spectra of the first derivative of the reference (red), the reflection (blue) and the fitted Gauss function (dashed black).

The second approach uses the frequency shift between reference and reflection to calculate the quality factor with the help of (3.12). The required parameter γ is determined by fitting the bell-shaped Gauss function (3.8) to the left part of the reference spectrum (Fig. 3.11 right). Then again the imaginary part of permittivity and the clay content are calculated as explained before. The predicted clay content with this method is ≈ 0 %, which is much too small. This wrong value might result from inaccuracies in wavelet extraction and/or the interference of other waves. Additionally the problem of choosing the proper reference wavelet occurs, which might be even more problematic in this approach, because only a single frequency is investigated. In contrast, the spectral ratio method uses a broad frequency band and thus might be not as sensitive to the choice of the reference wavelet as the central frequency shift approach.

The third approach uses the instantaneous frequency to determine the frequency downshift. The instantenous frequency is a complex trace attribute, which is often applied in seismic studies (e.g. Taner et al. 1979, Barnes 2007) and gives the frequency at any time of the trace. Because it is obtained by the derivation of the instantaneous phase it is very sensitive to (numerical) noise. This causes a raw instantaneous frequency curve with a lot of jumps and outliers (Fig. 3.13, black curve). Two successive median filters of window lengths 2.5 ns and 5 ns are then applied to flatten the curve (blue curve). The examined part between 10 and 55 ns is then fitted by a linear function (red dashed curve). Its slope gives the term $(f_0-f_c)/\Delta t$ in equation (3.12) to calculate the quality factor. The parameter γ is again determined by fitting a Gauss function to the left side of the reference spectrum. The resulting quality factor ($Q\approx18$) is then used to calculate the imaginary part of permittivity and the clay content. Using this method the predicted clay content is 0.25 %, which is lower than the true one, but again reflects the right order of magnitude. Of course this value is strongly dependent on the time interval of the instantaneous frequency, which is used to fit the linear function, and on the proper filterung of the instantaneous frequency.

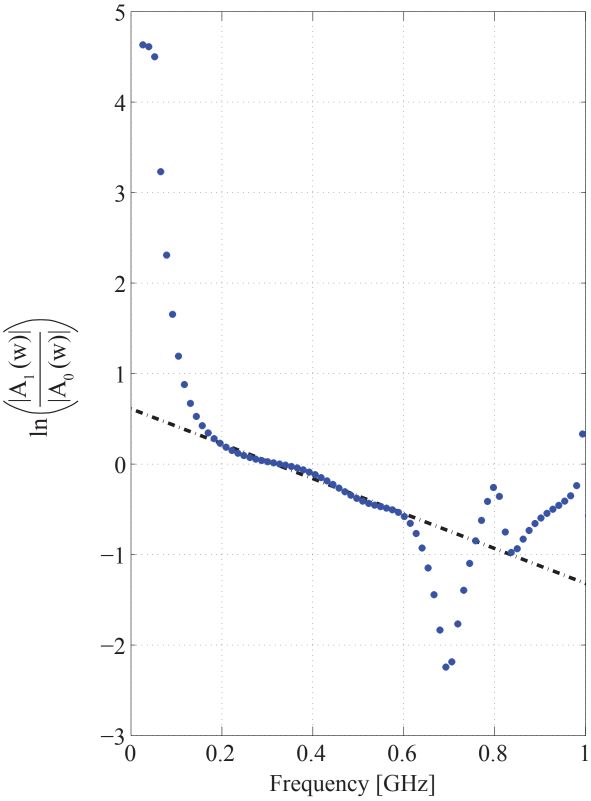

Fig. 3.12: Logarithm of the spectral ratio for one CMP with fitted line. The Note that x-axis is simple frequency and not angular frequency (for display purposes only).

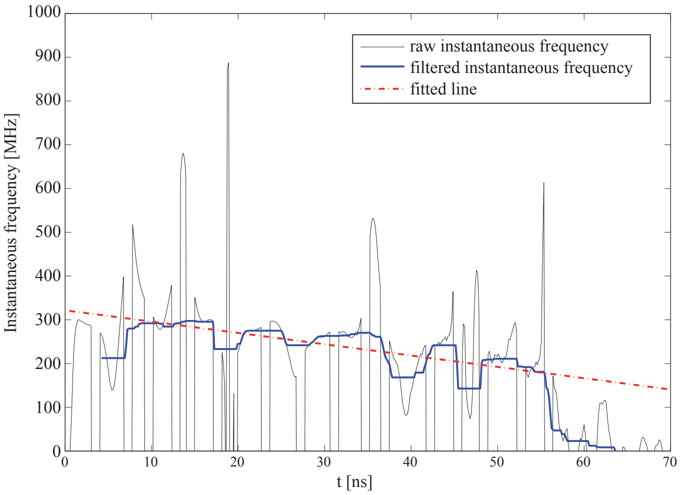

Fig. 3.13: Raw and median filtered instantaneous frequency of the first CMP trace with fitted line between 10 and 55 ns.

3.4 Discussion

The basic outcomes of the study are the empirical equations (3.13) and (3.14) that may help to determine the clay and water content in situ from combined GPR and electrical conductivity measurements. The underlying Q and ε'' values are of the same order of magnitude that were found for soils ranging from sandy loam to silty clay by Dobson et al. (1985), soils ranging from sand to clay by Wang and Schmugge (1980), a silty clay loam by Schwartz et al. (2009) and the general range for Q in GPR given by Turner and Siggins (1994).

Regarding field measurements it is of practical importance that the absorption of soils can be approximated by a constant Q approach over a wide range of frequencies (0.6 to 1.6 GHz for a 1.6 GHz antenna and 200 to 600 MHz for a 400 MHz antenna). Similar findings were published previously by Turner and Siggins (1994), Bano (1996) and Irving and Knight (2003). Bano (1996) also showed that the assumption of a constant Q model agrees with the description of the dielectric permittivity using a complex power-law function such as the Cole-Cole model (Cole and Cole 1941). The finding that Q is constant in the considered soils is in contrast to the findings of Hollender and Tillard (1998). However, these results apply to hard rock samples only and thus are not comparable to our soil samples.

Equation (3.14) shows that it is possible to determine the clay content of a sample if ε‘ and ε“ are known. Regarding large scale investigations of agricultural sites this finding promises great progress, but the applicability has to be verified in the future using an independent data set. The first application to field data gave promising results using the spectral ratio method or the instantaneous frequency at least to determine the order of magnitude of the clay content. A point that plays a role in this context is that the empirical relations may depend not only on grain size but on clay mineralogy, too. This issue still has to be investigated. Clearly, it has to be emphasized that in situ mapping of the clay and moisture contents based on GPR and conductivity data will always have to be complemented by some soil sampling for ground truthing. Also complementary near surface direct push measurements will be helpful.

The derived empirical relationship linking volumetric water and clay content to Q could also be combined with a simple theoretical model to explain the observed decrease of the spectral central frequency GPR reflections as a function of water and clay content. The generally good agreement of observed and theoretical frequency shifts confirms the plausibility of Q values derived from the spectral ratios. This finding indicates that areal variations of Q may be determined in field measurements from the variation of the central frequency that can be identified, for example, with the instantaneous frequency (Taner et al. 1979). A similar approach was suggested by Liu et al. (1998) who showed that the attenuation of electromagnetic waves is proportional to the difference in centroid frequencies between initial and reflected wavelet. This approach was successfully applied to cross-hole data during a saline-tracer injection experiment to map the spatial extend of the tracer. Compared to the spectral ratio method this approach is more simple but it may suffer from the simplifying assumptions of the source spectra as well as from interference effects and random noise. The first application to field data using the instantaneous frequency showed that it might be possible to determine the order of magnitude of the clay content. Nevertheless this method is strongly influenced by the noisy appearance of the instantaneous frequency and the filter used to flatten it. The result will be also dependent on the time interval which is used to fit the linear function for the Q determination.

Clearly, these factors affect Q values determined by the spectral ratio method as well. In order to check the reliability of these Q values synthetic radargrams were computed that were compared to observed radargrams (Fig. 3.14). For the modelling the program matGPR by Tzanis (2010) was used that includes a wavefield extrapolation in the frequency-wavenumber-domain by Bitri and Grandjean (1998) to compute GPR wave propagation in 2D. Input parameters of the model are the thickness of the soil sample, antenna central frequency, quality factor, relative permittivity, magnetic permeability and electrical conductivity. For the central frequency the frequency of the reference wavelet (1440 MHz) was used. For Q, relative permittivity, magnetic permeability and electrical conductivity we assumed the values measured on the soil samples at each step of water content. A comparison between observed and modelled GPR reflections is shown for one exemplary sample with low clay content in Fig. 3.14. Observed and modelled data agree generally well in both traveltime and waveform. The agreement is best at low water contents (top of Fig. 3.14) and gets slightly worse for higher water contents (bottom of Fig. 3.14). The RMS difference between observed and synthetic radargrams ranges from 3-14 % only, which can be considered as a confirmation of the chosen way of field data analysis.

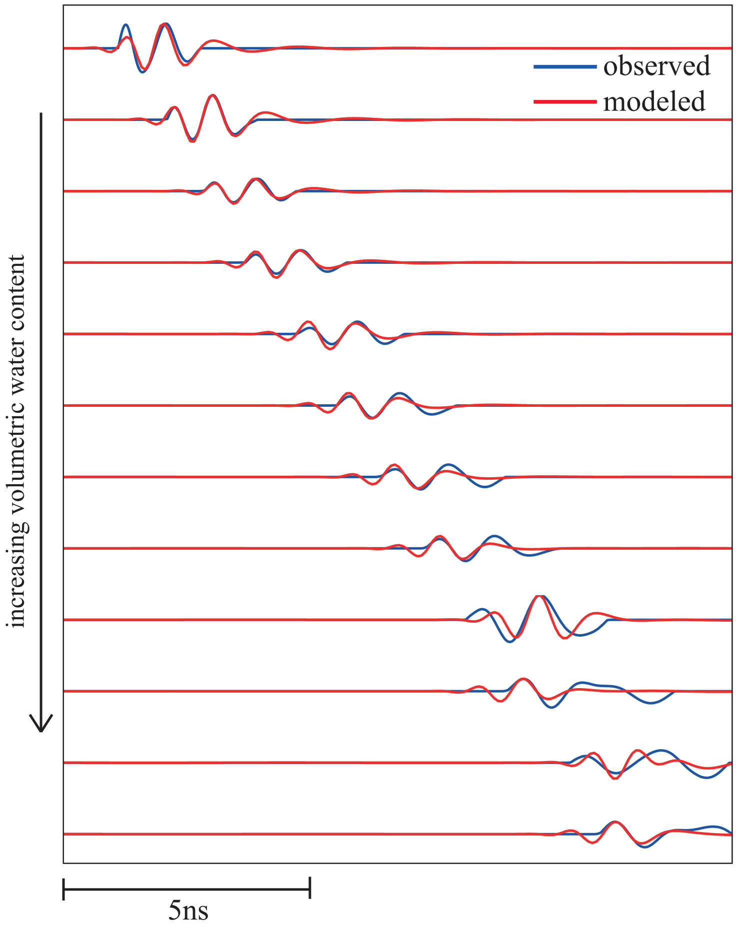

Fig. 3.14: Comparison of observed and modelled reflections for a low clay content sample at all water content steps. For each step the relative amplitude is used.

There are small differences between observed and modelled radargrams that are caused mainly by simplifying assumptions about the source wavelet and the antenna geometry and by neglecting scattering effects. The original source wavelet had to be approximated by a wavelet with a Gaussian spectrum (Bitri and Grandjean 1998). The model uses a zero-offset configuration whereas the real antenna has a small offset between transmitter and receiver. To compensate for this a small time shift was added to the modelled wavelet. Generally we have to consider that losses are caused not only by dielectric relaxation and electrical conductivity but also by scattering. Scattering is neglected in the modelling program. The high similarity of the modelled and observed waveforms shows, however, that coda effects caused by scattering play indeed a minor role in the investigated soils.

3.5 Conclusion

In order to determine the dependence of the absorption of GPR waves on the clay and water content in soils 23 soil samples with clay contents between 3 and 63% and water contents of 0 to 40% were investigated. For the large-scale samples we determined the electrical conductivity, the propagation velocity of the GPR waves and the absorption in terms of the quality factor Q. From these values the complex valued dielectric permittivity was determined in order to separate the absorption effects caused by electrical conductivity and dielectric relaxation.

The determination of Q values was based on the spectral ratio method, which showed that Q is approximately constant between 0.6 and 1.6 GHz. The obtained Q values are compatible with the observed decrease of the central frequency of reflected GPR waves and with corresponding synthetic waveform modelling.

A multivariate regression analysis showed that the Q factor can be described in terms of clay content c_c and water content θ by the following equation:

$$\frac{1}{Q} \approx \frac{\theta^{0.10} \cdot c_c^{\,0.16}}{28.2} \quad . \tag{3.15}$$

The denominator 28.2 on the right hand side can be interpreted as a reference maximum Q value applying to low water and clay contents. The equation fits the observed values with ±8.4 % accuracy. Q combines the absorption effects of electrical conductivity and dielectric relaxation that are influenced by both clay content and free water. The further analysis showed that the ratio of the imaginary to complex parts of the permittivity depends mainly on the clay content. The corresponding ε''-ε' relationship is linear where the slope is given by

$$\frac{d\varepsilon''}{d\varepsilon'} \approx 0.19 \cdot c_c^{\,0.15} \quad . \tag{3.16}$$

The empirical relations show that it may be possible to distinguish between bound and free water effects - that is between clay content and water saturation - in geophysical field measurements if the GPR absorption is considered in addition to GPR wave velocity and electrical conductivity. First applications to field data gave promising results at least to determine the order of magnitude of the clay content.

4. Inversion of EM38DD data measured in different heights

4.1 Introduction

Easy to use handheld electromagnetic (EM) induction sensors, such as the EM38DD (Geonics Ltd.), are frequently used for archaeological prospecting (e.g. von der Osten-Woldenburg 2005, Linford 2006) and soil science (e.g. Lesch et al. 2005, Kitchen et al. 2005, Saey et al. 2009). In archaeology the measured lateral changes in electrical conductivity are used to delineate objects in the ground and are mostly complemented by other geophysical methods. In soil science the measured values are used more and more quantitatively, e.g. Lesch et al. (2005) links the measured apparent conductivity values to soil salinity and soil texture by linear regression models, but does not differentiate between layers. Because the EM38DD measures an apparent conductivity as a cumulative effect over several layers down to a depth of approximately 1.5 m it is not possible to directly infer the electrical conductivities of the single layers. To receive information about different depth intervals several measurements with different specifications have to be conducted. Parameters that influence the depth of penetration in electromagnetic induction methods are (1) the coil spacing, i.e. larger coil spacing leads to greater penetration depth, (2) coil orientation, i.e. vertical coil axis orientation reaches larger depths, (3) frequency, i.e. low frequency signals reach greater depths (Spies and Frischknecht 1991) and (4) height above the ground, i.e. in larger height the signal is more sensitive to the surficial layers (Saey et al. 2009). Because the EM38DD has a fixed coil spacing and frequency and two coil orientations (vertical and horizontal) a single survey would result in two known parameters, i.e. the apparent electrical conductivities measured with different coil orientations. Assuming a 2-layer case there are three unknowns: the electrical conductivities of upper and lower layer and the depth of the interface. Thus this leads to an underdetermined system of equations. The only additional option for sounding and to increase the number of known parameters is the use of different measuring heights. This leads to an overdetermined system of equations.

This sort of depth sounding was conducted by e.g. Borchers et al. (1997), Hendrickx et al. (2002) and Gebbers et al. (2007). They all inverted the measured apparent electrical conductivity values using a linear model with respect to conductivity based on the low loss approximation. Their models comprised several layers of fixed thickness and the solution parameters were the conductivities of each layer. All inversions were conducted on single points and not on a field-scale.

The aim of this study is to investigate the inversion of EM38DD sounding data measured in two heights to yield two layer conductivities and the thickness of the first layer in a model that is variable in two dimensions. The two layers may correspond to topsoil and subsoil. The results are maps of electrical conductivity of two layers and a map of the depth of the interface between the layers. First different inversion approaches will be evaluated on the basis of a synthetic profile. The best approach will then be applied to two data examples from Rosslau (Germany) and Lany (Czech Republic) where EM38DD data in different heights were acquired on a larger scale (about 10 mx 70 m). The measurements can be realised relatively easy and time efficient in the field using a tractor that pulls the EM38DD mounted on a plastic sledge. A construction from plastic and wood on the sledge allows the EM38DD to be mounted also higher above the ground. The time effort is only twice that of a standard EMI survey, but yields more precise information about the soil (i.e. electrical conductivities for specific depth ranges and topsoil thickness).

4.2 Theory

4.2.1 Electromagnetic methods

Low induction number (LIN) approximation

In the electromagnetic induction method for near surface application a transmitter coil is used to produce an oscillating magnetic field. This primary field H_p generates eddy currents in the ground that in turn induce a secondary magnetic field (H_s). This magnetic field is superimposed with the primary field and both are measured with the receiver coil. The ratio of secondary to primary field is a function of frequency (f), coil spacing (s), magnetic permeability (μ) and electrical conductivity (σ) of the underlying halfspace (e.g. McNeill 1980).

In a homogeneous halfspace the skindepth is the depth where the amplitude of a plane wave is the initial amplitude (at the surface) divided by e (≈2.718). It is defined as

$$\delta = \frac{\sqrt{2}}{\sqrt{\omega\mu_0\sigma}} = \frac{\sqrt{2}}{\gamma} \tag{4.1}$$

where $\omega = 2\pi f$ is the angular frequency and μ_0 is the magnetic permeability of free space. The induction number B is defined as the ratio of the coil spacing s and the skindepth δ:

$$B = \frac{s}{\delta} \tag{4.2}$$

Inserting (4.1) into (4.2) yields

$$B = \frac{\gamma \cdot s}{\sqrt{2}} \,. \tag{4.3}$$

If $\gamma \cdot s \ll 1$, then the induction number B is very small and the ratio of secondary to primary magnetic field can be approximated by the following formula for the relation to the apparent electrical conductivity σ_a:

$$\sigma_a = \frac{4}{\omega\mu_0 s^2} \cdot \frac{H_s}{H_p} \,. \tag{4.4}$$

For $B \ll 1$, the coil spacing has to be much smaller than the skindepth, which in turn gives a constraint to the frequency:

$$\omega \ll \frac{2}{\mu_0\sigma s^2} \tag{4.5}$$

The EM38DD has a coil spacing of 1m and uses a fixed frequency of 14.6 kHz. This means that the conductivity of the homogeneous halfspace may not exceed 17 S/m (=17000 mS/m) for the low induction number (LIN) approximation to hold, which is never reached in our field examples.

Cumulative response functions

The EM38DD has different sensitivities in different depths. The sensitivity function is different for horizontal and vertical coil orientation and has its maximum at the surface and at a depth of 0.4 times the coil spacing for horizontal and vertical orientations, respectively.

The cumulative response functions under the LIN approximation for horizontal and vertical coil orientations are defined as (McNeill 1980):

$$R_H(z) = (4z^2 + 1)^{1/2} - 2z \tag{4.6}$$

and

$$R_V(z) = \frac{1}{(4z^2 + 1)^{1/2}} \quad . \tag{4.7}$$

In general, z is the depth divided by the coil spacing, but because the coil spacing is 1m for the EM38DD this is neglected in the following. These functions give the relative contribution to the measured apparent electrical conductivity from all material below a depth z.

Fig. 4.1 shows the cumulative responses for a homogeneous halfspace as a function of depth. The measured apparent conductivity of the vertical coil orientation will be more influenced by the lower layers than that of the horizontal coil orientation.

Using the EM38DD both the frequency and the coil spacing are fixed. This means that the only additional parameter that can be varied for depth sounding is the height above surface. If the EM is lifted at height z_0 above ground the cumulative response curves are also lifted upwards and thus are more sensitive to upper layers of the halfspace. The air layer between instrument and ground is assumed to have zero electrical conductivity (Fig. 4.2).

Using the cumulative responses the apparent electrical conductivity of a two-layered halfspace can be calculated (Spies and Frischknecht 1991):

$$\begin{aligned} \sigma_{a,V} &= \sigma_0 \cdot [1 - R_V(z_0)] + \sigma_1 \cdot [R_V(z_0) - R_V(z_0+z_1)] + \sigma_2 \cdot R_V(z_0+z_1) \\ &= \sigma_1 \cdot [R_V(z_0) - R_V(z_0+z_1)] + \sigma_2 \cdot R_V(z_0+z_1) \end{aligned} \tag{4.8}$$

$$\begin{aligned} \sigma_{a,H} &= \sigma_0 \cdot [1 - R_H(z_0)] + \sigma_1 \cdot [R_H(z_0) - R_H(z_0+z_1)] + \sigma_2 \cdot R_H(z_0+z_1) \\ &= \sigma_1 \cdot [R_H(z_0) - R_H(z_0+z_1)] + \sigma_2 \cdot R_H(z_0+z_1) \; . \end{aligned} \tag{4.9}$$

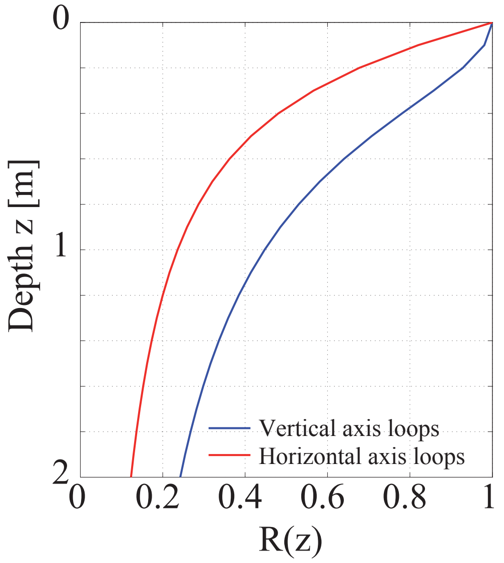

Fig. 4.1: Cumulative response R as a function of depth z for vertical and horizontal axis loops over a homogeneous halfspace.

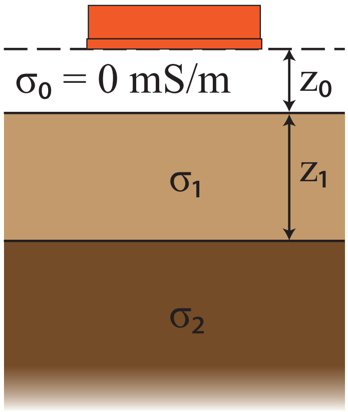

Fig. 4.2: Sketch of the EM38DD in a height z_0 above ground. σ_1 and σ_2 are the electrical conductivities of first and second layer, respectively, and z_1 is the thickness of the first layer.

Comparison to model without LIN approximation

The above-mentioned equations are only valid in the LIN approximation. A formulation for the exact analytic solution if given by Koefoed et al. (1972) and implemented in the modeling program FreqEM (Loke 2006). Unfortunately this program can only invert one point at a time and is thus not suitable for the inversion of profiles or even large areas. Additionally the computation is faster for the LIN model, which might be of interest for large areas.

To compare both models, the apparent conductivities for horizontal and vertical mode are calculated using both formulations for different combinations of σ_1, σ_2, z_1 and two values for z_0.

The conductivities range between 0 and 100 mS/m, z_1 between 0.3 m and 1.5 m and z_0 is 12.5 cm or 55 cm. The error of the approximation is shown for z_1=0.9 m in Fig. 4.3. The error is largest (~20%) for the conductivity of the second layer approaching 100 mS/m. In general, the errors are larger for a larger height above the ground and for the vertical coil orientation. The red box indicates the range that is relevant for the following inversion examples. Thus the error using the LIN approximation equations compared to the exact solution is negligible here (0 - 10 %), which justifies the choice of the LIN model for the inversion.

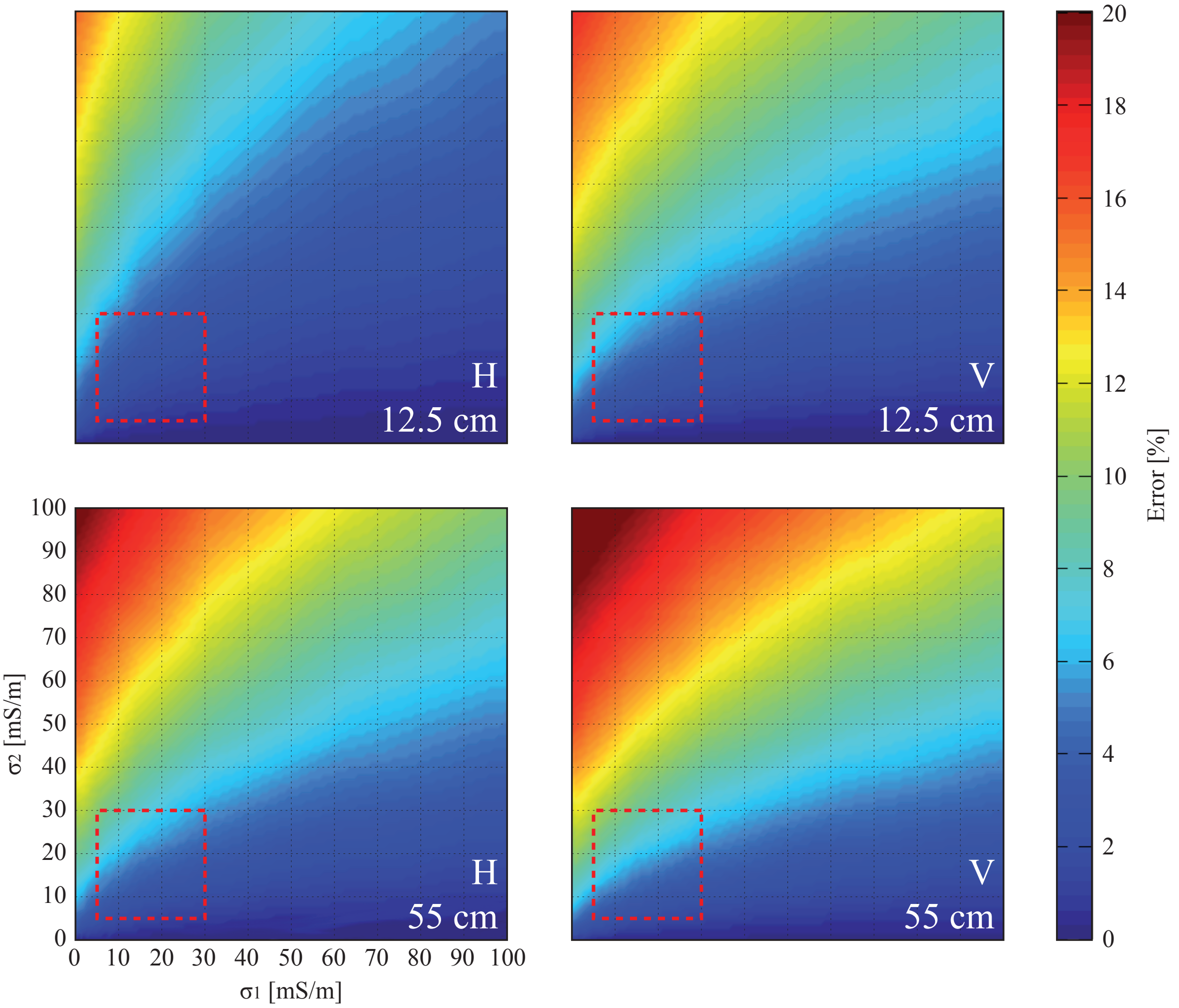

Fig. 4.3: Error between LIN approximation (McNeill 1980) and exact (Koefoed et al. 1972) formulation for z_1=0.9 m and all four measurements (horizontal and vertical coil orientations in two heights). The red box indicates the conductivity range that is relevant for the following inversion examples.

4.2.2 Inversion theory

Linearisation and objective function

Equations (4.8) and (4.9) shall be used to receive the conductivity distribution in the subsurface from measured values. Although the equations are linear with respect to the conductivities, they are non-linear with respect to z (see eq. (4.6) and (4.7)). To apply a linear inversion approach they have to be linearised using Taylor series expansion. The resulting linearised equations are (the index "a" as a symbol for apparent conductivity has been omited in the following):

$$\sigma_V^{obs} - \sigma_V^{Start} = \frac{\delta\sigma_V}{\delta\sigma_1} \cdot \Delta\sigma_1 + \frac{\delta\sigma_V}{\delta\sigma_2} \cdot \Delta\sigma_2 + \frac{\delta\sigma_V}{\delta z_1} \cdot \Delta z_1 \tag{4.10}$$

$$\sigma_H^{obs} - \sigma_H^{Start} = \frac{\delta\sigma_H}{\delta\sigma_1} \cdot \Delta\sigma_1 + \frac{\delta\sigma_H}{\delta\sigma_2} \cdot \Delta\sigma_2 + \frac{\delta\sigma_H}{\delta z_1} \cdot \Delta z_1 \tag{4.11}$$

with the partial derivatives

$$\frac{\delta\sigma_V}{\delta\sigma_1} = \frac{1}{(4z_0^2 + 1)^{1/2}} - \frac{1}{(4\cdot(z_0 + z_1^{Start})^2 + 1)^{1/2}}$$

$$\frac{\delta\sigma_V}{\delta\sigma_2} = \frac{1}{(4\cdot(z_0 + z_1^{Start})^2 + 1)^{1/2}}$$

$$\frac{\delta\sigma_V}{\delta z_1} = \frac{4\cdot(z_0 + z_1^{Start})}{(4\cdot(z_0 + z_1^{Start})^2 + 1)^{3/2}} \cdot (\sigma_1^{Start} - \sigma_2^{Start})$$

$$\frac{\delta\sigma_H}{\delta\sigma_1} = (4z_0^2 + 1)^{1/2} - 2z_0 - (4\cdot(z_0 + z_1^{Start})^2 + 1)^{1/2} + 2\cdot(z_0 + z_1^{Start})$$

$$\frac{\delta\sigma_H}{\delta\sigma_2} = (4\cdot(z_0 + z_1^{Start})^2 + 1)^{1/2} - 2\cdot(z_0 + z_1^{Start})$$

$$\frac{\delta\sigma_H}{\delta z_1} = \left[\frac{4\cdot(z_0 + z_1^{Start})}{(4\cdot(z_0 + z_1^{Start})^2 + 1)^{1/2}} - 2 \right] \cdot (\sigma_2^{Start} - \sigma_1^{Start}).$$

The linearisation leads to initial values (labeled by ^{Start}), around which the expansion has been carried out. They have to be guessed before the first iteration (see section 4.3.3about starting values) and are updated in each iteration using the result of the previous iteration. Parameter σ_v^{Start} and σ_H^{Start} result from equations (4.8) and (4.9) calculated with starting values for the conductivities of upper and lower layer and depth of the interface.

The resulting linearised equations can be written for two heights above the ground and two orientations (H1, V1, H2, V2) and thus can be summarised in matrix equation as

$$\mathbf{y}^{obs} - \mathbf{y}_0^{mod} = \frac{\delta \mathbf{y}(\mathbf{m}_0)}{\delta \mathbf{m}} \cdot \Delta \mathbf{m} \quad , \tag{4.12}$$

where $\Delta\mathbf{m} = \mathbf{m} - \mathbf{m}_0$, $\mathbf{m} = (\sigma_1, \sigma_2, z_1)$, $\mathbf{m}_0 = (\sigma_1^{Start}, \sigma_2^{Start}, z_1^{Start})$, $\mathbf{y}^{obs} = (\sigma_{H1}, \sigma_{V1}, \sigma_{H2}, \sigma_{V2})$ and $\mathbf{y_0}^{mod} = (\sigma_{H1}^{Start}, \sigma_{V1}^{Start}, \sigma_{H2}^{Start}, \sigma_{V2}^{Start})$. $\delta\mathbf{y}(\mathbf{m}_0)/\delta\mathbf{m} = A$ is the Jacobi matrix comprising the partial derivatives (4x3-matrix).
The objective function that shall be minimised is then

$$S_2 = \sum_i |y_i^{obs} - y_i^{mod}|^2 \quad \rightarrow \text{Minimum} \; . \tag{4.13}$$

The usual way to solve this equation is by the Gauss-Newton method applicable to normal and overdetermined systems of linear equations (Menke 1989). The solution of equation (4.13) is then given by

$$\Delta\mathbf{m} = (A^T \cdot A)^{-1} \cdot A^T \cdot (\mathbf{y}^{obs} - \mathbf{y}_0^{mod}). \tag{4.14}$$

Several iterations are carried out, in which $\mathbf{m}_0$ is updated in each iteration:

$$\mathbf{m}_0^{n+1} = \mathbf{m}_0^{n} + \Delta\mathbf{m} \; . \tag{4.15}$$

The inversion is stopped if the change in $\| \mathbf{y}^{obs} - \mathbf{y}_0^{mod} \|_2$ between iterations is smaller than 0.1.

Singular value decomposition
Another technique to solve equation (4.14) is the singular value decompositon (SVD) that can also solve ill-conditioned problems (Press et al. 2002).
SVD uses the fact that a m x n matrix can be split into a m x n orthogonal matrix U multiplied by a n x n diagonal matrix L and the transpose of an orthogonal n x n matrix V (Press et al. 2002):

$$A = U \cdot L \cdot V^T. \tag{4.16}$$

The columns of U are the eigenvectors of AA^T, the columns of V the eigenvectors of A^TA and the diagonal elements of L are the corresponding singular values in descending order. To solve the set of linear equations the generalised inverse can be calculated (Menke 1989), which is

$$H = V \cdot L^{-1} \cdot U^T. \tag{4.17}$$

The solution vector x is then

$$\Delta\mathbf{m} = H \cdot (\mathbf{y}^{obs} - \mathbf{y}_0^{mod}). \tag{4.18}$$

One advantage of the SVD is the characterisation of the matrix A in terms of singularity. If the condition number (ratio of largest to smallest singular value) of A is infinite, matrix A is called singular. If the condition number is just very large, matrix A is called ill-conditioned (Press et al. 2002). The condition number is used as a criterion in section 4.3.4.

Inclusion of neighbouring points

Using only one measuring height results in an underdetermined system with two equations and three unknowns. Using two measuring heights instead gives an overdetermined system with four equations. Inclusion of neighbouring points can stabilise the system further. For this purpose it is assumed that a number of n (odd) neighbouring points represents the same underground segment as the inversion point. This results in a larger number of equations that constrain the subsurface properties locally.

Inclusion of smoothness constraints

Instead of assuming a locally constant model, it is possible to define a constraint that limits the variation between neighbouring points. This is reasonable, because it is unlikely that there are sharp steps between neighbouring points neither in electrical conductivity nor in the depth of the interface.

These smoothness constraints are included in the inversion procedure by three additional equations, for σ_1, σ_2 and z each. The number of neighbouring points for these constraints is m (odd). For m=3 the smoothness constraints read

$$0 = -0.5\cdot\sigma_1^{i-1} + \sigma_1^{i} - 0.5\cdot\sigma_1^{i+1} \quad , \qquad (4.19)$$

$$0 = -0.5\cdot\sigma_2^{i-1} + \sigma_2^{i} - 0.5\cdot\sigma_2^{i+1} \quad , \qquad (4.20)$$

$$0 = -0.5\cdot z^{i-1} + z^{i} - 0.5\cdot z^{i+1} \quad , \qquad (4.21)$$

where i is the index of the i-th inversion point along a profile.

The multiplying factors (-0.5, 1, -0.5 in this example) have to sum up to 0. For larger m there are also more multiplying factors with the immediate neighbors having the largest influence. The number of factors that have to be determined is (m-1)/2.

Equations (4.19), (4.20) and (4.21) mean that also the underground model (i.e. σ_1^{i-1}, σ_1^{i+1}, σ_2^{i-1}, σ_2^{i+1}, z^{i-1} and z^{i+1}) of the neighbouring points has to be part of the solution vector x and thus are updated every iteration. But only the conductivities and depth of the middle point are taken as the result of the i-th inversion point.

Regularisation of the inversion through a-priori-information

Further stabilisation and improvement of the inversion process can be achieved by the inclusion of weighted a-priori information about the underground model, which is also known as Tikhonov regularisation (Hansen, 2001). This information can be, e.g., the depth from GPR measurements or electrical conductivities and interface depth from Schlumberger soundings or other geoelectrical methods. But care has to be taken regarding the correctness of the information, because they might be influenced by errors like incorrect time-depth conversion in GPR or geoelectric inversion errors. The influence of the a-priori information on the inversion results can be regularised using a weighting parameter w. The objective function is extended from equation (4.13) to (Hansen, 2001)

$$S_2 = \sum_i |y_i^{obs} - y_i^{mod}|^2 + \sum_j w \cdot |m_j - m_j^{ap}|^2 \rightarrow \text{Minimum} . \tag{4.22}$$

This means that additional to the minimisation of the difference between y^{obs} and y^{mod} the difference between the model and the a-priori information shall be minimised. The influence of this depends on the size of w, being larger for larger weight.
The solution can be derived using (Hansen, 2001)

$$\Delta\mathbf{m} = (A^T \cdot A + W)^{-1} \cdot (A^T \cdot (\mathbf{y}^{obs} - \mathbf{y}_0^{mod}) + W \cdot \Delta\mathbf{m}^{ap}) \tag{4.23}$$

with $W = w \cdot I$, where I is a 3x3 identity matrix, $\Delta\mathbf{m}^{ap} = \mathbf{m}^{ap} - \mathbf{m}_0$ and $\mathbf{m}^{ap} = (\sigma_1^{ap}, \sigma_2^{ap}, z_1^{ap})$ the vector containing the a priori information about conductivities and depth.
For choosing the „best“ weight w the L-curve criterion can be used, which is a plot of the solution norm $||x||$ versus residual norm $||Ax - y||$ (Hansen, 2001). Then the corner-point of the L-curve is considered as the best weight. This approach is used in section 4.3.5.

4.3 Inversion of synthetic data

4.3.1 Model

To test the above defined inversion approaches a synthetic underground model is invented with relatively strong variations in both conductivities and depth of the interface. The simulated measurements of apparent conductivity in vertical and horizontal mode are calculated for two different heights using equations (4.8) and (4.9) every 0.1m along the profile (Fig. 4.4). The heights were chosen according to field measurements to be 0.125 m and 0.55 m, due to the construction of the measuring sledge. Additional offsets have to be added to these heights, which are 9 cm for vertical mode and 1 cm for horizontal mode to account for the coil positions inside the EM38DD body.

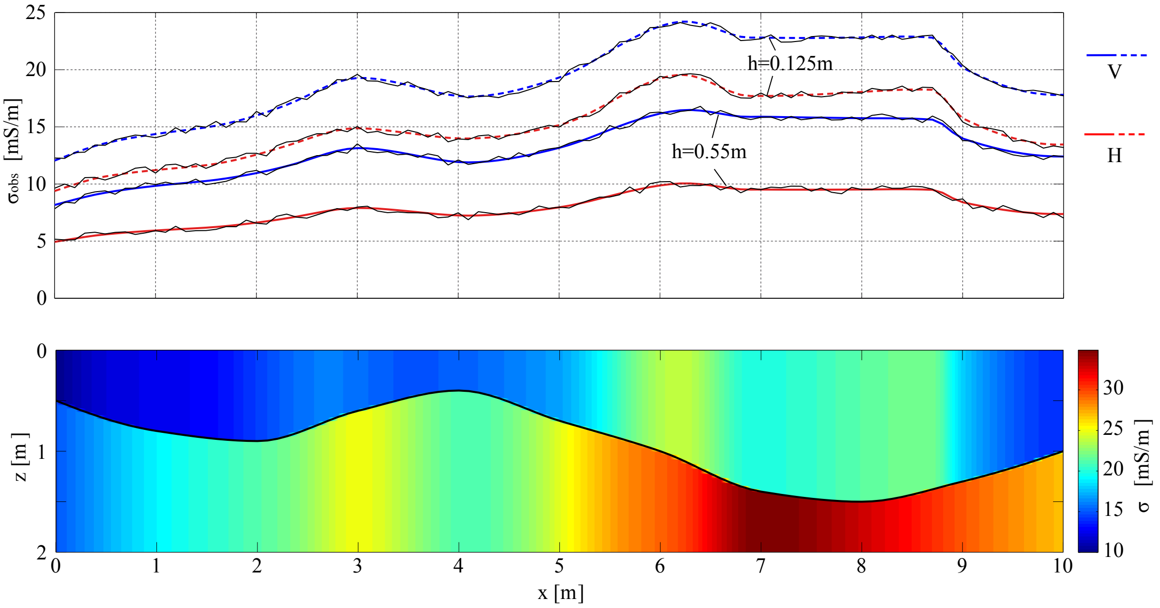

Fig. 4.4: Synthetic data in vertical and horizontal mode in different heights (blue and red curves) and with the addition of 2 % noise (black curves) (top) and underground model (bottom).

4.3.2 Simple inversions with one and two observation heights and neighbouring points

As a first step I inverted the synthetic data from one height (0.125 m) without and with 2 % of noise added to the observed data using no additional constraints. In the noise-free case the electrical conductivity of the upper layer is reconstructed well, whereas the conductivity of the lower layer and the depth of the interface are badly resolved (Fig. 4.5 b). The addition of noise leads to large jumps in the modelled parameters (Fig. 4.5 c). The noise-free case with 2 heights leads to a very good reconstruction of the model (Fig. 4.5 d), whereas only 2 % of noise causes the model parameters to be smaller than zero, which is not valid, or too large (white spaces) (Fig. 4.5 e). At some points the inversion did not converge and was automatically stopped after 1000 iterations.

The first constraining action is the inclusion of neighbouring points. The results for 7 neighbors for noise-free and noisy case are shown in Fig. 4.5 f and g. Again the noise-free case reconstructs the model good. The inversion with 2 % noise shows better results than the inversion without neighbouring points. For 21 neighbouring points and 2 % noise the inversion result (Fig. 4.5 h) is better than for 7 neighbours, but still not satisfactory. The resulting RMS errors (Root mean square) between original model and inverted parameters confirm these results (Fig. 4.6). The RMS errors for the noisy dataset with and without neighbouring points are similar although the images (Fig. 4.5 e and g) are not. This results from the calculation of the RMS error, which does not include missing points (white spaces in the images).

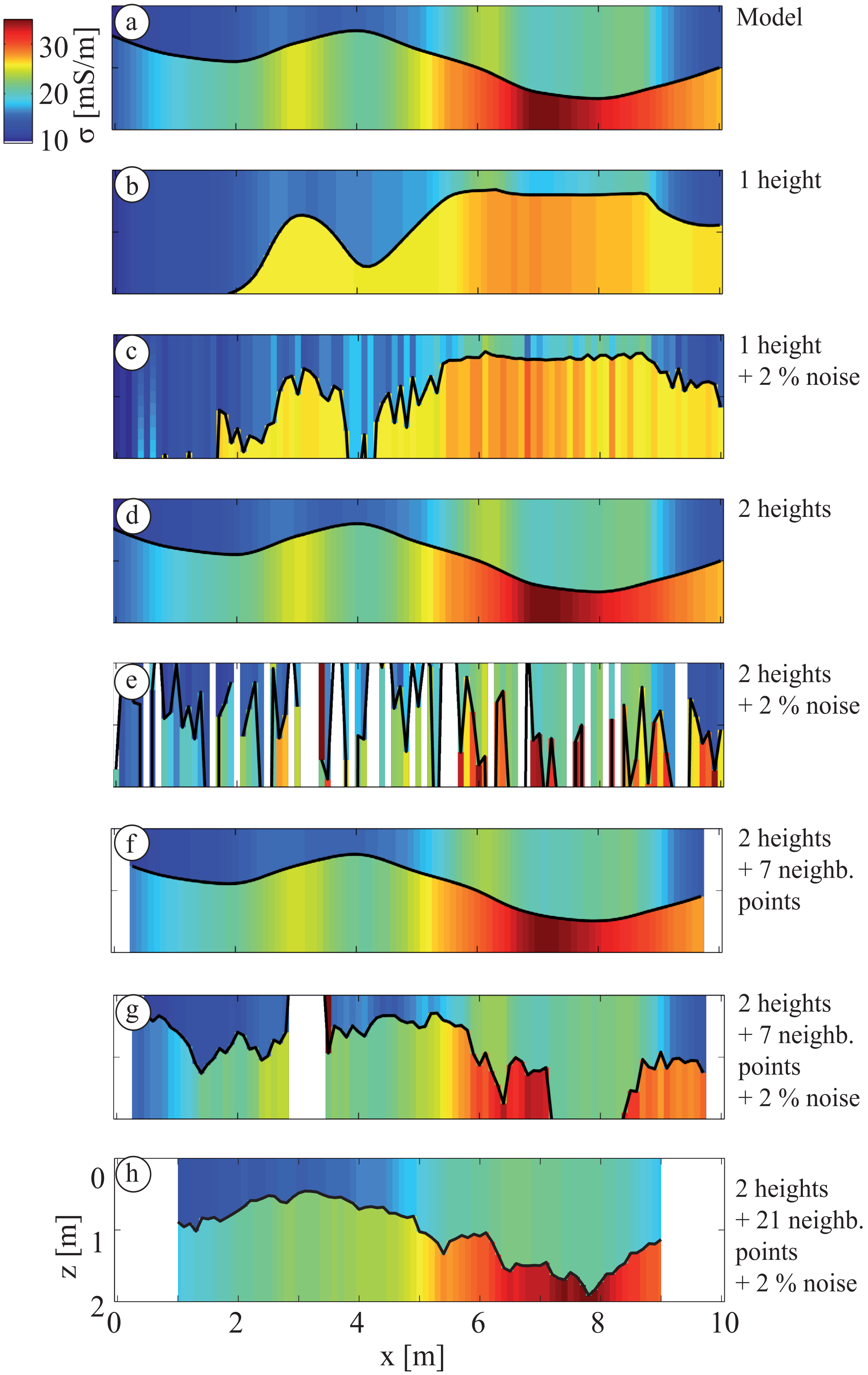

Fig. 4.5: Model (a) and different inversion approaches using 1 or 2 heights, with and without 2 % noise and neighbouring points.

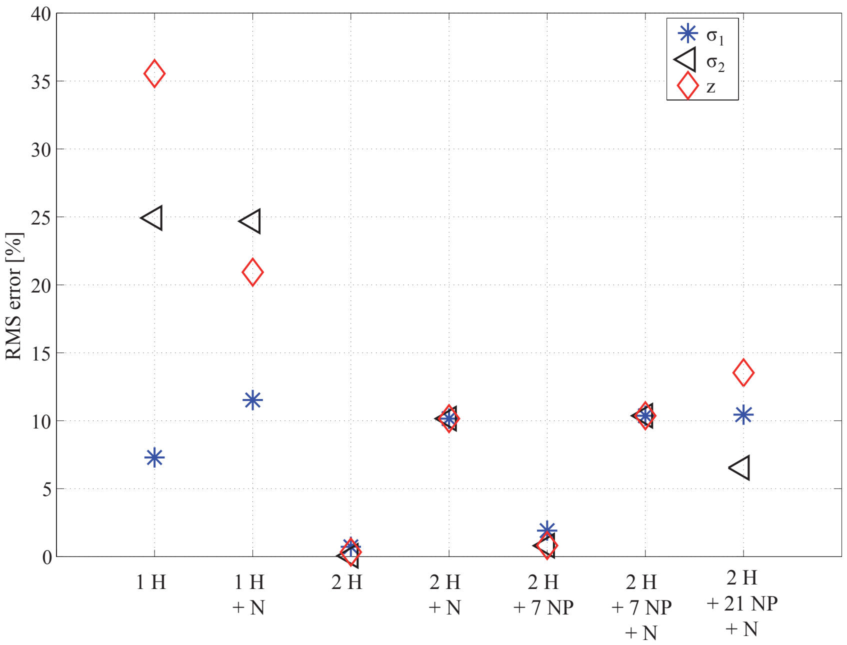

Fig. 4.6: RMS errors between original model and inverted conductivities and depth of interface for the six approaches presented in Fig. 4.5. (Abbreviations: H:height, N: 2% noise, NP: neighbouring points)

4.3.3 Influence of starting values

All these inversions have been carried out with the mean model parameters as starting values. In reality this is not possible, because they are unknown. For practice it is preferable to choose the starting values automatically for each inversion point depending on the measured apparent conductivities. To test this the inversion has been carried out using observations from two heights with 2 % noise and with the inclusion of 7 neighbouring points. The starting values have been varied in following ranges:

$\sigma_1^{Start} \in [\sigma_{H1} - 10 ; \sigma_{H1} + 10]$,
$\sigma_2^{Start} \in [\sigma_{V1} - 10 ; \sigma_{V1} + 10]$,
$z^{Start} \in [(\sigma_{H1}/\sigma_{V1}) - 0.8 ; (\sigma_{H1}/\sigma_{V1}) + 0.8]$,

with the restriction that none of the starting values may be smaller than zero. The resulting misfit at the end of the inversion is plotted for an exemplary point (x = 4 m) in Fig. 4.7 for different combinations of additive terms (-10 to 10 for σ_1 and σ_2, -0.8 to 0.8 for z). The additive terms resulting in the best starting values should lie in the global minimum of the misfit function. After examination of the misfit functions for several inversion points the best starting parameters were chosen to be $\sigma_1^{Start} = \sigma_{H1}^{obs}$, $\sigma_2^{Start} = \sigma_{V1}^{obs} + 4$ and $z^{Start} = \sigma_{H1}^{obs} / \sigma_{V1}^{obs}$. Thus all following inversions are calculated using these starting values.

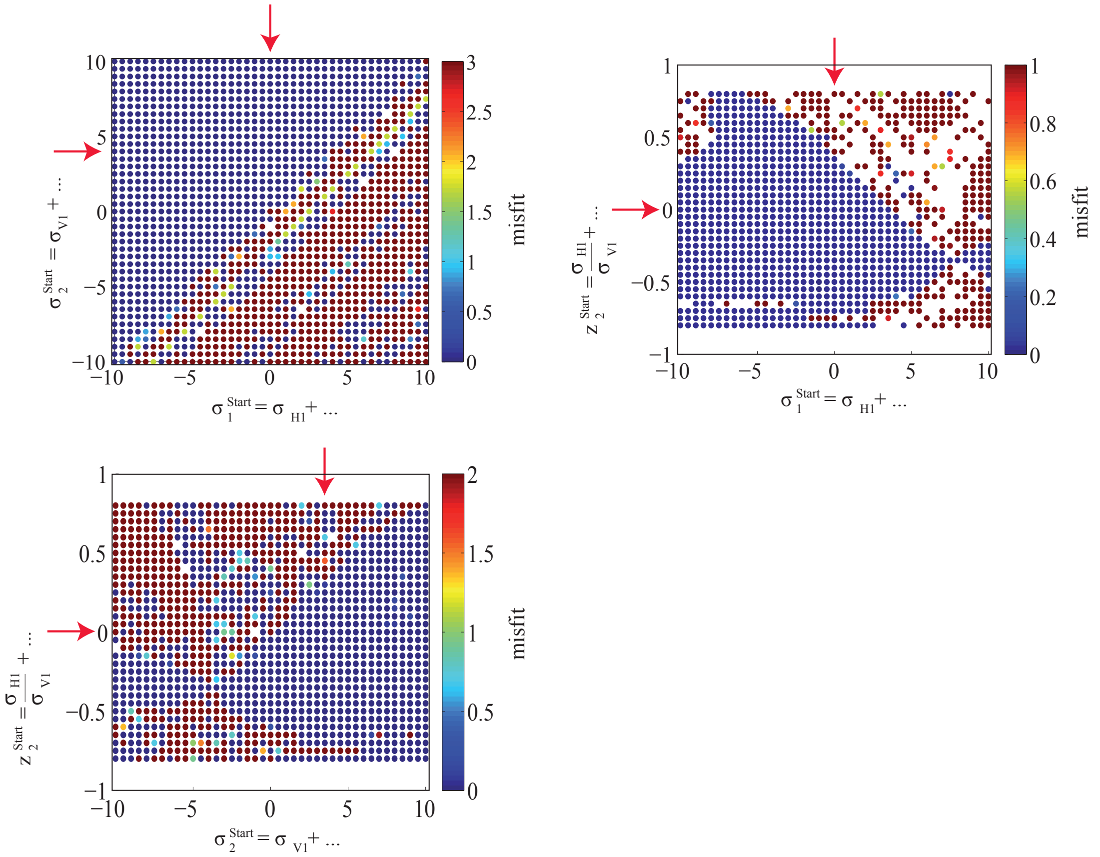

Fig. 4.7: Misfit as a function of possible starting values for x = 4 m. Red arrows indicate the chosen starting values.

4.3.4 Inversion with smoothness constraints

The next approach is the inclusion of smoothness constraints over m neighbouring points. For m=1 the inversion reduces to the case with two heights and no neighbors. Using the above mentioned starting values the inversion result for m=1 is worse than with the starting values taken before (Fig. 4.8 b in comparison to Fig. 4.5 d). The result is drastically improved by using m=3 which is shown in Fig. 4.8 c. There is only a small amount of data points around x = 9 m where there are small-scale variations in depth of the interface. For m>3 these small-scale variations increase and thus the result gets worse. For increasing m the condition number increases and leads to this instabile inversion. For the data inversion with 2 % noise the result for m=1 does not change too much compared to the noise-free case, whereas for m=3 there are a lot of missing points and large jumps in all parameters between neighbouring points (Fig. 4.9). The reason for this is investigated using SVD. Analysing the eigenvalues in the matrix L leads to a condition number of around 70, which is about 15 times that for m=1. This means that the matrix is ill-conditioned. Thus the inversion approach until now will be still not successfully applicable to noisy field data.

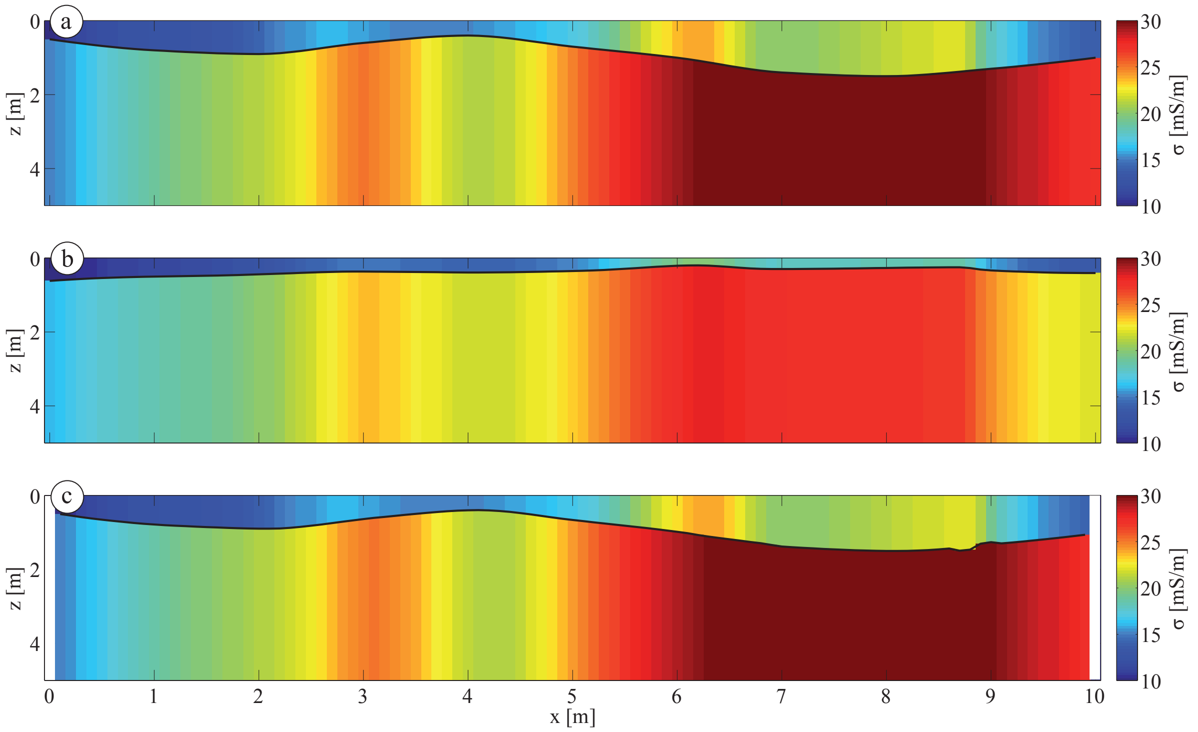

Fig. 4.8: Inversion with smoothness constraints for m=1 (b) and m=3 (c) points. a is the original underground model.

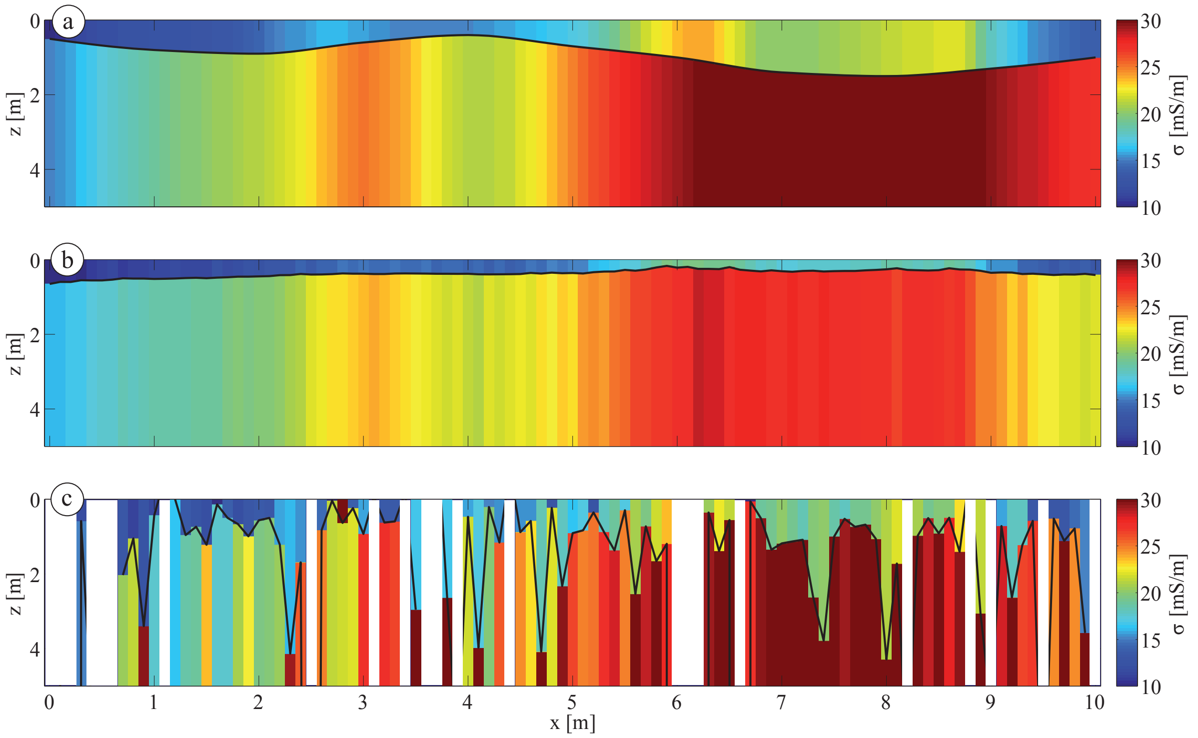

Fig. 4.9: Inversion with smoothness constraints and 2 % noise for m=1 (b) and m=3 (c) points.

4.3.5 Inversion with regularisation using a priori information

The next approach is the Tikhonov regularisation with the weighted inclusion of a priori information. As a priori information either the conductivities of upper and lower layer or the depth of the interface can be used. In the Matlab-script for this approach there needs to be an a priori information for every measurement point. If this information is not available, the starting values are used instead, because they have been proven to lead the inversion in the direction of the global minimum. In practice the a priori information can be gained from GPR measurements (providing depth of the interface only), geoelectric resistivity profiles or Schlumberger soundings (providing both conductivities and depth of the interface). Nevertheless the latter requires also an inversion, which is subject to ambiguity and might lead to doubtful results.

In the following example I assume that the conductivities and depths of the interface are known every 2 m along the profile, e.g. from Schlumberger soundings. For all measuring points in between the values have been interpolated linearly. The a priori information about depth of the interface every 2 m are marked by black dots in Fig. 4.11 b-d. The inversion has been carried out for 50 weights between 1e-10 to 1e5 using the L-curve as a criterion for the best value. In general the L-curve is expected to start at a relatively small residual norm and large solution norm for small weights and then move to larger residual norms and smaller solution norms for increasing weights. In the first example for m=1 the solution norm is increasing for increasing weights until it reaches a peak and then decays rapidly as expected (Fig. 4.10). To illustrate the different steps of this process three points have been marked with red stars and the inversion results for these regularisation parameters have been plotted in Fig. 4.11 b-d.

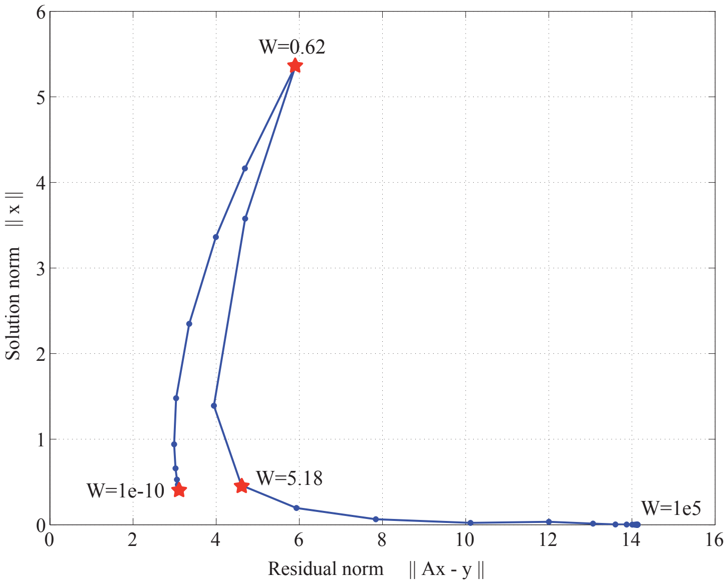

Fig. 4.10: L-curve for the inversion with a-priori-information taken from the original model every 2 m and interpolated in between and m=1. Significant points are marked with red stars and labelled with their weight.

The inversion with the smallest weight has the smallest solution and residual norms, thus it should be the best weight depending only on the L-curve criterion.

But having a look at the result (Fig. 4.11 b) shows that neither the depth of the interface nor the conductivities have been well resolved. The result also reveals that the solution is relatively far from the a priori information (compare the interface and black dots). For larger weights the solution approaches the a priori information, although the solution norm reaches a maximum for w=0.62. This must be due to differences in the conductivities because the depth of interface is already close to the a priori information (Fig. 4.11 c). After this weight the L-curve behaves as expected and the solution norm decreases together with an increasing residual norm. Considering only this typical part of the L-curve, the best weight is w=5.18 whose result is shown in Fig. 4.11 d.

Comparing the three mentioned results, the best weight is the one at the corner point of the typical part of the curve with w=5.18.

To investigate the data for m=1 without available Schlumberger soundings the starting values gained from the measured conductivities are used as a priori information. The resulting L-curve is typically shaped and the corner point is reached for w=0.62 (Fig. 4.12). The result is shown in Fig. 4.13 b, which is far from the original model.

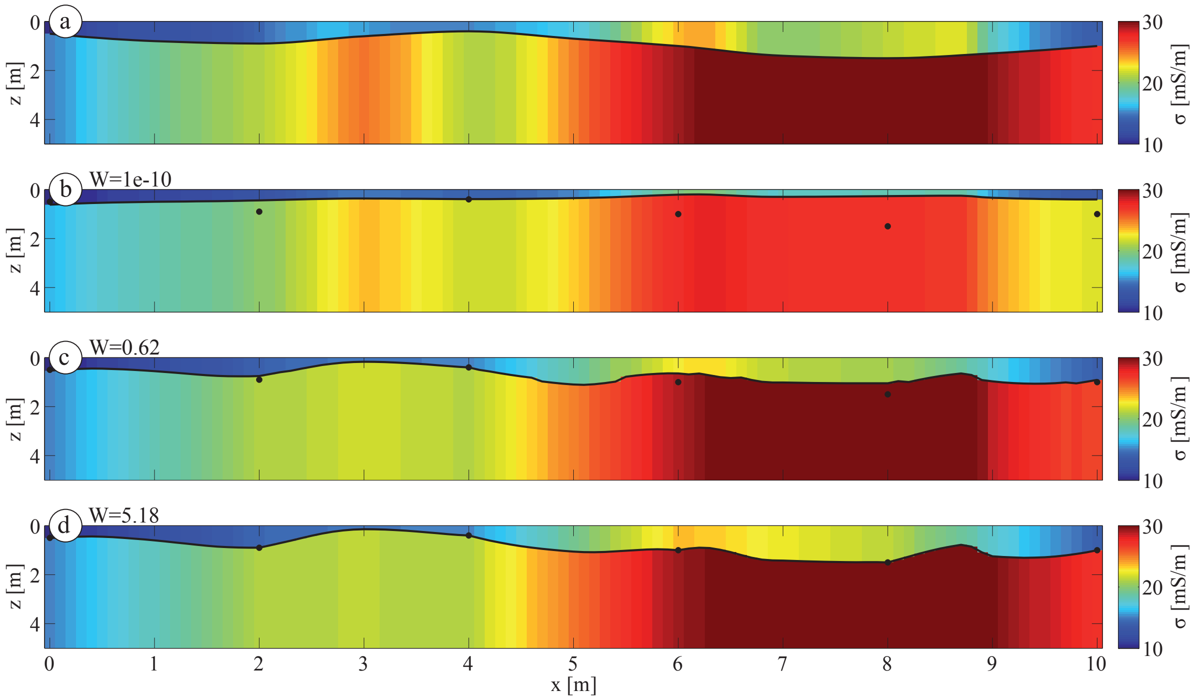

Fig. 4.11: Original underground model (a) and inversion results (m=1) for weights of 1e-10 (b), 0.62 (c) and 5.18 (d). For the corresponding L-curve see Fig. 4.10. The black dots indicate the a priori information about the depth of the interface every 2 m.

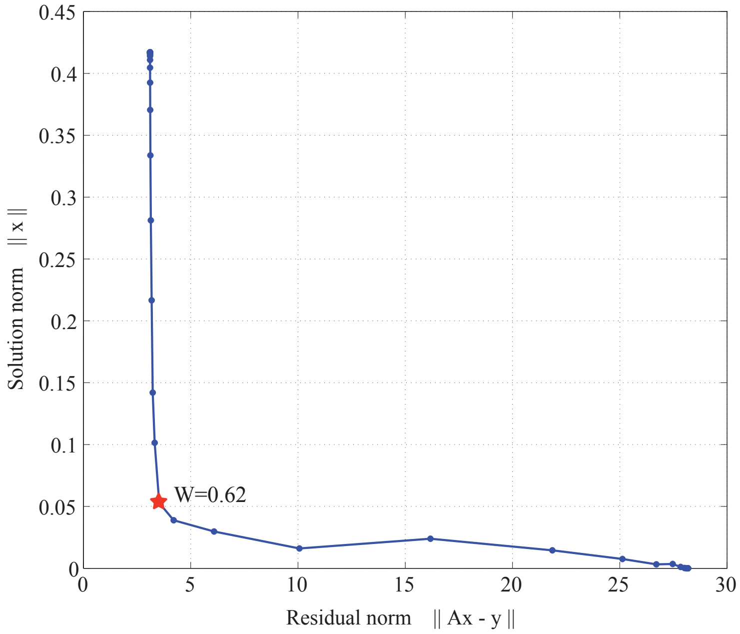

Fig. 4.12: L-curve for the inversion with starting values as a-priori-information and m=1. The best weight is marked with a red star and labelled with its weight.

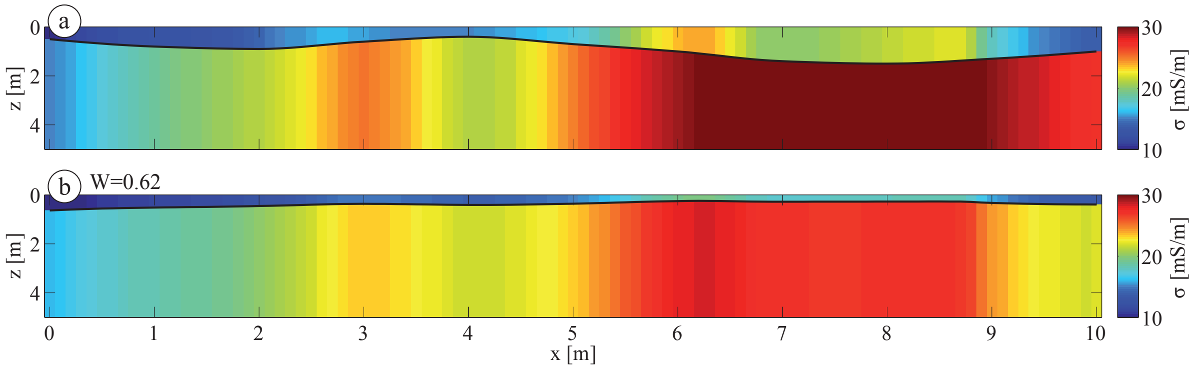

Fig. 4.13: Original underground model (a) and inversion result for best weight (w=0.62) based on L-curve criterion for m=1 (b).

A chance to improve the result is to increase the number of points for smoothness constraints to m=3. The resulting L-curve shows the same atypical behaviour as Fig. 4.10, thus I investigate the results at a very small weight and for the corner point of the typical part of the curve (red stars). The model for the very small weight matches the original perfectly (Fig. 4.15 b), whereas the typical L-curve criterion leads to a worse result (Fig. 4.15 c). The explanation for this contrary behaviour to the first case for m=1 is the different choice of a priori information. For m=3 I chose the starting values to be the apriori information, which are mainly reproduced by Fig. 4.15 c. This means that the a priori information were wrong and thus a very small weight gives a better result. This is of course difficult to identify for real data, because in this case the original model is not known and thus a direct control of the performance of the inversion is not possible.

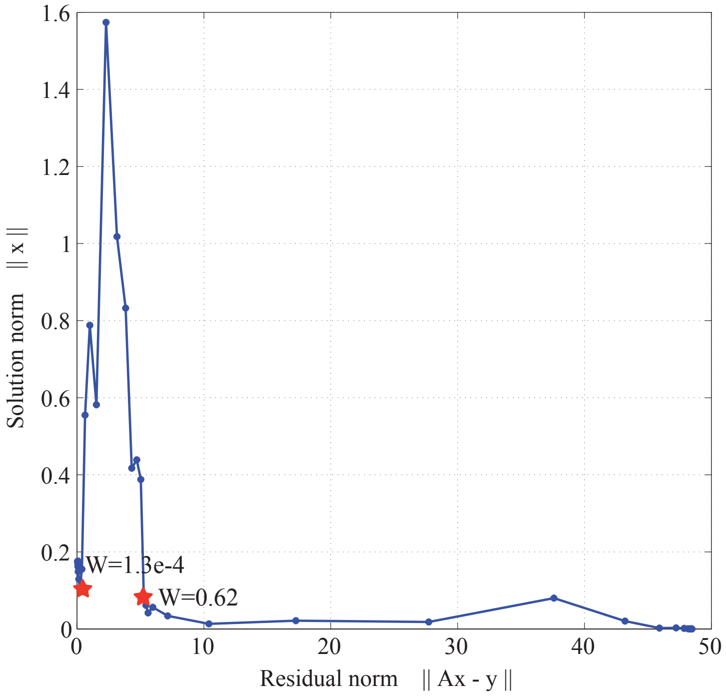

Fig. 4.14: L-curve for the inversion with starting values as a-priori-information and m=3. Significant points are marked with red stars and labelled with their weight.

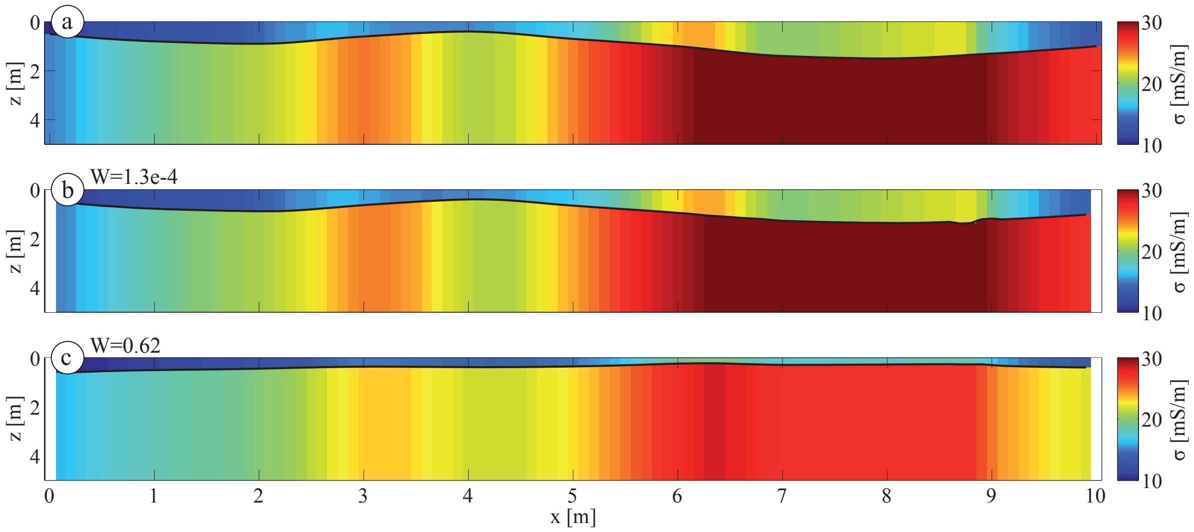

Fig. 4.15: Original underground model (a) and inversion results for weights w=1.3e-4 (b) and w=0.62 (c) and m=3.

Taking a step towards real data and adding 2 % noise to the observed data leads to typical shaped L-curves for m=1 and m=3 (Fig. 4.16). The results for m=1 and m=3 calculated with the weights representing the corner points of the curves are almost identical (Fig. 4.17) and represent mainly the starting values. Using m>3 again leads to larger condition numbers that are indicators for an ill-conditioned system.

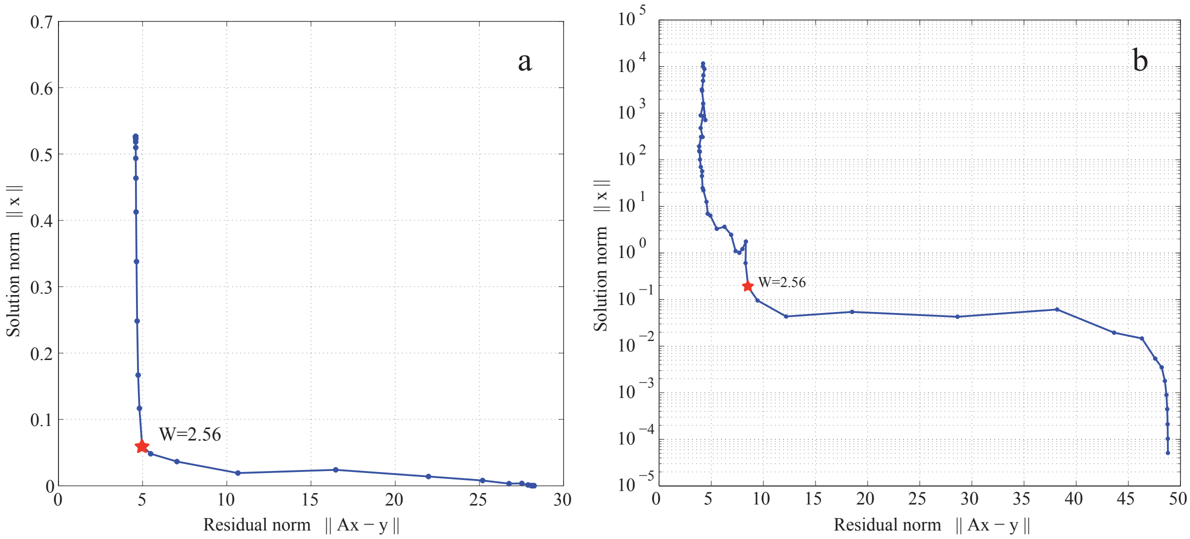

Fig. 4.16: L-curves for the inversion with 2 % noise, starting values as a-priori-information and m=1 (a) and m=3 (b). The best weight is marked with a red star and labelled with its weight.

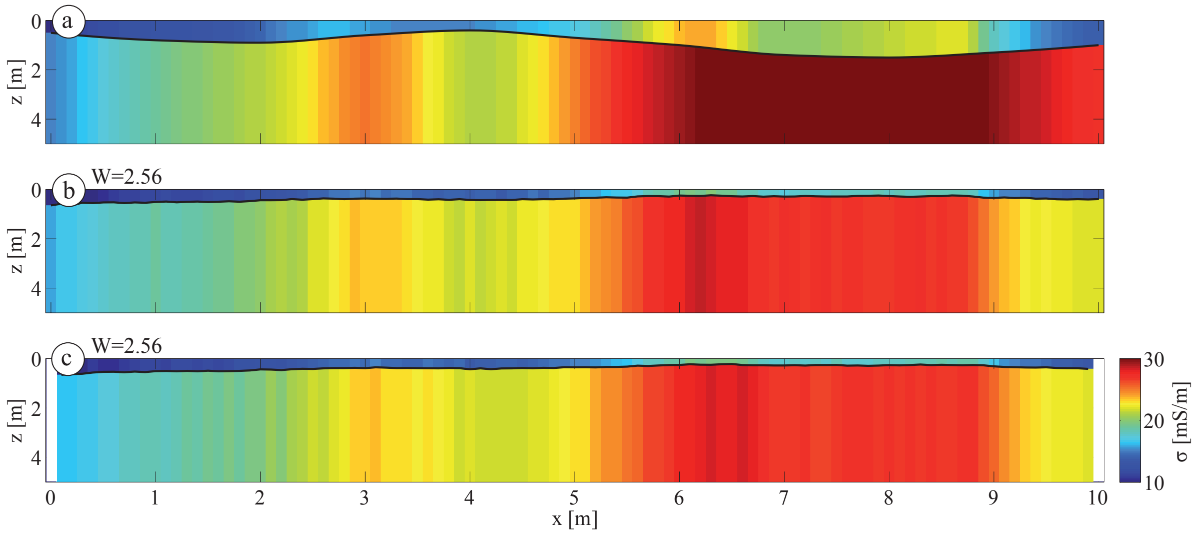

Fig. 4.17: Original underground model (a) and inversion result for best weight (w=2.56) based on L-curve criterion for m=1 (b) and m=3 (c) and 2 % noise.

To test the resolution of model parameters a method proposed by Forbriger (2003) is used. In the beginning the resulting model for the best weight (w=2.56), m=3 and 2 % noise is held constant except of one parameter, which is varied until the misfit increases 10 %. Then this parameter is held constant and the inversion is carried out while the other parameters may vary to reduce the misfit. This procedure is done successively for all three parameters. The resulting possible models, which lead to a misfit increase of less than 10 % are shown as shaded areas in Fig. 4.18 (for 4 points), whereas the initial solution is shown as red line. Additionally the starting models and the true models are indicated. For x = 4 m the true depth of the interface is shallowest (about 0.4 m) and the inversion results resemble the true model very well, especially in depth. The electrical conductivities resemble mainly the starting values, but the deviation from the true model conductivities is only about 1 mS/m, which is satisfactory. The resolution is high, which is shown by the small shaded area.

For the other points the true depth of the interface is deeper, in particular for x = 8 m (z = 1.5 m). In this special case the resolution is high, but the inverted depth is too shallow, which might be due to a local minimum in the misfit function. Nevertheless, the orders of magnitude of the conductivities are determined well. For x = 2 m and x = 6 m the depth of the interface is around 0.9 m and for the starting model at around 0.8 m, but the inversion leads to a shallower depth. The large shaded area indicates that the depth is not well resolved and also the layer conductivities have worse resolution compared to the other two points. Nevertheless, the true model conductivities of the first layer lie inside the shaded area, whereas the conductivities of the second layer are slightly underestimated.

The bad results for deeper interfaces might be explained by the cumulative response functions of the EM38DD (Fig. 4.1) that are not sensitive to this depth anymore. This is especially valid for the second oberservation height (55 cm).

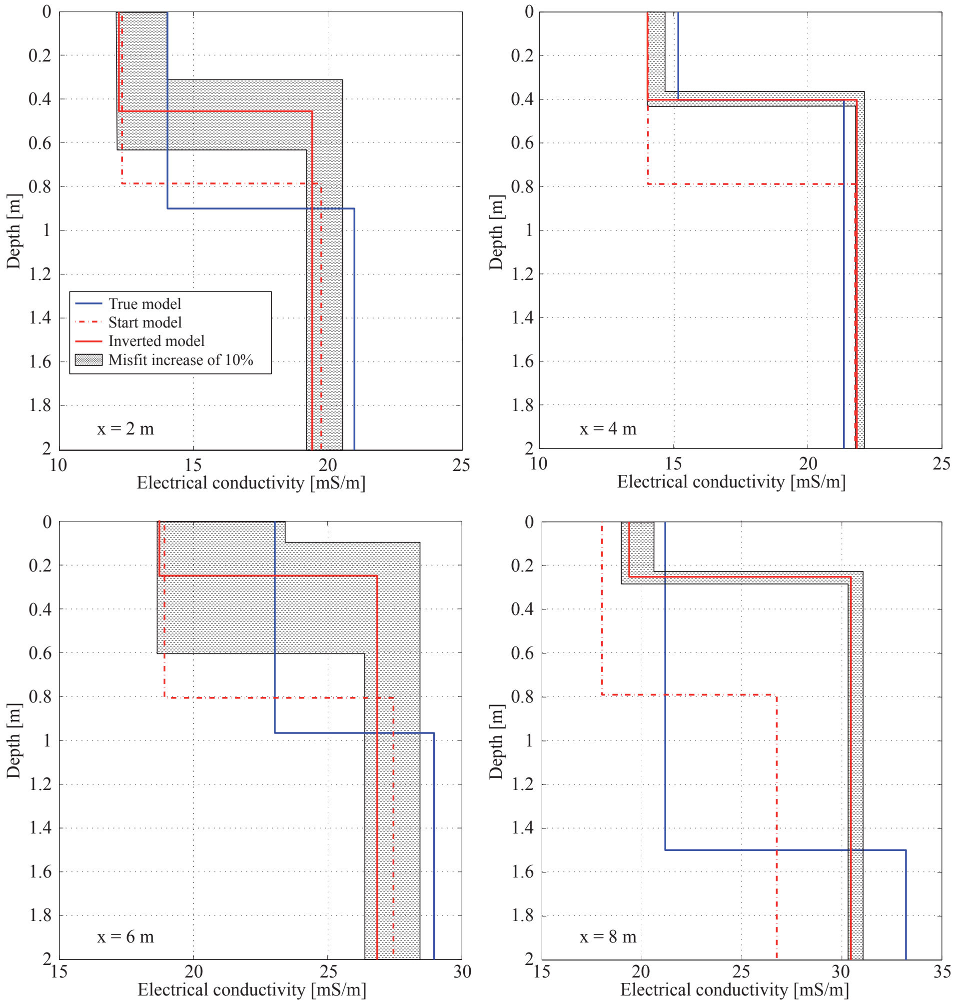

Fig. 4.18: Test results for the resolution of model parameters using m=3 and noisy data.

4.3.6 Summary for the inversion of synthetic data

The inversion with only one height is not feasible, because the system is underdetermined. The simple inversion with two heights yields very good results, but the addition of 2 % noise leads to large jumps (and sometimes negative model parameters, which are not valid) and missing values (were the inversion does not converge). The inclusion of neighbouring points does not bring much improvement for the noisy case. The best inversion results and a stabile inversion procedure can be achieved through the inclusion of smoothness constraints and regularisation using a priori information. The most critical task in this inversion approach is the selection of the a priori information. If no independently measured a priori information are available, the starting values are used instead, which have been proven to lead the inversion into the direction of the global minimum. The choice of the regularisation parameter based on the L-curve criterion leads to a stabile inversion procedure. Choosing smaller weights leads to an instable inversion and thus to large jumps and missing values.

Regarding the inversion of real data the most critical point is to have correct a priori information that have been measured independently.

Tab. 4.1 summarises the findings of this section.

	without noise	2 % noise	
	σ/z	σ	z
1 height	-	-	-
2 heights	+	-	-
2 heights + neighb. points	+	o	-
2 heights + smoothn. constraints	+	o	o
2 heights + smoothn. constr. + a priori info	+	o/+ (strongly depending on the quality of the a priori info)	o (strongly depending on the quality of the a priori info)

Tab. 4.1: Summary of the results of the inversion approaches (- bad, o medium, + good).

4.4 Inversion of real data

For the inversion of real data two examples are available. The first was measured in Rosslau, Germany, on a sandy plot with very low clay content. The second was measured in Lany, Czech Republic, on a Cambisol soil with medium clay content. In Rosslau GPR penetration was good so that the depth of the interface between the two layers can be taken from GPR measurements. To convert traveltime into depth the velocity determined from CMP (Common Midpoint) measurements was used. The reflection of electromagnetic waves is mainly influenced by the dielectric permittivity. Therefore there is no necessity that the observed reflection and a change in electrical conductivity are coincident and thus the depth of the layer interface from GPR has to be taken with caution.

The EMI measurements were conducted using the EM38DD (1) mounted directly on a plastic sledge and (2) using a wooden plank construction to lift the EM38DD to a constant height above ground. The sledge was pulled behind a tractor. At the beginning of the project tests were carried out that proved the conductivity readings to be without influence of the tractor. Before the measurements the EM38DD was calibrated with respect to the user manual. Nevertheless a linear trend was visible in the measured data that was corrected by measuring a reference profile at the beginning and at the end.

Because the measured points are now on a two-dimensional plane the smoothness constraints have to be adapted. m=3 means that the ring of the directly neighbouring points around the inversion point is used (= 8 additional points) and m=5 uses two rings (= 24 additional points) (Fig. 4.19). Each ring of neighbouring points is weighted in decreasing order from the centre point.

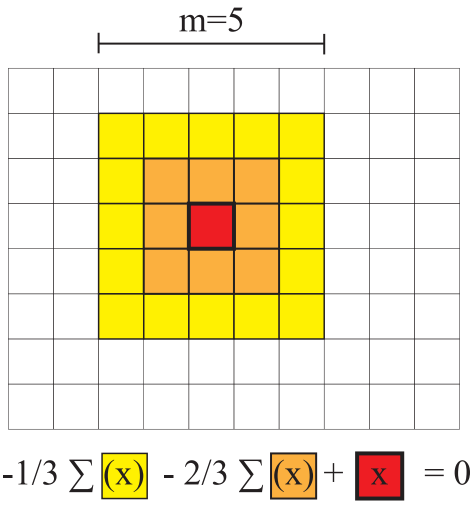

Fig. 4.19: Sketch of smoothness constraints in 2D. The actual inversion point is red, whereas the neighbouring points are weighted decreasingly with larger distance from the main point (orange and yellow). x stands for both conductivities and the depth z (and thus 3 equations).

4.4.1 Rosslau

The area measured in Rosslau is about 70 m x 10 m large and has a relatively uniform electrical conductivity distribution with larger measured conductivity in the eastern part (Fig. 4.20). The depth of the interface taken from GPR measurements varies between 0.7 and 1.5 m with larger depth also in the eastern part (Fig. 4.21).

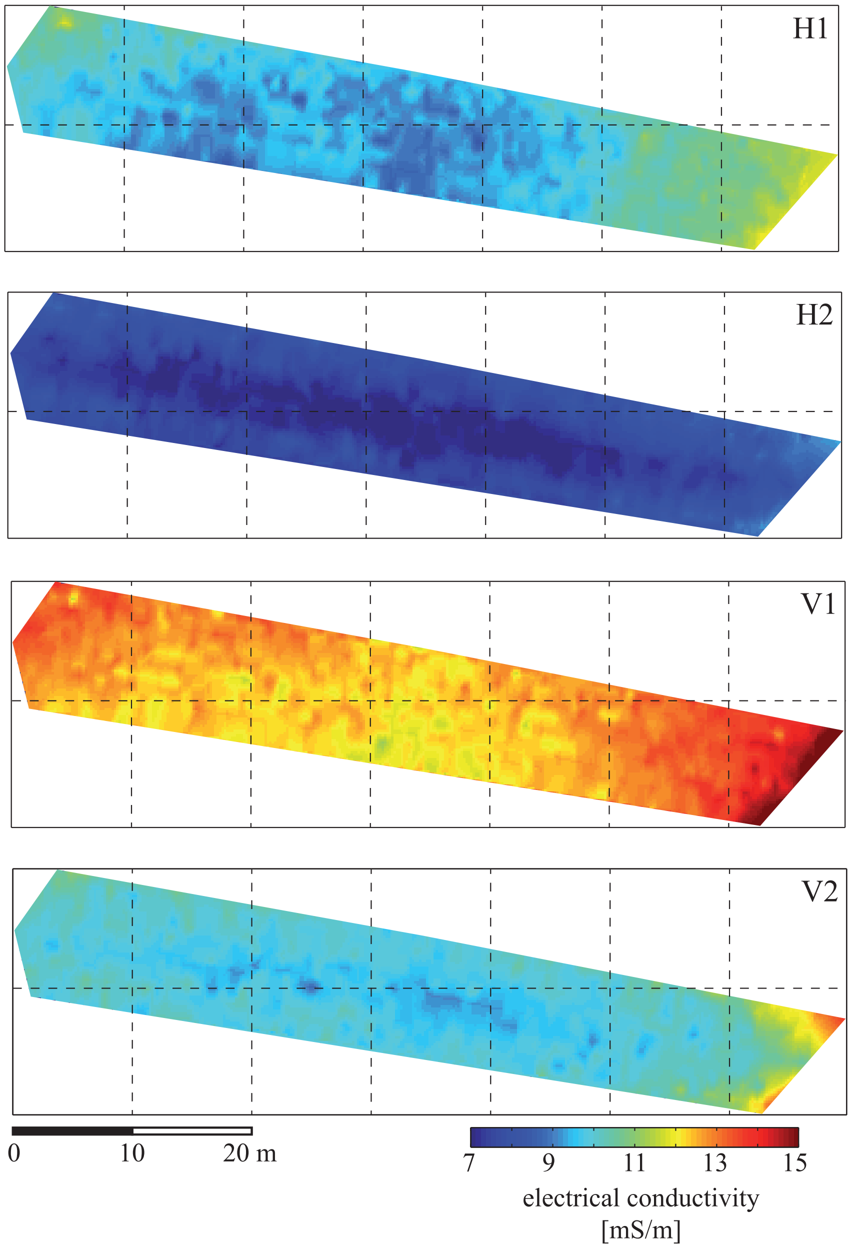

Fig. 4.20: Electrical conductivity measurements in Rosslau for vertical and horizontal modes in two heights. 1 stands for 0.125 m and 2 for 0.55 m height.

Due to the results of the inversion approaches in section 4.3 only the approach using two heights, smoothness constraints and a priori information is used. The depth of the interface is taken from GPR measurements, whereas no information is available for the conductivities. As a priori information for the conductivities of both layers the starting values are used, as was explained before in the section about the inversion of synthetic data. The weights for the regularisation using a priori information are 10^{-4}, 10^{-3}, 10^{-2}, 10^{-1}, 1, 5, 10, 50, 10^{2}, 10^{3}, 10^{4} and 10^{5}. The L-curves for m=3 and m=5 show clear corner points for w=10 (Fig. 4.22). For this weight the mean RMS error is around 15 % and on average 4 iterations are performed for each inversion point. The RMS error is highest (about 20 %) in the eastern part of the area where the expected depth of the interface is deepest (Fig. 4.23). This might mean that the a priori depth in this part is not reliable.

The correlation between measured and modelled conductivities for both heights and both coil orientations ranges between coefficients of 0.63 and 0.84 (Fig. 4.24). Especially for the lower measuring height the correlation is good, whereas the second height in horizontal coil orientation is badly represented.

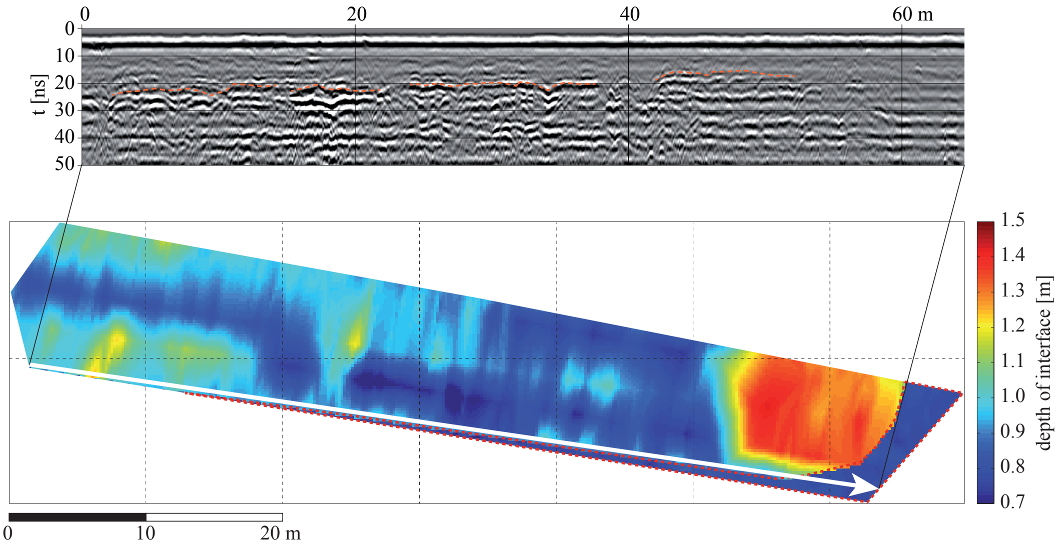

Fig. 4.21: A priori information about the depth of the interface between the two layers from GPR measurements. The area surrounded by the dashed red line indicates that no GPR measurements were available in this part and instead the best starting values are used as a priori information. The white arrow gives the position of the example radargram, in which the orange dashed line shows the picked depth of the interface.

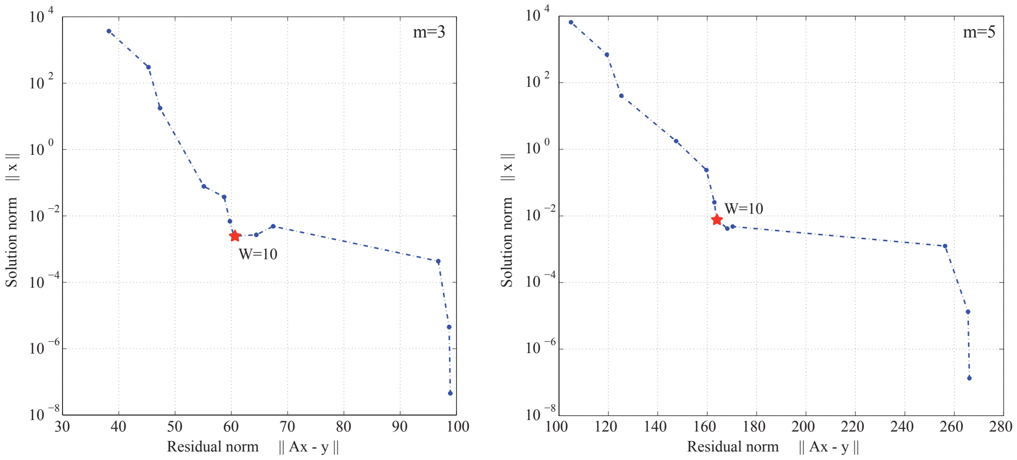

Fig. 4.22: L-curves for the inversion using smoothness constraints and a priori information with m=3 (left) and m=5 (right).

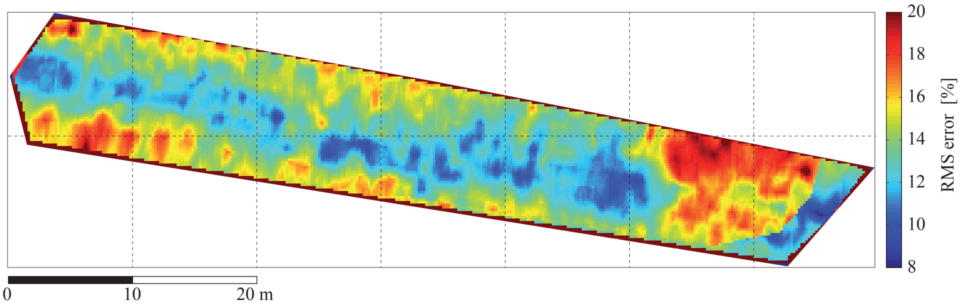

Fig. 4.23: RMS error for w=10 and m=5.

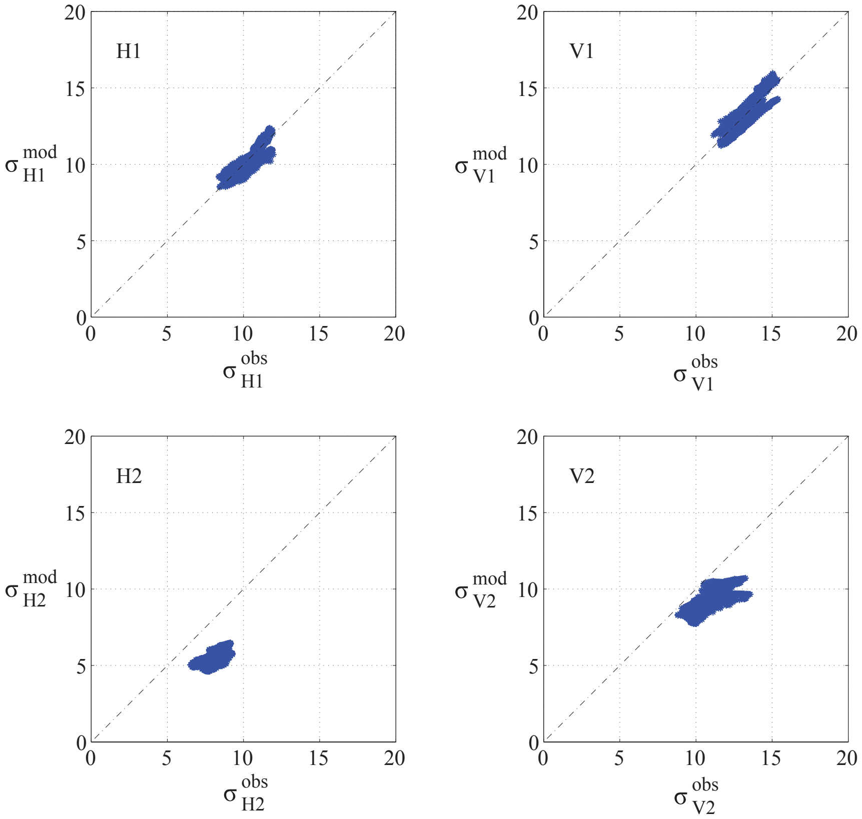

Fig. 4.24: Correlation between observed and modelled conductivities in both heights and both coil orientations. R_{H1}=0.83, R_{V1}=0.84, R_{H2}=0.63 and R_{V2}=0.75.

The inversion results for m=3 and m=5 are more or less equal and thus in the following only the figures for m=5 will be shown. The maps of electrical conductivity of the layers show similar patterns as the measured conductivity maps and also the map of the interface depth shows the same pattern as the map of the a priori information (Fig. 4.25). Nevertheless the depth is generally almost two times smaller than the a priori information. In the map of the interface depth there is a border with larger depth values around the area. This is probably caused by the missing neighbouring points for the smoothness constraints and is ignored in the interpretation of results. The sharp cut-off between a priori information from GPR and assumed starting values in the East is also copied from the a priori information to the map of the interface depth. This is not the case for smaller weights, but then the depth distribution is very homogeneous and does not represent the map of a priori information. Using larger weights the model is further smoothed and the depth values increase to reach that of the a priori information.

Especially the high RMS errors in the area of the deep layer interface from a priori information leads to the assumption that the GPR information is not reliable. Perhaps the structure that can be seen in the radargrams is just an interface with differing dielectric permittivity, but not conductivity. Thus this layer interface would not be „visible" in electric methods. An electrical resistivity tomography on a profile on the area indicates a relatively homogeneous first layer of higher resistivity up to about 1.5 m depth (Fig. 4.26). Underneath is a sharper boundary and a change to lower resistivities. The homogeneity of the upper layer is confirmed by sounding curves measured with Schlumberger configuration at two locations. The inversion of these sounding curves is highly non-unique and is thus not shown here, but the general shape of the measurement curve does not reveal any layering. Hence, the layering from GPR results is not applicable for the EMI inversion.

Because the a priori information from GPR seems not to be valuable in this case, the inversion is again carried out without (using the best starting values instead). The best weight, regarding the L-curve, is again w=10. Fig. 4.27 shows the results for the inversion with m=5. The conductivity maps of upper and lower layer show the same pattern as the previous inversion, but the depth of the interface is different. The mean RMS error decreases a little to about 13 %, but there is no maximum anymore in the east of the area. The depth of the interface varies between 0.3 and 0.6 m and might thus be the interface between topsoil and the underlying subsoil, which is observed frequently. Thus I suppose that this is the best solution for the inversion problem.

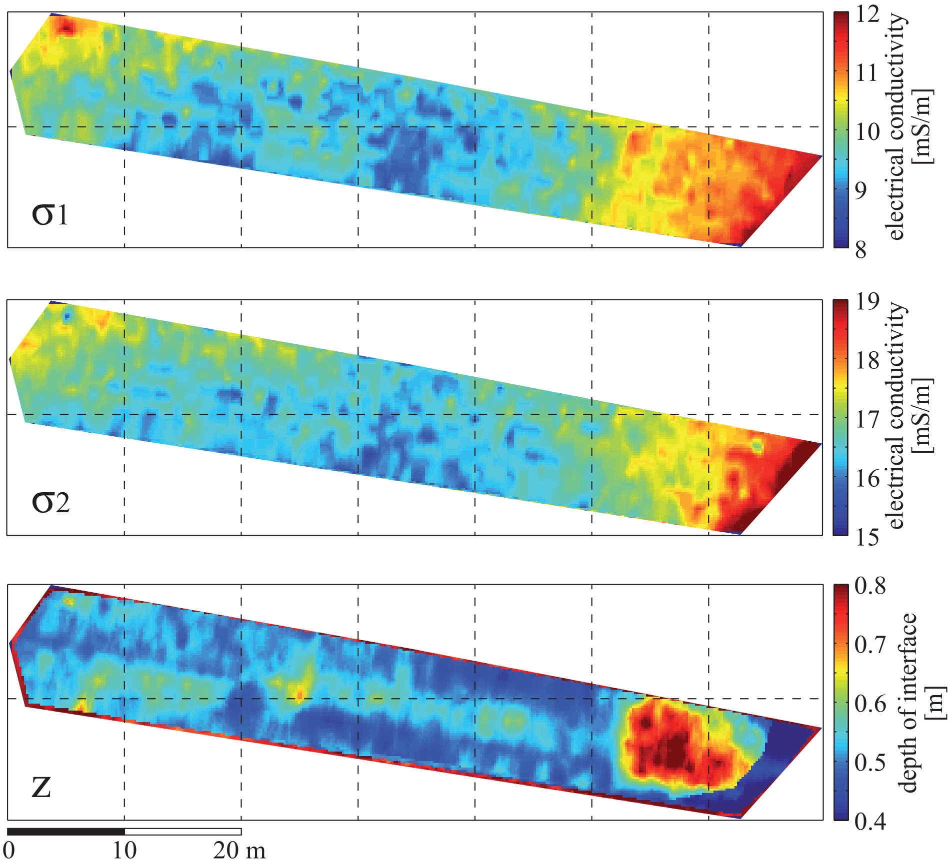

Fig. 4.25: Inversion results of σ1, σ2 and z for w=10 and m=5.

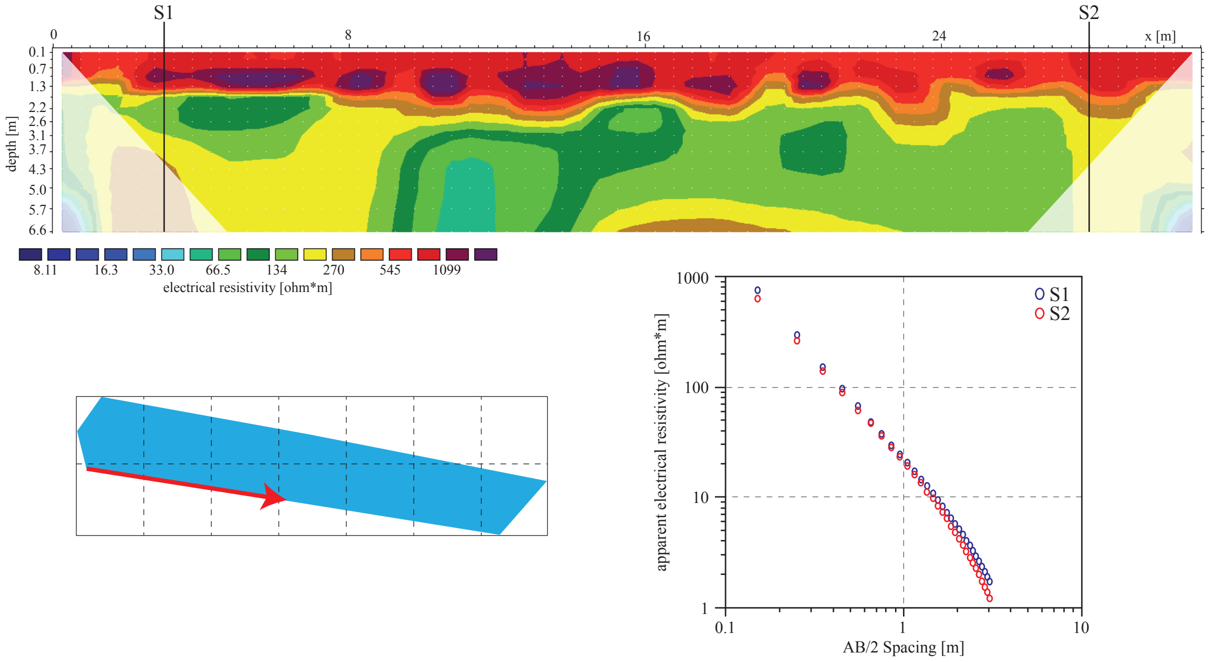

Fig. 4.26: Inverted electrical resistivity profile (Res2DInv, Loke 2011) and measurements of Schlumberger soundings at two locations. The red arrow indicates the position and direction of the profile on the measured area. Locations of midpoints of Schlumberger soundings are marked by S1 and S2.

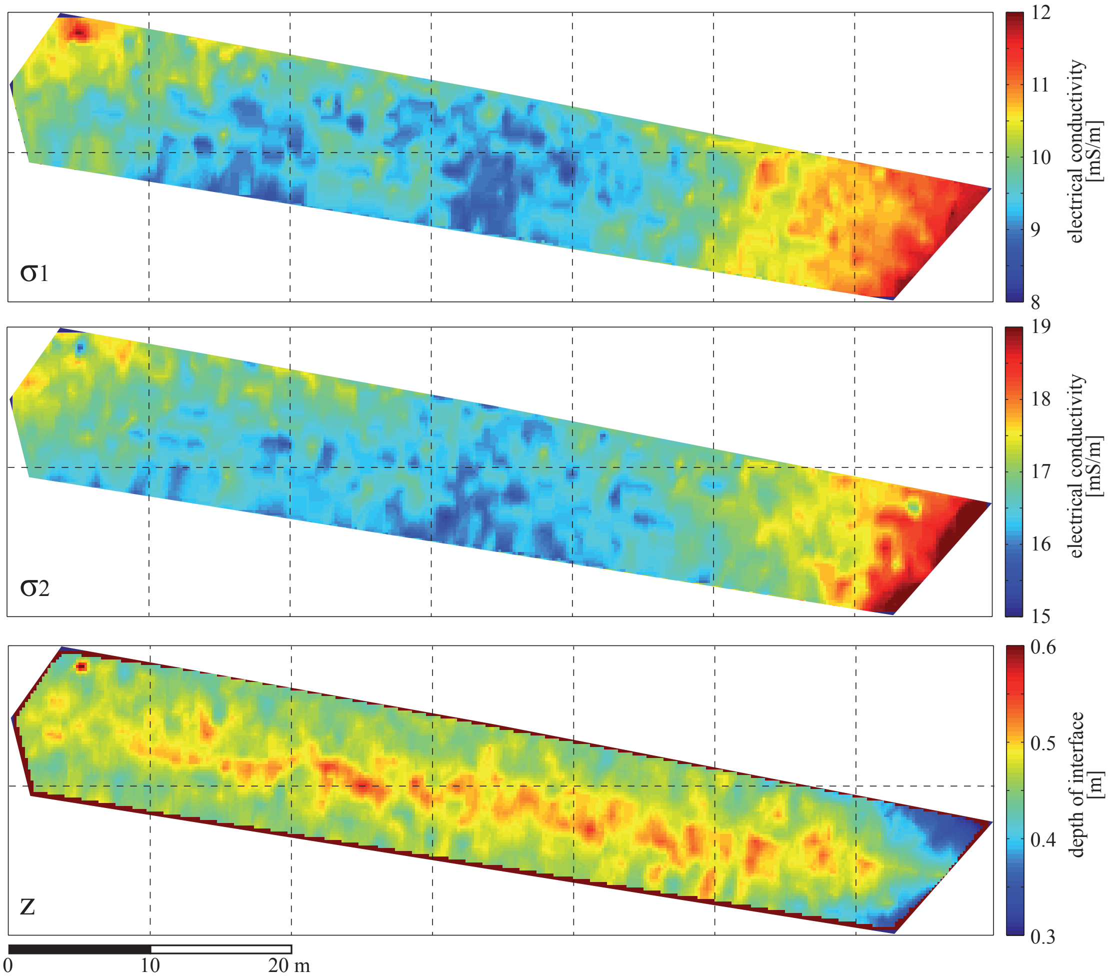

Fig. 4.27: Inversion results with starting values as a priori information for w=10 and m=5.

4.4.2 Lany

In Lany the EM38DD measurements show a high gradient in apparent electrical conductivity from south-east to north-west (Fig. 4.28). The maps from the second height show very low conductivity compared to the measurements closer to the ground. Thus this indicates that there is a relatively low conductivity layer at the surface. In Lany it is not possible to extract reliable information about a layer interface from the GPR data due to relatively low penetration and no clear continuous reflections. Thus the starting values are used as a priori information (Fig. 4.29). The L-curve for m=5 is shown in Fig. 4.30 with a corner point for w=5. Nevertheless also the results for w=10 are shown and discussed in the following section for comparison. The spatial distribution of the RMS errors for w=5 and w=10 are shown in Fig. 4.31. The northwestern part of the area has very low RMS errors < 5 %, whereas the middle part shows high values (14-20 %) that decrease again to about 10 % in the southern part. For w=5 there are some spots with RMS error close to zero. At these regions the inversion does not give good results, because the depth of the interface is negative (i.e. above ground) here (Fig. 4.32). This shows that a low

RMS error does not necessarily imply a good and reliable inversion result. The negative depth means that the regularisation parameter is too small, although it was the corner point of the L-curve. Usage of the next higher regularisation parameter (w=10) slightly increases the RMS error, but gives reasonable inversion results with positive (i.e. below the surface) depth of the interface.

There is almost no difference in the layer conductivities for the two regularisation parameters. For w=10 as the best parameter the depth of the interface varies between 0.4 m in the northwest to 1.2 m in the south-eastern part. Conductivities of both layers show a similar pattern with higher values in the north and decreasing values to the south. The correlation of measured and modelled apparent conductivities is very good with correlations coefficient > 0.96 (Fig. 4.33). The apparent conductivities in horizontal coil orientation are about 15 % underestimated, but the values in vertical orientation are well reproduced.

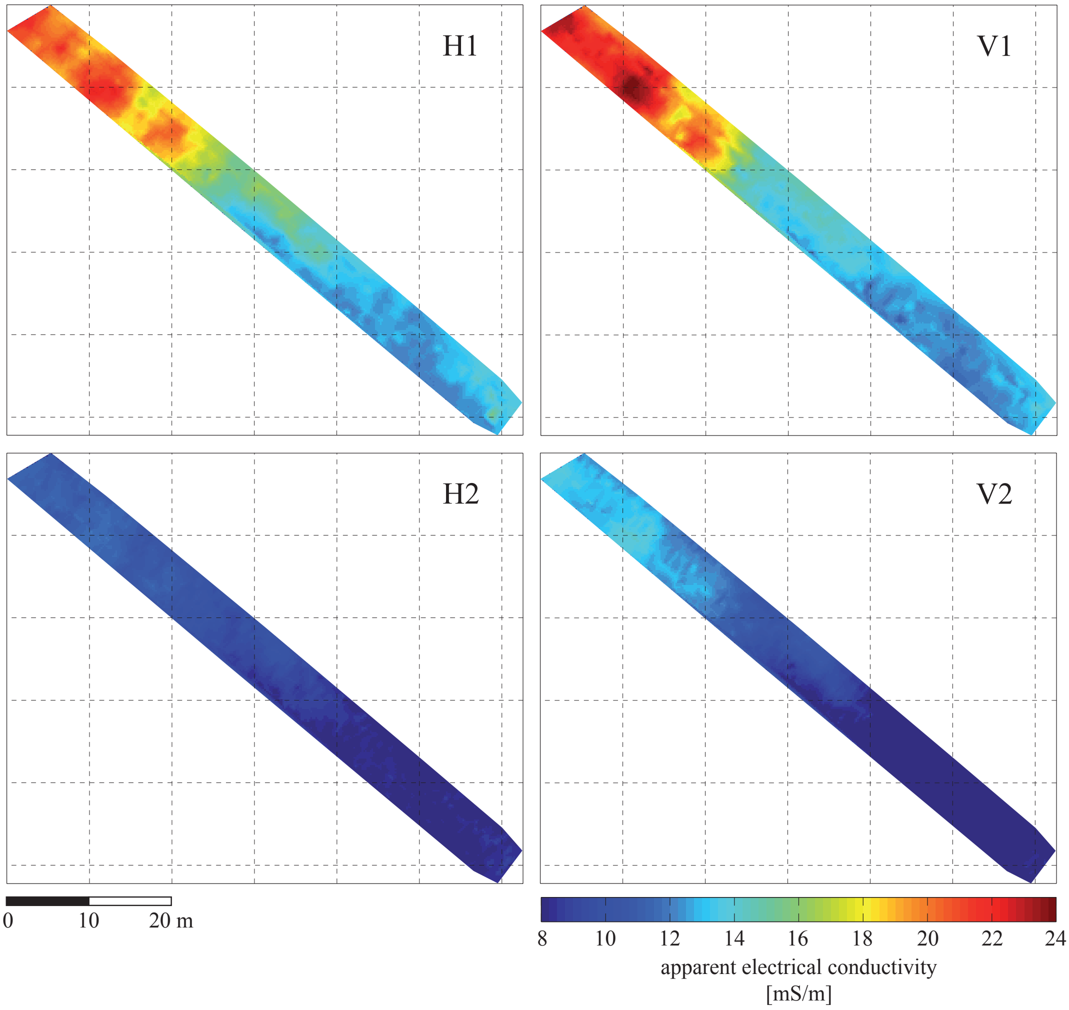

Fig. 4.28: Electrical conductivity measurements in Lany for vertical and horizontal modes in two heights. 1 stands for 0.125 m and 2 for 0.55 m height.

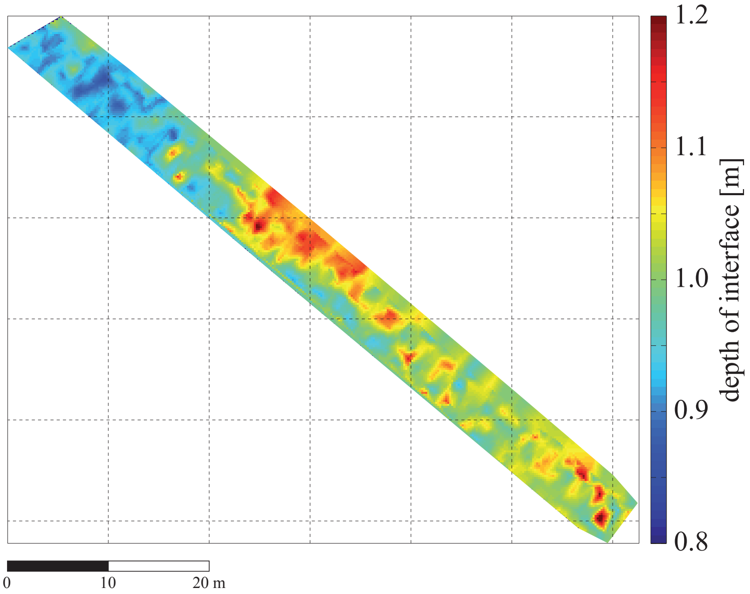

Fig. 4.29: A priori information for the depth of the interface (= best starting values).

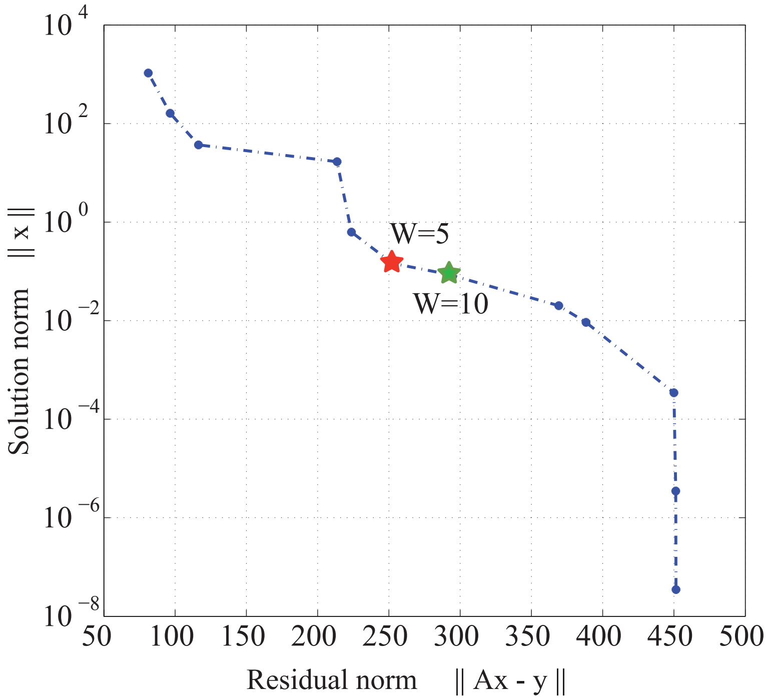

Fig. 4.30: L-curve for the inversion using smoothness constraints and a priori information with m=5. The red star is the corner point of the L-curve (w=5), whereas the green star represents w=10 as the best choice for the regularisation parameter (refer to text for details).

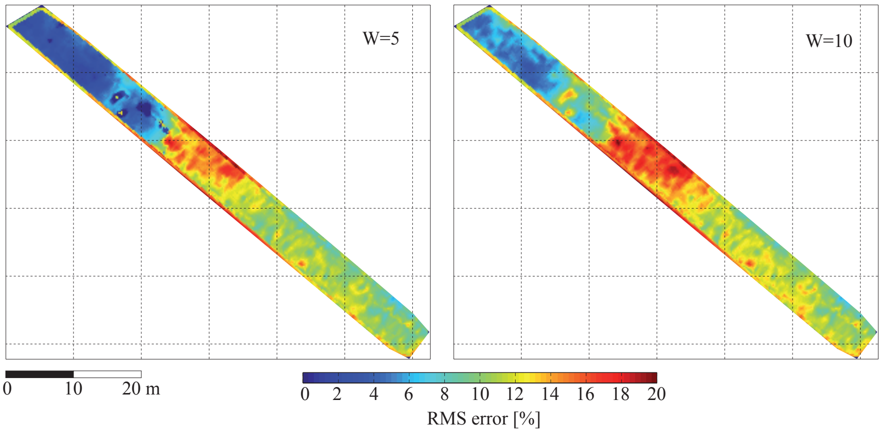

Fig. 4.31: RMS error for m=5 and w=5 (left) and w=10 (right).

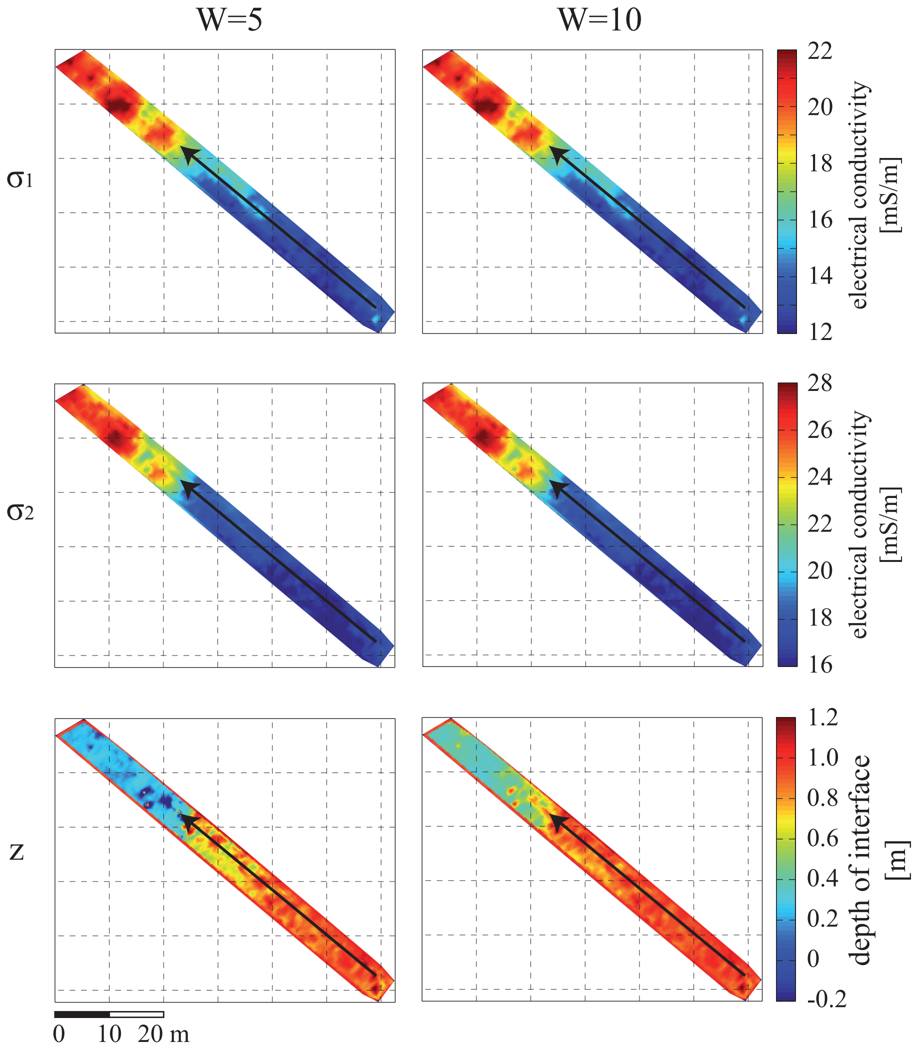

Fig. 4.32: Inversion results for both layer conductivities and depth for m=5 and w=5 and w=10. Note that the colourbar of the depth of the interface is also including negative values. The arrows indicate the position and direction of the geoelectric profile.

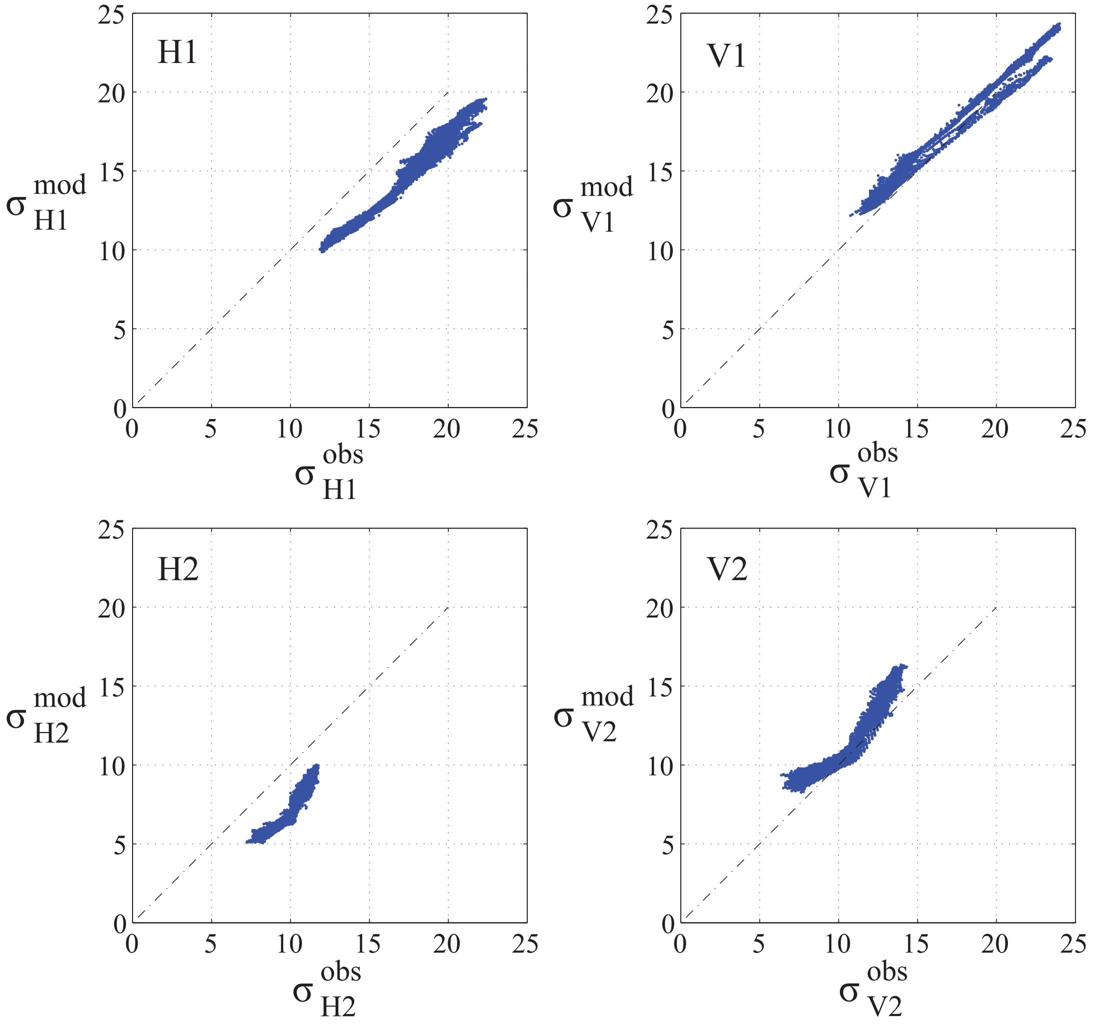

Fig. 4.33: Correlation between observed and modelled conductivities in both heights and both coil orientations. R_{H1}=0.99, R_{V1}=0.99, R_{H2}=0.96 and R_{V2}=0.96.

A geoelectric profile was measured in the middle of the area (location and direction see Fig. 4.32) using a RESECS equipment (GeoServe) and an electrode distance of 1m. The apparent resistivity values were inverted with the software Res2DInv (Loke 2011). Afterwards the resistivities were transformed into electrical conductivities for better comparison with the EMI inversion results (Fig. 4.34). The general structure of the geoelectric profile is a three-layer model (Fig. 4.34). The uppermost layer has relatively low conductivities down to a depth of about 1m. In the second layer the conductivity increases to more than 20 mS/m especially in the north-western part and than decreases again in the third layer (< 10 mS/m) below a depth of about 2 m. The resulting depth of the interface from the EMI inversion (m=5 and w=10) is marked by a black line and agrees well with the interface between first and second layer in the geoelectric profile (Fig. 4.34 a). Fig. 4.34 b shows the EMI inversion result in the same colorscale and reveals that the conductivities are much smoother in profile direction. The first layer has generally higher values compared to the geoelectric profile. The second layer of the EMI model has higher conductivities in the south-eastern part and lower values to the northwest. Plotting the

EMI model in a more suitable colourscale (Fig. 4.34 c) shows that the general trends in profile direction are the same with increasing conductivities to the northwest. Even the high conductivity areas for 30 m < x < 35 m and x > 45 m can be found in both models. This comparison confirms that the results of the EMI inversion are reliable.

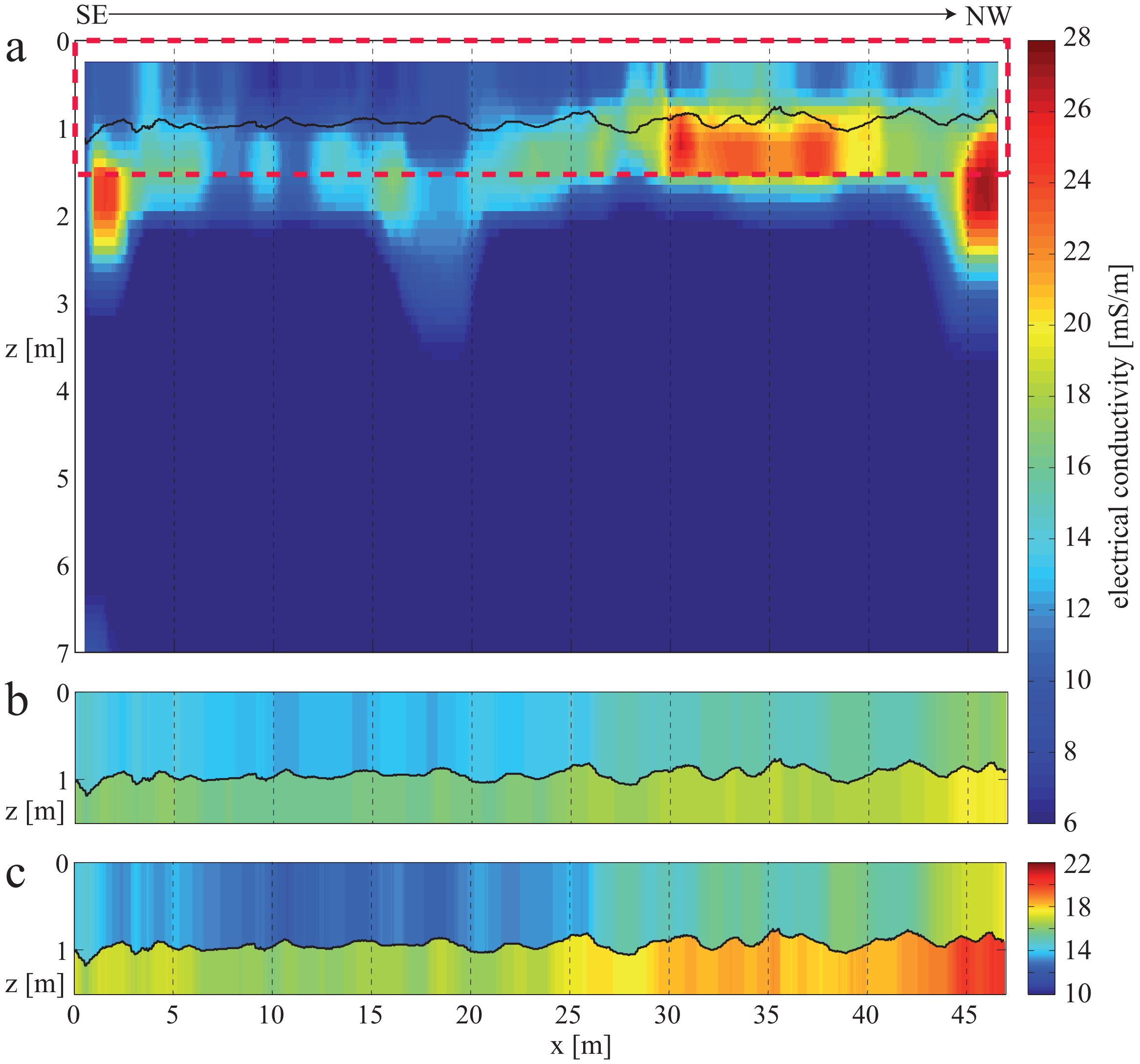

Fig. 4.34: Comparison between inverted geoelectric profile (a) and results of EMI inversion with m=5 and w=10 (b and c). The dashed red box in a indicates the area shown in b and c. a and b have the same colourscale, whereas c is the same as b but with different colourscale. The black line indicates in all pictures the depth of the interface from the EMI inversion.

4.5 Discussion

The aim of the inversion of synthetic data was to test different inversion approaches and to have the possibility to check the results compared to the true underground model. These tests showed that the best results can be achieved using smoothness constraints including neighbouring points and the Tikhonov regularisation using a priori information. The choice of the regularisation parameter was carried out with the help of the L-curve. For typically shaped L-curves this seemed to work well, whereas sometimes the behaviour of the curve was atypical and the approach of taking the corner point failed. Gebbers et al. (2007) also found that the L-curve approach is not always the best choice for picking the regularisation parameter. They also used EMI measurements in different heights above the ground and inverted them to yield an underground model. Gebbers et al. (2007), Deidda et al. (2003) as well as Borchers et al. (1997) used the equations from McNeill (1980) that are linear with respect to the conductivities. The difference to my approach is that they used several layers of constant thicknesses and thus only inverted for the conductivities of these layers. In my case, using a two-layer model with unknown layer depth needs linearisation of the equations, because they are not linear with respect to depth. But this can be realised easily with the help of Taylor series expansion. The advantage of using a two layer case with variable depth is that there are only three unknowns for each inversion point and that the depth of the interface is determined directly instead of searching for a large jump in conductivities between layers. A disadvantage might be that smooth ramplike conductivity profiles may not be resolved as was the case for the inversion of real data from Rosslau. Nevertheless this is also a problem using small constant layer thicknesses as in Gebbers et al. (2007). Hendrickx et al. (2002) compared the linear model by McNeill and a non-linear model for the inversion of EMI data measured in different heights. They found that for conductivities < 100 mS/m both models yield similar results. The non-linear model needs more computation time and is superior only for very high conductivities. Because the conductivities observed in my examples are much smaller than 100 mS/m the model by McNeill (1980) proved to be applicable. Hendrickx et al. (2002) also stated that the inversion is stronger biased by measurement errors and noise than by the simplification using the linear model.

The inversion of the synthetic data with depths larger than about 1 m has shown that the EM38DD is not able to resolve an interface at this depth reliably. This is due to the limited sensitivity at this depth, especially for larger observation heights.

A problem that occurs in real data is the calibration of the EM38DD. As Nüsch et al. (2010) pointed out it is almost impossible to measure reliable absolute values with the EM38DD. By taking care about calibration errors it is possible to measure reliable relative values and also the correlation between different instruments is good, but the calibration procedure is highly influenced by the person doing the calibration. Nüsch et al. showed that the values measured on the same profile with an EM38DD calibrated by different persons deviated to about 23 %. Thus the question is if the inversion can give reliable absolute results when the measurements are not giving reliable absolute measurements. This can be answered by the example from Lany. The comparison of the EMI inversion result with an inverted geoelectric profile showed that the depth of the layer interface agrees well and also the relative distribution of conductivities for the two layers as well as inside the layers is similar in both methods. The absolute values differ by sometimes more than 100 %. But one has to take into account that also the geoelectric profile has been processed by an inversion and must thus not necessarily show the true values. If the depth of the interface and the relative conductivity distribution in the layers are of interest, the inversion procedure described here gives acceptable results. To obtain absolute values a re-calibration during processing can be performed using geoelectric profiles (Mester et al. 2011) or direct push data. Mester et al. apply the re-calibration of the EMI data before the inversion, whereas the following approach re-calibrates the EMI inversion results. For this purpose the electrical conductivities of the two layers from the EMI inversion and the mean values of the inverted geoelectric profile between 0.3-0.5 m (layer 1) and between 1.3-1.5 m (layer 2) are plotted against each other (Fig. 4.35). The correlation coefficient is high (0.87) and the equation of the linear fit is $\sigma_{EMI} = 0.38 \cdot \sigma_{Geoelectrics} + 10.59$ mS/m. Thus the equation used for calibrating is

$$\sigma_{EMI}^{cal} = \frac{\sigma_{EMI} - 10.59 \text{ mS/m}}{0.38} \quad . \tag{4.24}$$

Of course this equation has to be determined for each field site independently and also for different EM38DD field calibrations on the same field.

Application of equation (4.24) to the inversion results of Lany increases the electrical conductivities of both layers (for layer 1 see top of Fig. 4.36). Comparison between the inverted geoelectric profile and the EMI inversion results before and after the inversion shows a strong improvement of the agreement between absolute electrical conductivity values (Fig. 4.36 bottom). Nevertheless, one has to take into account that the inversion of the geoelectric profile does not necessarily need to be true underground model.

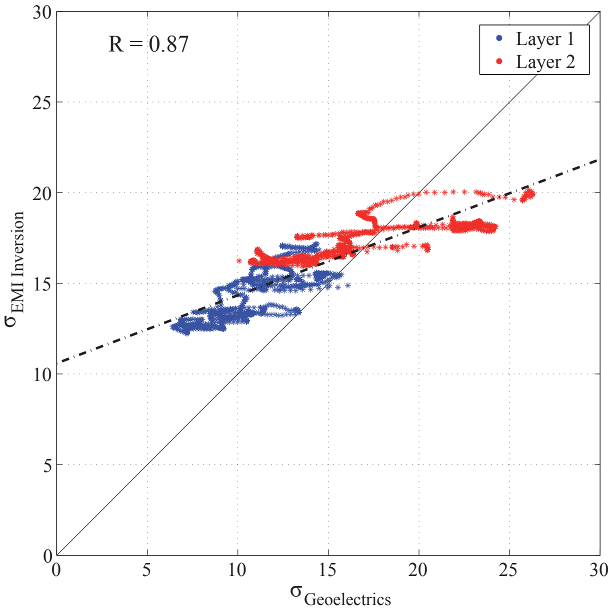

Fig. 4.35: Correlation between conductivities derived from geoelectrics and EMI inversion. Layer 1 stands for depths between 0.3-0.5 m and layer 2 for 1.3-1.5 m. The dashed line indicates the fitted linear function.

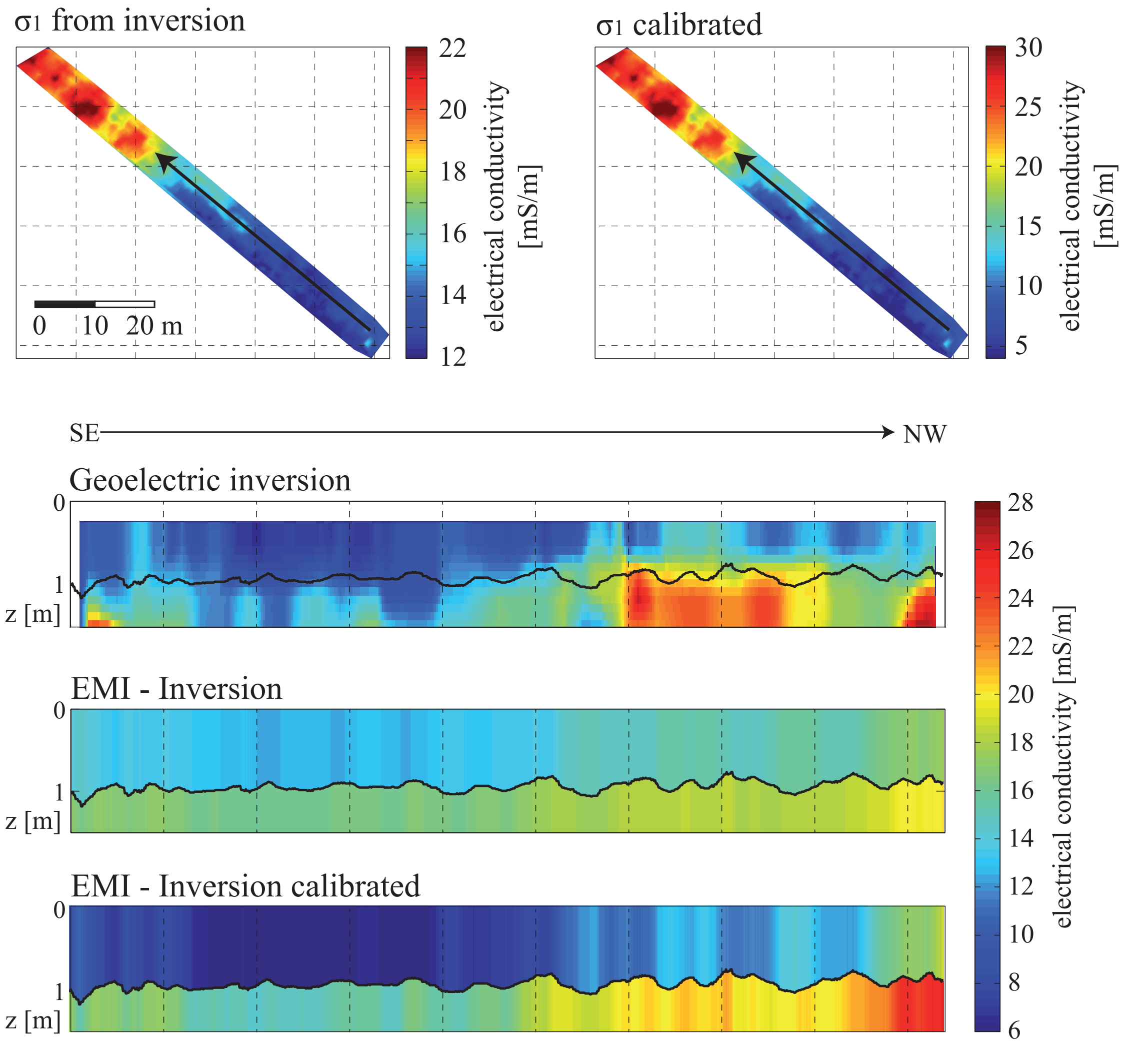

Fig. 4.36: Results of re-calibration of EMI inversion results using an inverted geoelectric profile.

4.6 Conclusion

Different inversion approaches have been tested on synthetic as well as real data of apparent electrical conductivity measurements using the EM38DD with two coil orientations and in two heights above the ground. The use of a priori information about layer conductivities and/or depth of the interface and the integration of smoothness constraints yield reliable results even for noisy data. Nevertheless there are problems with smooth and ramplike conductivity profiles and the reliability of a priori information, e. g. in a real data example from Rosslau. In Lany the comparison between geoelectric profile and the EMI inversion results showed good agreement with respect to the thickness of the first layer and the relative conductivity distributions in the layers. The disagreement in the absolute conductivity values is due to difficulties in the right calibration of the EM38DD before mesurements. Re-calibration of the EMI inversion result using the geoelectric profile yields good agreement between the absolute conductivities.

5. Principal and Independent Component Analysis for the separation of influences from water and clay contents

5.1 Introduction

Principal component analysis (PCA) is a multivariate method that transforms related data into variables that are uncorrelated (Jackson 1991). The directions of the vectors that span the new data space are the principal components and are orthogonal to each other. PCA can be used for pattern recognition in (large) datasets, to discover relations between variables and to find redundancies in multivariate datasets by projecting the data on an appropriate basis. By separating different components it is possible to extract certain amounts of the data.
Independent component analysis (ICA) is a related technique to PCA, but the independent components do not have to be orthogonal. ICA is widely used for face recognition (e.g. Bartlett et al. 2002) or is applied in medicine to electroencephalographic (EEG) records (e.g. Delorme and Makeig 2004). For face recognition ICA has been proved to be superior over PCA, especially if different expressions at different days are involved (Bartlett et al. 2002).
In geophysics there are also several fields of application. In vertical seismic profiling (VSP) a problem is to differentiate between upgoing and downgoing wave field in the data. Freire and Ulrych (1988) successfully applied PCA to VSP data to extract both wave fields and to isolate the noise. The partition of signal and noise is also import in anti-personal landmine detection using GPR. Karlsen et al. (2001) compared two ICA algorithms and PCA, where one of the ICA algorithms showed to be superior over the other two approaches for the clutter reduction of GPR data.
The partitioning effect of PCA cannot only be used for division of signal and noise but also for the division of local and regional anomaly field of gravity and magnetic data (Zhang et al. 2009). After supplementary texture analysis (of contrast and entropy) of the potential field data PCA was successfully applied to extract the regional field from the local anomalies.
Instead of separating parts from datasets PCA can be also used to compress datasets, such as images (e.g. Kaarna 2001, Abadpour and Kasaei 2008) by omitting the most unimportant principal components.

In this chapter PCA and ICA shall be applied to separate the influences of clay and water content on the electrical conductivity, because it is influenced by both factors (see Tab. 1.1). For this task the resulting electrical conductivity of the uppermost layer from the EMI inversion (previous chapter) and element concentrations from γ-ray spectrometry are used. The γ-concentrations are used as an indicator for the clay content, because it is assumed that they are dependent on this parameter only.
Further explanations on the data will be given in section 5.3.1.

5.2 Theory

5.2.1 Principal Component Analysis (PCA)

As already explained in Section 4.2.2 a m x n - matrix A can be decomposed into three matrices:

$$A = U \cdot L \cdot V^T. \tag{5.1}$$

U (m x n) is comprised of the eigenvectors of AA^T, V (n x n) of the eigenvectors of A^TA and L (n x n) is the diagonal matrix with the singular values in decreasing order as the diagonal elements (Fig. 5.1). The eigenvectors are orthogonal to each other.

If there are n=2 variables ($\mathbf{x}_1$ and $\mathbf{x}_2$) with each m observations, the columns of A are these two vectors of length m. The first principal component, containing most of the variability of the data, is then a linear combination of the first eigenvector v and the variables ($v_{11} \cdot \mathbf{x}_1 + v_{12} \cdot \mathbf{x}_2$) and the second component is a linear combination of the second eigenvector v and the variables ($v_{21} \cdot \mathbf{x}_1 + v_{22} \cdot \mathbf{x}_2$) (Dunteman 1989). The variance explained by the first principal component is λ_1 and is maximal (Fig. 5.2).

$$A = \begin{pmatrix} x11 & x21 \\ x12 & x22 \\ x13 & x23 \\ . & . \\ . & . \\ . & . \\ . & . \\ . & . \\ . & . \\ x1m & x2m \end{pmatrix} \quad L = \begin{pmatrix} \lambda 1 & 0 \\ 0 & \lambda_2 \end{pmatrix} \quad U = \begin{pmatrix} u11 & u21 \\ u12 & u22 \\ u13 & u23 \\ . & . \\ . & . \\ . & . \\ . & . \\ . & . \\ . & . \\ u1m & u2m \end{pmatrix} \quad V = \begin{pmatrix} v11 & v21 \\ v12 & v22 \end{pmatrix}$$

Fig. 5.1: Matrices involved in SVD.

Having n datasets in two dimensions, i.e. maps, each column of A is composed of the pixels of one dataset (Fig. 5.3a). After decomposition in U, L and V matrixes E_i (i = 1...n) are reconstructed using eigenvectors u_i and v_i:

$$E_i = u_i \cdot v_i^T \qquad \text{for } i = 1...n. \tag{5.2}$$

E_i is called the i-th eigenimage (Freire and Ulrych 1988). The contribution of the i-th eigenimage to the whole matrix A is dependent on the magnitude of the corresponding singular value λ_1. Thus the first eigenimage has the largest influence and contains most information. For better comparison the columns of E_i are sorted back to n two-dimensional maps that are linearly dependent on each other (Fig. 5.3b).

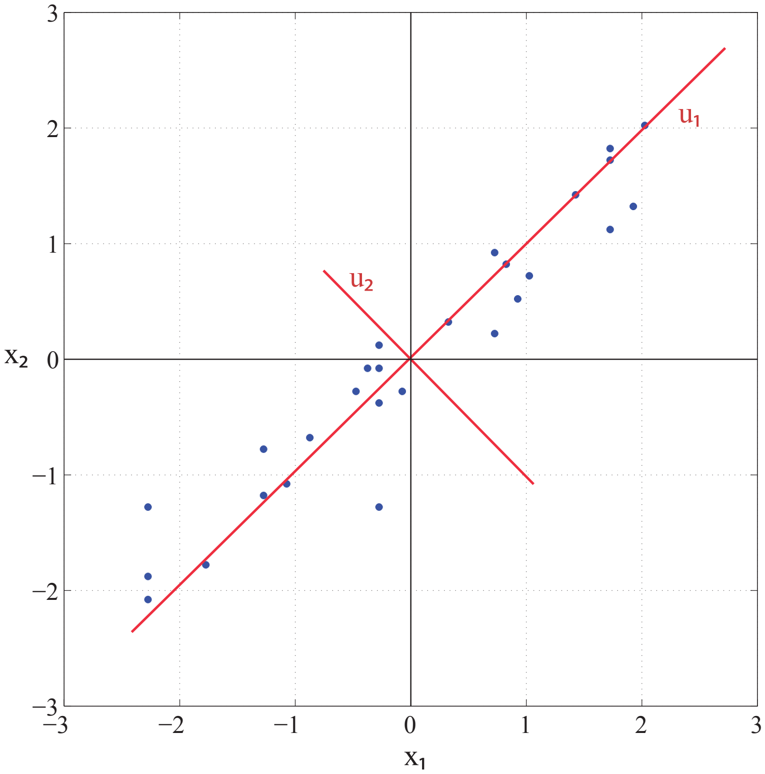

Fig. 5.2: Sketch of the principle of PCA: Observations (dots) in the original coordinate system x_1-x_2 are transformed into two new orthogonal coordinates u_1-u_2. u_1 is the first principal component (containing most information) and u_2 the second.

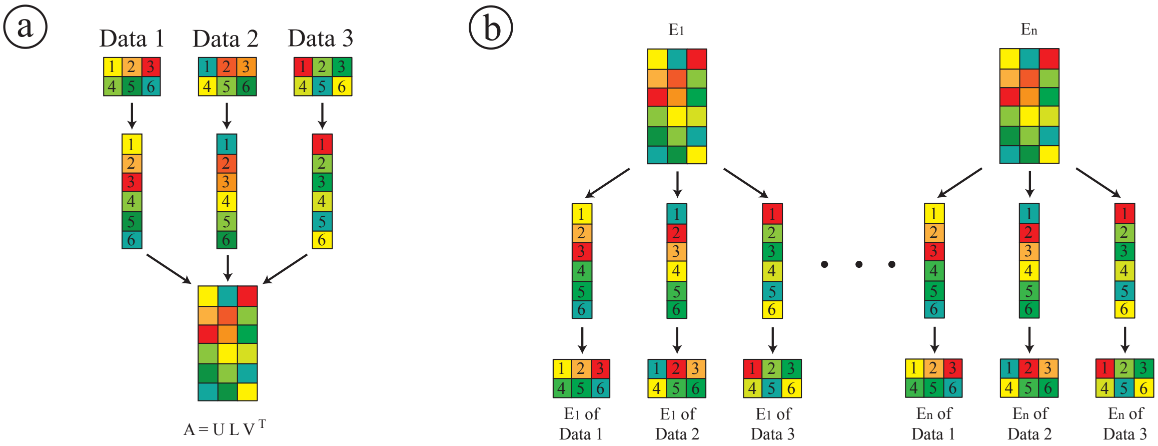

Fig. 5.3: Build-up of matrix A from three 2D-data sets (a) and the reconstruction of eigenimages (b).

5.2.2 Independent Component Analysis (ICA)

The independent component analysis can also be used to decompose a dataset into different components. In contrary to PCA these components do not have to be orthogonal, but are higher-order statistically independent (Hyvärinen and Oja 2000).
If there are n observed variables ($\mathbf{x}_1, \ldots, \mathbf{x}_n$, vectors of length m) these can be interpreted as mixtures of n independent components ($\mathbf{s}_1, \ldots, \mathbf{s}_n$, vectors of length m):

$$\mathbf{x}_i = a_{i1} \cdot \mathbf{s}_1 + a_{i2} \cdot \mathbf{s}_2 + \ldots + a_{in} \cdot \mathbf{s}_n \quad \text{for } i=1, \ldots, n \tag{5.3}$$

All coefficients $a_{i1}, \ldots, a_{in}$ (scalars) and the independent components $\mathbf{s}_1, \ldots, \mathbf{s}_n$ (vectors)are unknown and have to be determined. The problem can be also written in matrix form as

$$X=AS, \tag{5.4}$$

where matrix X contains the observed variable vectors $\mathbf{x}_1, \ldots, \mathbf{x}_n$ in its rows, matrix S the independent components $\mathbf{s}_1, \ldots, \mathbf{s}_n$ and matrix A contains the coefficients a_{ij}. The columns of matrix A give the directions of the independent components (ICs).

Restrictions
Because both A and S are unknown it is not possible to determine the absolute values of the ICs, because if one source $\mathbf{s}_i$ is multiplied by a scalar this can be cancelled by dividing the corresponding column of A by the same scalar (Hyvärinen and Oja 2000). This means that also the multiplicative sign of the independent component cannot be identified. Additionally the order of the ICs is undetermined.

Requirements for the data
Before the determination of the independent components the observed data have to be processed (Hyvärinen and Oja 2000). The first step is to centre the data, which means that the mean value of each variable is subtracted so that it varies around zero. The next step is to scale each variable vector that it has unit variance. This can be achieved by dividing each vector **x** by the square-root of its variance:

$$\mathrm{var}\left(\frac{\mathbf{x}}{\sqrt{\mathrm{var}(\mathbf{x})}}\right) = \frac{1}{\sqrt{\mathrm{var}(\mathbf{x})}^{\,2}} \cdot \mathrm{var}(\mathbf{x}) = \frac{\mathrm{var}(\mathbf{x})}{\mathrm{var}(\mathbf{x})} = 1 \tag{5.5}$$

Another requirement for the ICA is that the variables are non-Gaussian. If for example two variables had a Gaussian distribution the independent components would also be Gaussian and thus their probability density distribution would be symmetric (Fig. 5.4). This distribution contains no information about the directions of the columns of matrix A and thus the coefficients of A could not be determined (Hyvärinen and Oja 2000).

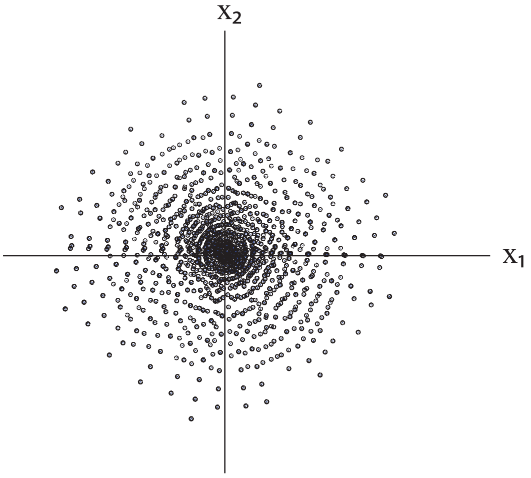

Fig. 5.4: Probability density function of two Gaussian variables x_1 and x_2.

Calculation of independent components

There are several ways of determining the independent components: Maximization of non-Gaussianity, minimization of mutual information or maximum likelihood estimation (Hyvärinen and Oja 2000) and many others that are summarized in e.g. Comon (1994). The implementation of the FastICA algorithm using Matlab by Hyvärinen and Oja (2000) is available free in the internet (http://research.ics.tkk.fi/ica/fastica/) and is used for the ICA in the following sections. It determines the independent components by maximizing non-Gaussianity using negentropy as a measure. Negentropy (J) is defined as the difference between the entropies of a Gaussian variable $H(x_{Gauss})$ and another variable H(x) (Hyvärinen and Oja 2000):

$$J(x) = H(x_{Gauss}) - H(x) \tag{5.6}$$

Entropy is the degree of information that is given by a variable, i.e. an unpredictable and unstructured variable has high entropy. For a Gaussian variable entropy is largest. Thus negentropy is always positive and is zero for a Gaussian variable. This means that for independent components the negentropy should be maximized (Hyvärinen and Oja 2000).

Relation between PCA, ICA and SVD

Vrabie et al. (2004) gives a description on how ICA is connected to SVD and with it to PCA. If a SVD is applied to a matrix A the eigenvectors in matrix V are orthogonal to each other, i.e. second-order statistically independent, and point in the direction of the principal components. The SVD is also the first step of the ICA. Based on this it has to be found a new matrix B for that is VB = V‘. V‘ contains then new vectors that are fourth-order statistically independent. One method to determine the rotational matrix B is the joint approximative diagonalisation of eigenmatrices (JADE) (Vrabie et al. 2004, Cardoso and Souloumiac 1993), but also several other methods are available (e.g. Comon 1994, Vrabie et al. 2004).

5.3 Application and Results

5.3.1 Basic assumptions

The aim of the application of PCA and ICA in the following examples is the separation of the influence of water and clay content on the electrical conductivity, because the electrical conductivity is dependent on both factors (see Tab. 1.1). For the separation of influences also other parameters are necessary. Information about the clay content can be derived from γ-spectrometry that was also measured on the same areas in Rosslau and Lany. A thallium activated sodium iodide crystal with a volume of 4 litres and an energy range of 0.1 - 3 MeV (512 channels) was used (GSCar, GF Instruments, Czech Republic). The main parameters extracted from the measured energy spectrum are the decay products of ^{40}K (Potassium), ^{238}U (Uranium) and ^{232}Th (Thorium). A fourth parameter is the Dose rate (DR), which is a linear combination of K, U and Th concentrations (e.g. Arogunjo et al. 2004). γ radiation is closely related to clay content, but there are several findings in the literature about which element concentrations are appropriate. Taylor et al. (2002), Pracilio et al. (2006) and van der Klooster et al. (2011) state that one of the best correlations to clay content is Dose rate (or total counts). Köster et al. (1988) found that Th and U correlate to clay content, whereas van der Klooster et al. (2011) prefer a linear multivariate relationship with K and Th. Hesselbo (1996) uses the ratio of Th to K as an indicator. What they have in common is that they all include Th and that K as an indicator alone is not feasible. To determine the elements that correlate well with clay content in our field examples, 52 sampling points from Rosslau were taken for comparison between measured radioelement concentrations and clay content (see Tab. A1 in appendix). The clay content was determined in the laboratory and was provided by UFZ (Helmholtz Centre for Environmental Research, Leipzig, Germany).

First, the linear correlation coefficients between clay content and K, U, Th and DR were determined (Tab. 5.1). The correlation between K and clay content is negative and has the lowest correlation coefficient. Clay content correlates best with Th and also well with U and DR. Thus U and Th seem to be good indicators for the clay content. Similar correlation coefficients were found by Petersen et al. (2012) using 13 soil samples from all iSOIL field sites. This confirms the use of U and Th as clay indicators not only for Rosslau, but also for Lany.

All radioelements correlate well with DR. Because DR is a linear combination of K, U and Th it will be neglected in the following analysis, because it does not provide additional information. The assumption for the following PC and IC analyses (with the aim to separate influences of clay and water content) is that the electrical conductivity is influenced by both factors, whereas the γ concentrations are dependent on clay content only.

	Clay content	K	U	Th	DR
Clay content	-	-0.08	0.65	0.76	0.68
K	-0.08	-	0.28	0.43	0.58
U	0.65	0.28	-	0.72	0.85
Th	0.76	0.43	0.72	-	0.94
DR	0.68	0.58	0.85	0.94	-

Tab. 5.1: Correlation coefficients between clay content and radioelement concentrations for 52 samples from Rosslau. Blue: lowest correlation, green: acceptable correlation, red: highest correlation.

5.3.2 Rosslau

PCA

The 2D data for U, Th and σ_1 are sorted into three columns to build up matrix A. Then the mean is subtracted from each column and they are scaled to have a variance of 1.

The centred and normalised data is shown as maps in Fig. 5.5, indicating very different distributions of high and low values. Then the SVD is calculated and the eigenimages for U, Th and σ_1 are calculated regarding (5.2) and multiplied by the corresponding singular value. The results are sorted back and displayed as two-dimensional maps in Fig. 5.6. Thus for each eigenimage there are three maps of U, Th and σ_1 that are linearly dependent on each other. The first eigenimage shows an anticorrelation between the γ components and σ_1, i.e. areas with positive values in γ concentrations are negative in σ_1 and vice versa. This is interpreted in a way that the spatial distribution in this eigenimage is not caused by a factor influencing both γ and σ_1. The same holds for the second eigenimages, although σ_1 is positively correlated to U, but σ_1 is negatively correlated to Th. The third eigenimage shows a positive correlation between all three components and is thus interpreted as the distribution of clay content. The first and the second eigenimage for σ_1 are summed to give the spatial distribution of the water content to electrical conductivity (Fig. 5.7).

To verify these findings TDR (Time Domain Reflectometry) measurements were conducted on 5 points in the field to yield the volumetric water content of the upper 15 cm of the soil. The locations of these points are displayed in Fig. 5.7 a. The TDR and the extracted values from the water content distribution were normalised to the interval [0, 1] and plotted in Fig. 5.8. The general trend agrees relatively well and the highest values are measured at the same point.

To approve the derived map of relative clay content I calculated the clay content distribution directly from the Th concentration. Because the correlation coefficient between Th and c_c is high (Tab. 5.1) a linear relationship can be established:

$$c_c = 5.41 \cdot \mathrm{Th} + 6.47\ . \tag{5.7}$$

The resulting map of clay content is similar to the relative clay content distribution derived by the PCA (Fig. 5.9), but the correlation is weak (R = 0.45). Nevertheless, the locations of regions with higher and lower clay content are similar.

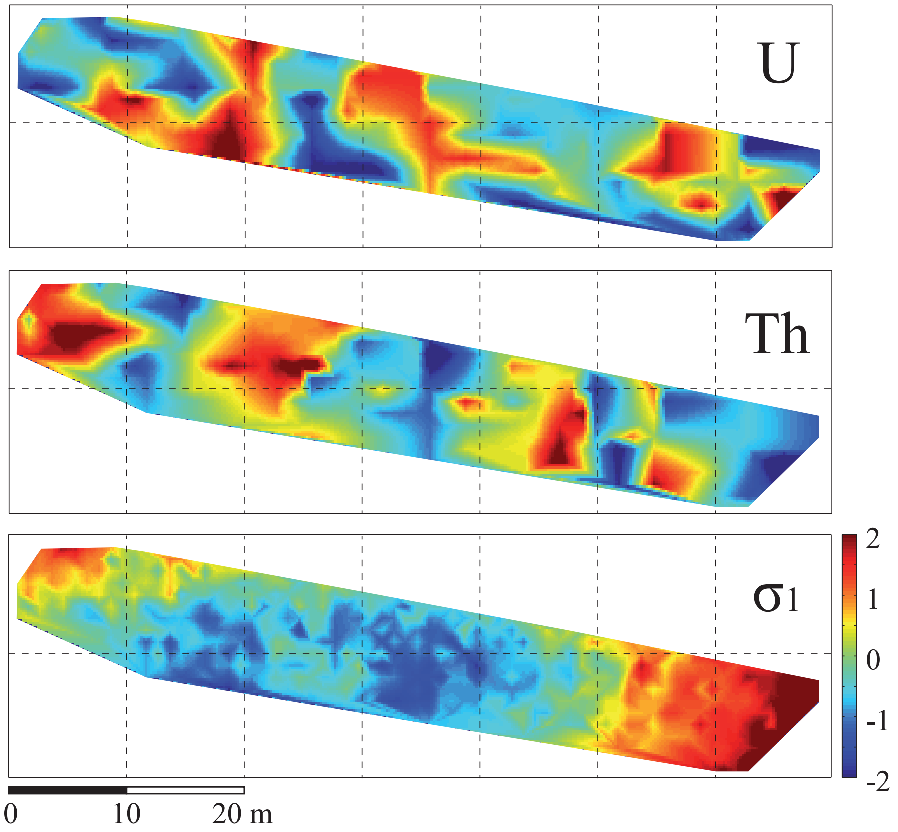

Fig. 5.5: γ concentrations of U and Th and electrical conductivity of the first layer. All parameters are centred and have a variance of 1.

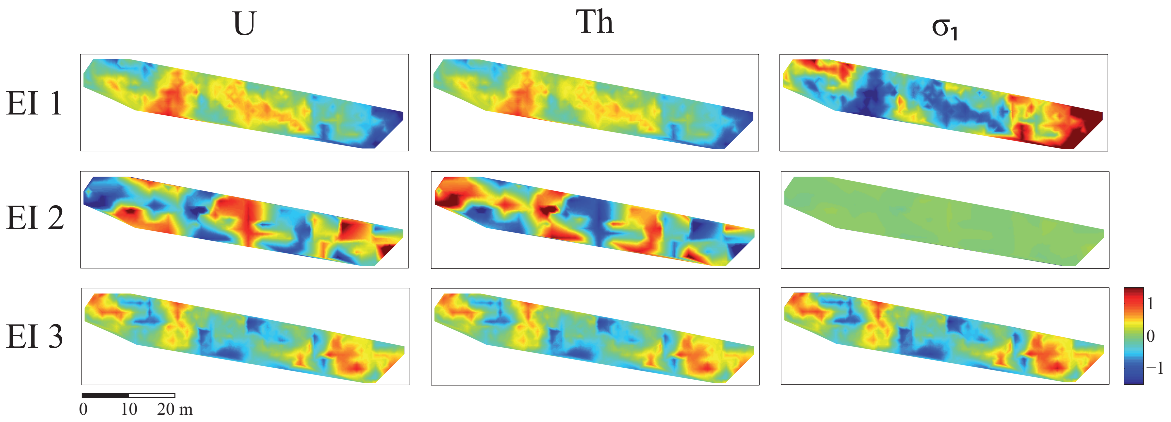

Fig. 5.6: Eigenimages for U, Th and σ_1 plotted with the same colourscale for comparison of their magnitude.

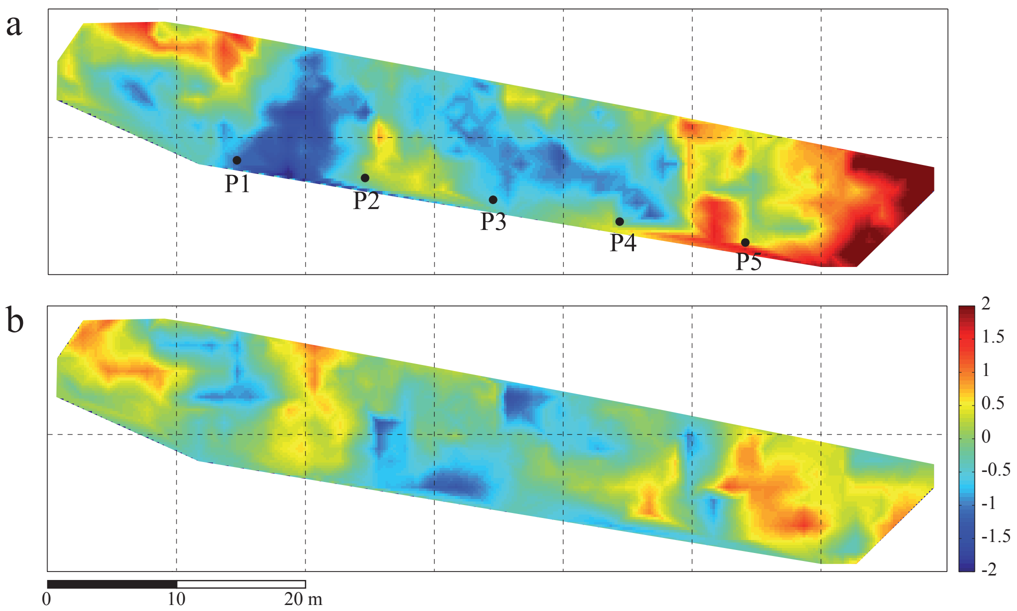

Fig. 5.7: Contributions of water (a) and clay content (b) to electrical conductivity of the first layer. a is the sum of first and second eigenimage and b is the third eigenimage. The black points show the locations of TDR measurements.

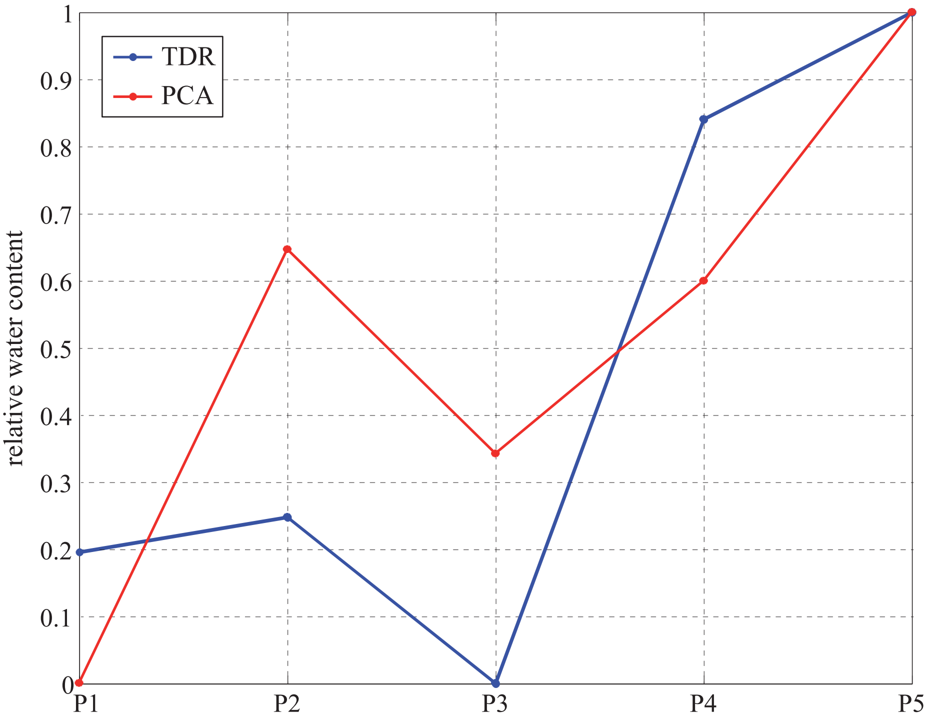

Fig. 5.8: Comparison between relative water contents derived from TDR and relative water contents determined by PCA (Fig. 5.7a).

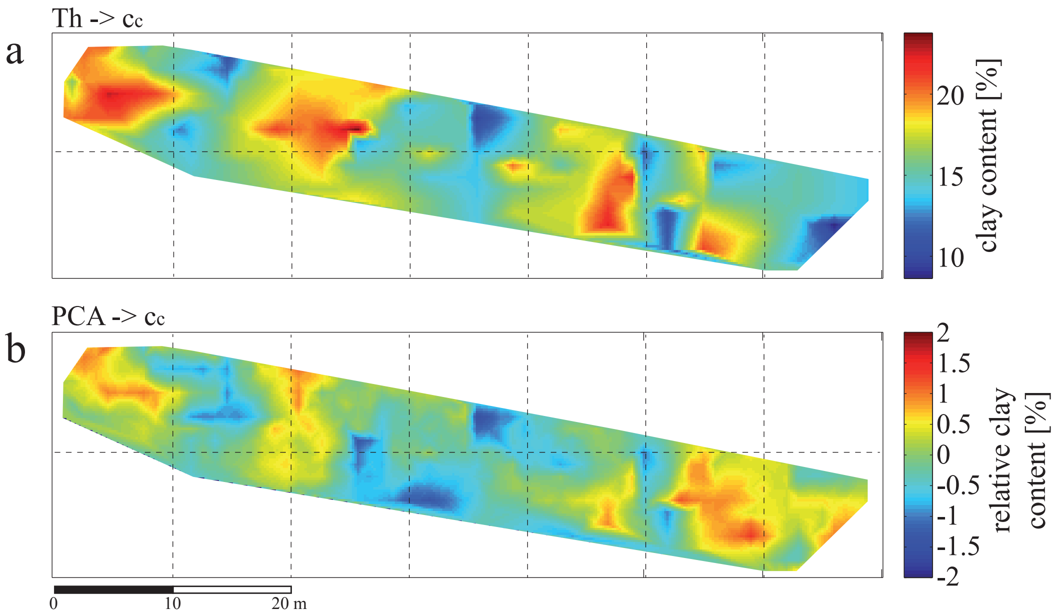

Fig. 5.9: Comparison between a clay content map derived from the linear correlation with Th (a) and from the PCA (b).

ICA

To test if the assumption of non-Gaussianity holds, histograms of the three components have been plotted (Fig. 5.10). Unfortunately they resemble a Gauss curve relatively well and thus the underlying assumption for the ICA is not satisfied. Nevertheless, the ICA has been performed as a test. For the ICA the same centred and scaled dataset of U, Th and σ_1 is used. For the computation of the independent components the FastICA algorithm by Hyvärinen and Oja (2000) is used that is implemented in Matlab. The resulting independent components are sorted back to two-dimensional maps and are shown in Fig. 5.11. They show some similarities to the principal components in Fig. 5.6.

Unfortunately the FastICA does not give the eigenvector matrix V‘ and the rotational matrix B (see 5.2.2), but only the independent components S and the mixing matrix A (eq. (5.4)). Thus it is not possible to calculate an ‚eigenimage‘ for each component as in the case of PCA. For this reason it is not possible to evaluate the correlation between components to make an assumption about the influence of clay and water content. To check the comparability to the TDR measurements different sums of independent components were investigated, but no suitable combination was found. The failure of the ICA in this case might be explained by the violation of the assumption of non-Gaussianity.

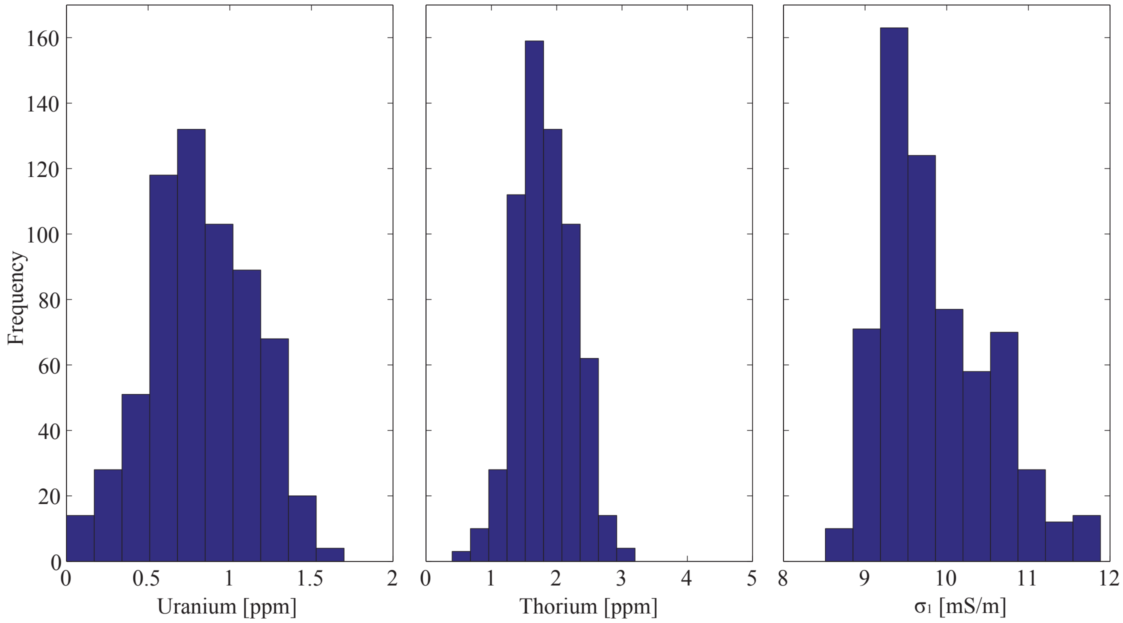

Fig. 5.10: Histograms of Uranium, Thorium and electrical conductivity for Rosslau.

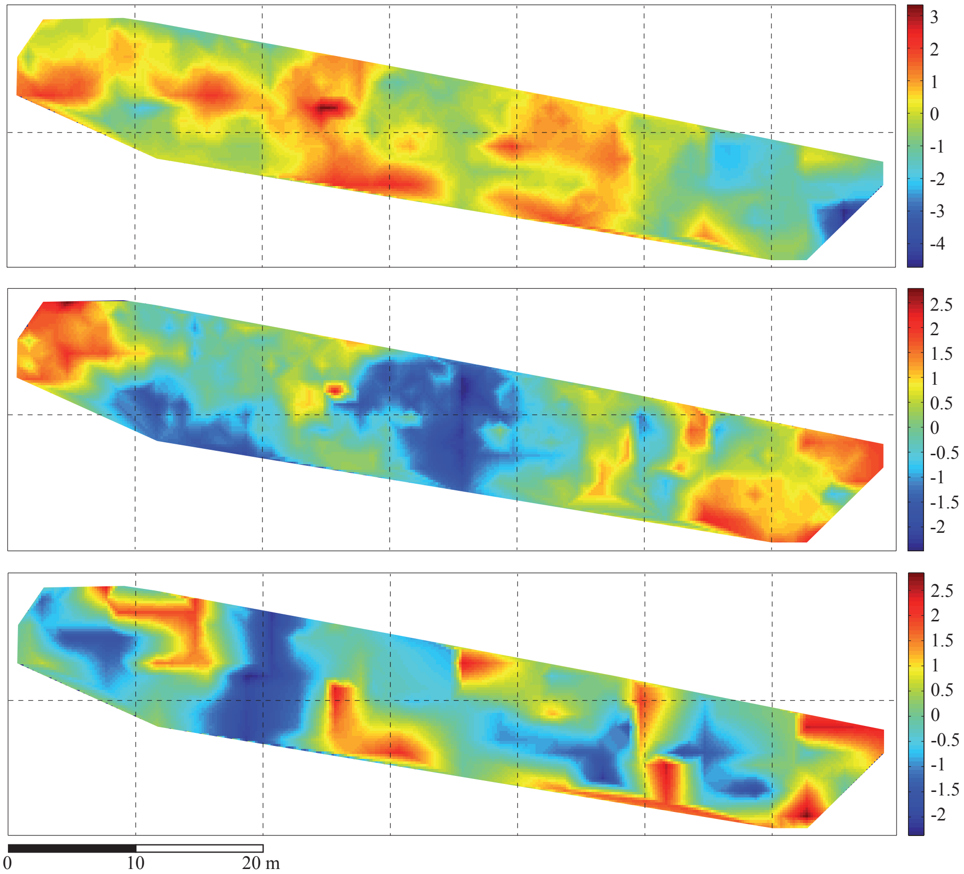

Fig. 5.11: Independent components for the matrix containing U, Th and σ_1.

5.3.3 Lany

PCA

The dataset was prepared the same way as for Rosslau and the centred and scaled maps are shown in Fig. 5.12. The decomposition into three eigenimages with each three components is plotted in Fig. 5.13. Again for the first two eigenimages γ and σ_1 are negatively correlated, whereas the last eigenimage shows a positive correlation and represents thus the distribution of the clay content. The resulting images for the spatial influence of water and clay content on electrical conductivity are displayed in Fig. 5.14. In general, the electrical conductivity is mostly influences by water content and the clay content plays a minor role, which is indicated by generally lower values for the clay content distribution. Unfortunately no TDR measurements are available at this site, so the distribution of water content cannot be proved. The comparison of the clay content map with calculated clay contents using equation (5.7) shows very low agreement (Fig. 5.15). Only some smaller features are similar in both maps, e.g. the lower clay content in the northern part.

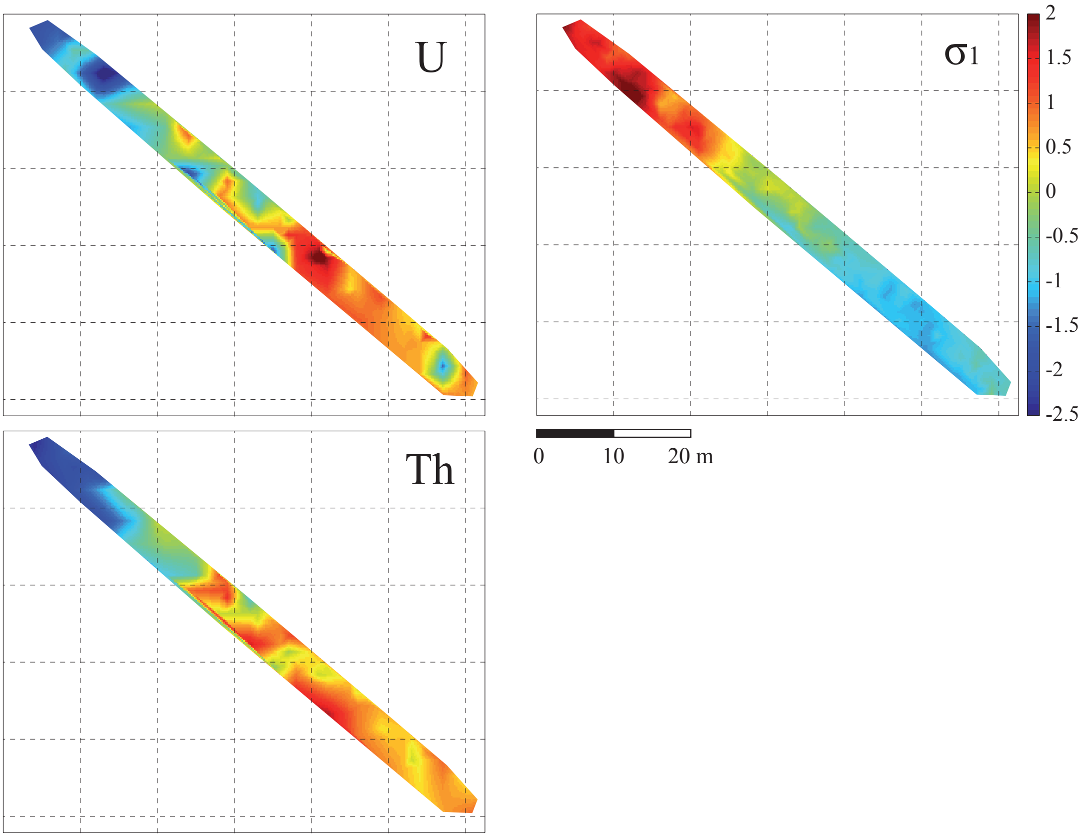

Fig. 5.12: γ-concentrations of U, Th and electrical conductivity of the first layer. All parameters are centred and have a variance of 1.

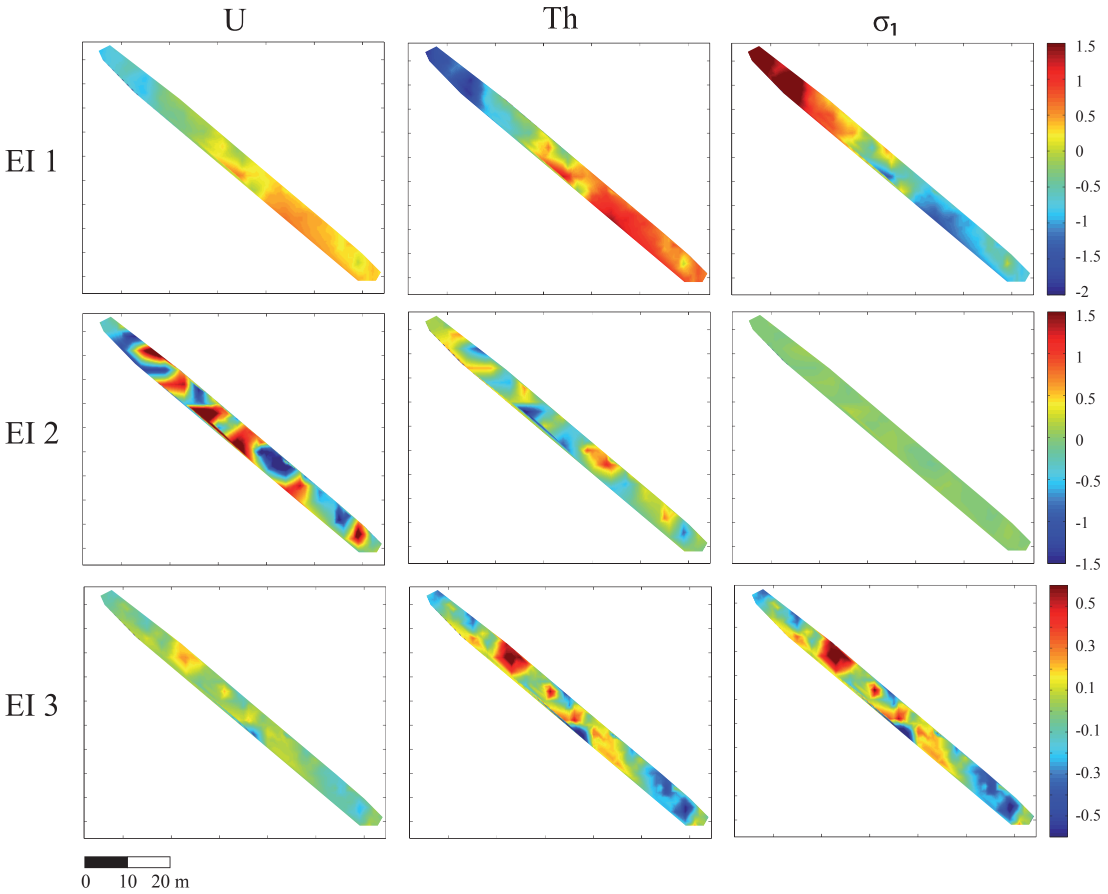

Fig. 5.13: Eigenimages for U, Th and σ_1.

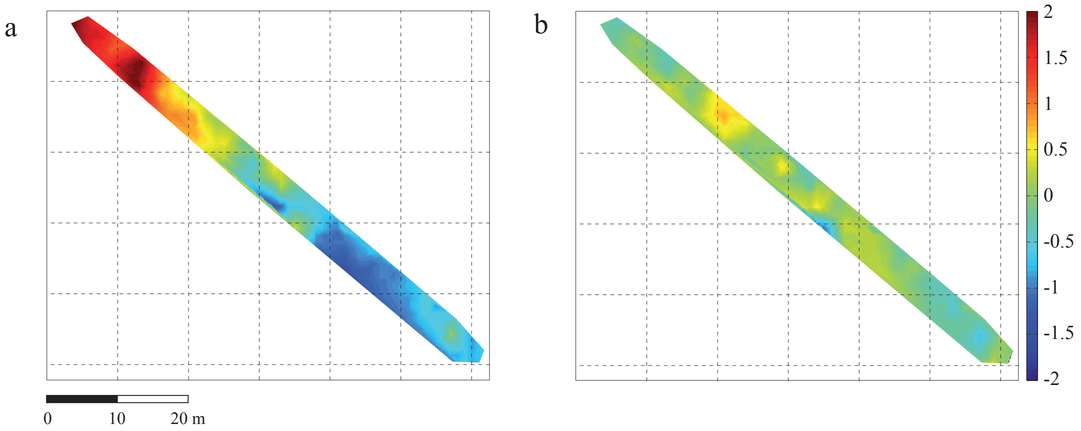

Fig. 5.14: Contributions of water (a) and clay content (b) to electrical conductivity of the first layer. a is the sum of first and second eigenimage and b is the third eigenimage.

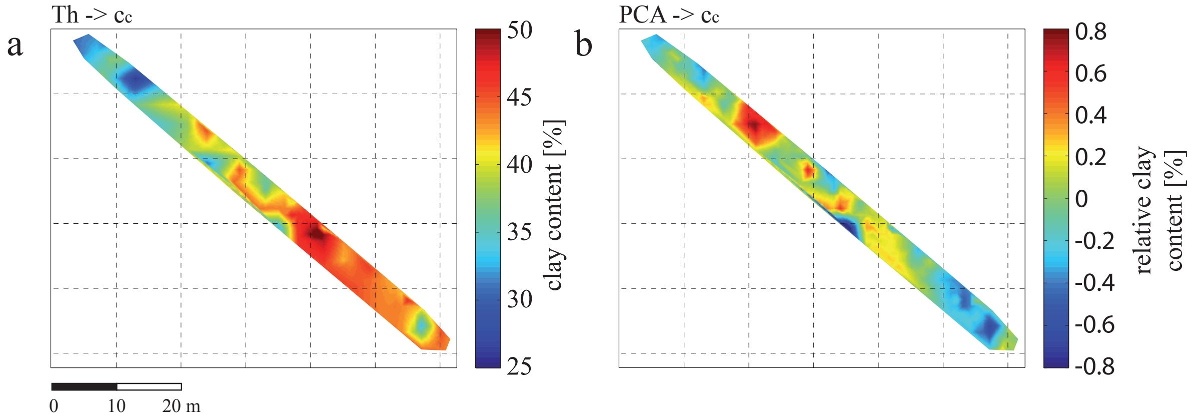

Fig. 5.15: Comparison between a clay content map derived from the linear correlation with Th (a) and from the PCA (b).

ICA

The independent components were determined as described for Rosslau and also the non-Gaussianity has been investigated (Fig. 5.16). Although U and Th show an almost Gaussian distribution, the electrical conductivity shows a bimodal distribution. Thus the assumption of non-Gaussianity is met better here.

The resulting ICs are shown in Fig. 5.17. The first independent component is very similar to the contribution of water content determined by the PCA, but with negative sign. Thus the first inverted IC might represent the influence of the water. In contrast to the PCA this component is weaker than the sum of the other to ICs that might indicate the clay content.

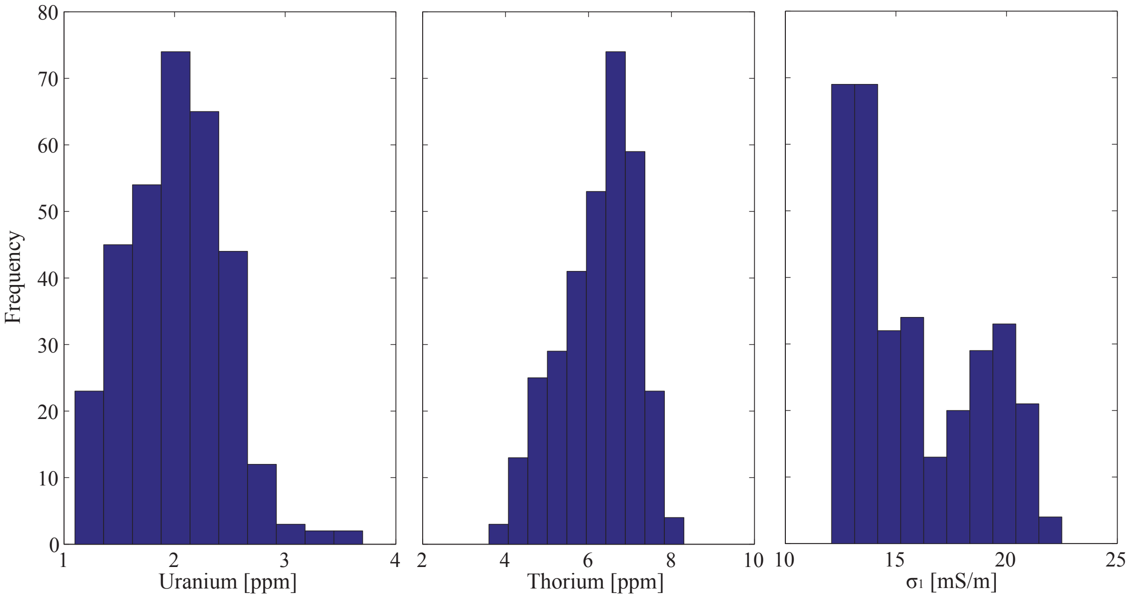

Fig. 5.16: Histograms of Uranium, Thorium and electrical conductivity for Lany.

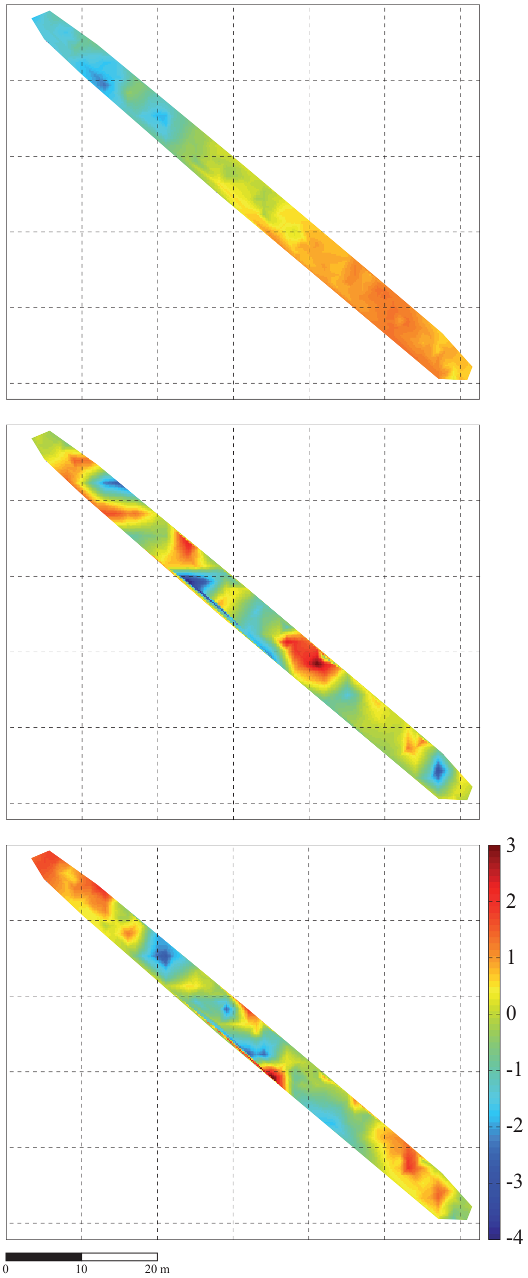

Fig. 5.17: Independent components for the matrix containing U, Th and σ_1.

5.4 Discussion

It was shown that it is possible to extract the influences of water and clay content on the electrical conductivity by PCA. The underlying assumption is that both γ-concentrations and electrical conductivity increase with increasing clay content and that the water content only affects the conductivity. This might be not completely true, because the water content also influences the γ-concentration by reducing the measured concentrations (de Groot et al. 2009). Thus the water content has an opposite effect on electrical conductivity and γ-concentrations. This in turn supports the approach to interpret the positively correlating eigenimages to represent the clay content (because both parameters increase with increasing clay content) and to interpret the negatively correlating eigenimages to represent the water content. In Rosslau a comparison with 5 points of TDR measurements showed good agreement, although this is not significant. The comparison of the derived clay content map with clay contents calculated with a linear regression between Th and c_c showed good agreement. This confirms the reliability of the PCA-approach. Nevertheless this has to be approved by further sampling and determination of clay and water content at more sampling points.

For Lany no TDR measurements were available and thus the separation of clay and water content distributions could only be verified using the linear regression between Th and c_c. The comparison between the clay content maps gave no satisfying agreement. Thus, the derived water and clay content maps have to be taken with caution.

Unfortunately the IC analysis does not lead to separate eigenimages for each parameter, so the sign of the correlation (positive/negative) between γ-concentrations and electrical conductivity cannot be used as a tool for separating the effects of clay and water content. This could only be controlled by additional sampling in the field. Nevertheless the independent components reveal patterns that are similar to the PCs for Lany. Another disadvantage of the ICA for the aim of this application is that the multiplicative sign of the ICs cannot be determined. Thus this can only be identified by additional information. The failure of ICA might be also explained by the violation of the underlying assumption of non-Gaussianity that was observed for all parameters in Rosslau and for two parameters in Lany.

Overall, the approach of using a PCA of γ-concentrations and electrical conductivity seems to give a hint at the relative spatial patterns of water and clay content, but the results should be verified by ground-truthing points. The difference between the results of clay content from the linear regression (between Th and c_c) and the PCA (using U, Th and σ) reveals that there might be additional mechanisms or dependencies that are not taken into account by the mentioned approaches.

5.5 Conclusion

The aim of this chapter was to separate the influences from water and clay content on the electrical conductivity, which increases for increasing water and for increasing clay content. For the geophysical mapping of large areas and the following interpretation in terms of soil parameters it is necessary to get an idea about the spatial distribution of both factors. In the examples from Rosslau and Lany a combination of Uranium and Thorium concentrations from γ-ray spectrometry and the electrical conductivity of the upper layer derived from the EMI inversion showed promising results by means of PCA. The second approach, ICA, did not yield satisfactory results, especially with respect to the possibilities of interpretation. The resulting maps of clay content were compared to clay contents derived by linear regression of Th and c_c, showing partly satisfactory (Rosslau) and partly bad agreement (Lany).

6. Application of results

The previous chapters investigated the relationships between measured geophysical parameters and soil parameters, i.e. water and clay content. Several approaches were introduced to calculate the clay and/or water content. Some of them were derived in laboratory and represent until now only single sampling points. The aim of this chapter is the application of the findings to areal field data to derive maps of water and clay content. The basis for this is in all cases the areal measurement of EMI data and the adjacent inversion to derive the electrical conductivity of single layers. Using an inverted geoelectric profile to re-calibrate the EMI data results in a reliable distribution of electrical conductivities.

The representative depth interval of the requested water and clay content maps is based on the investigation depth of the geophysical methods. Using the electrical conductivity map of the first layer only (from the EMI inversion) and corresponding data from other methods results in soil parameter maps representing the topsoil. This is done in the following examples.

The first approach uses GPTFs that were tested in chapter 2. One possibility is to use the electrical conductivity map resulting from the calibrated EMI inversion to derive a map of water content, e.g. by application of the empirical formula of Waxman & Smits (1968). The desired fitting parameters and the porosity can be taken from laboratory measurements, estimated or determined through calibration with in situ measured water contents (e.g. with TDR) (Fig. 6.1).

To derive a map of permittivity a linear relationship between electrical conductivity and permittivity can be used, which either is determined in laboratory (Fig. 6.2 a) or more practically is derived from the combination of several CMP in situ velocity measurements and a geoelectric profile (Fig. 6.2 b).

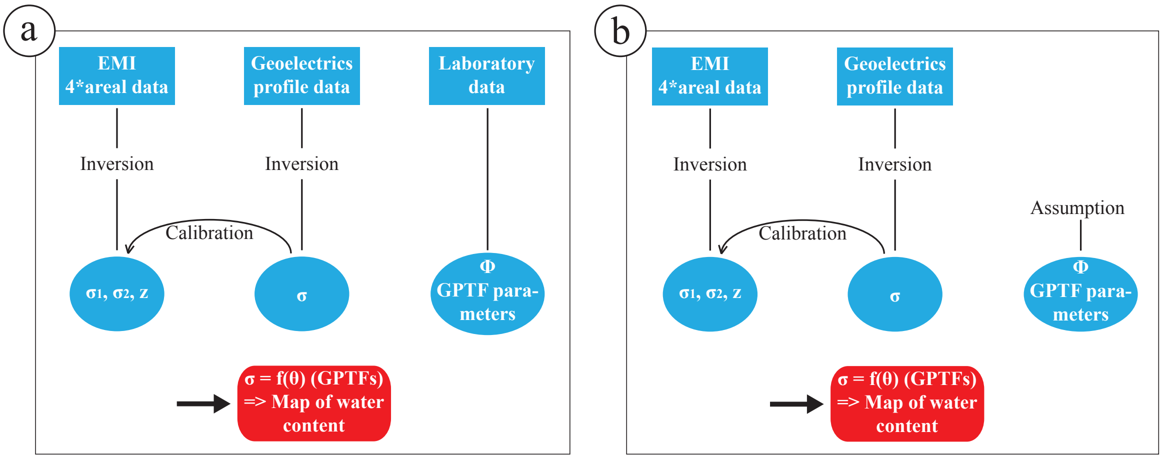

Fig. 6.1: Schematics for the derivation of water content maps from electrical conductivity using a combination of field and laboratory data (a) or field data and estimates of parameters (b).

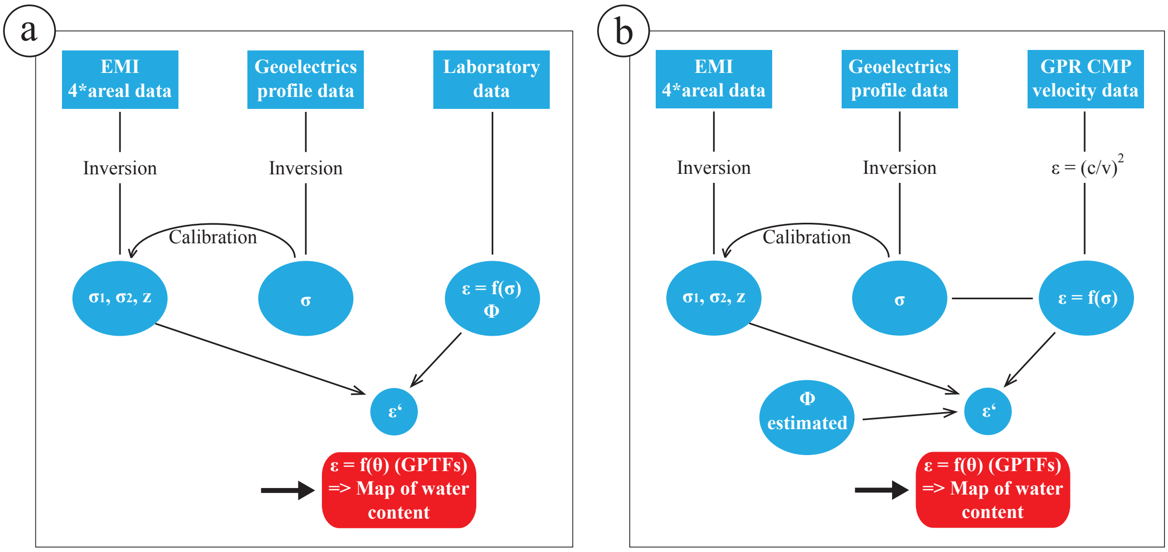

Fig. 6.2: Schematics for the derivation of water content maps from the permittivity using a combination of laboratory and field data (a) or field data and estimates of the porosity (b).

The laboratory measurements showed that for the link between permittivity and water content simple empirical and volumetric mixing models yielded good results. Thus the empirical model of Jacobsen & Schjønning (1993) and the CRIM model were used to derive maps of water content from permittivity. For the derivation from electrical conductivity the Waxman-Smits formula was used. Fig. 6.3 shows on top the calibrated map of electrical conductivity for the topsoil in Lany and the derived map of relative permittivity. The second row shows the resulting maps of water content (same color scale) and for comparison the relative distribution of water content from PCA (chapter 5) in the last row. Although the absolute values of water content differ by up to ≈10 %, the relative distribution is similar. The maximum absolute difference between water contents is 0.035, which is acceptable. The pattern of the derived water content maps is in good agreement with the relative water content distribution from PCA.

Determination of a clay content map is more complicated (Fig. 6.4). The basis is again the re-calibrated electrical conductivity of the topsoil from which a permittivity map is calculated (again using the linear relationship between both parameters). A standard (almost) zero-offset GPR survey using a 400 MHz antenna is used to derive the quality factor. From each trace the instantaneous frequency is calculated and the frequency downshift between 2 and 10 ns (representing the upper 50 cm, i.e. the topsoil) is fitted by a linear function. The slope (df/dt) of this is then used to determine the quality factor (equation (3.12)). It is then possible to determine a map of the imaginary part of permittivity (equation (3.6)). Using the empirical formula describing complex permittivity as a function of clay content (equation (3.14)), a map of clay content can be derived.

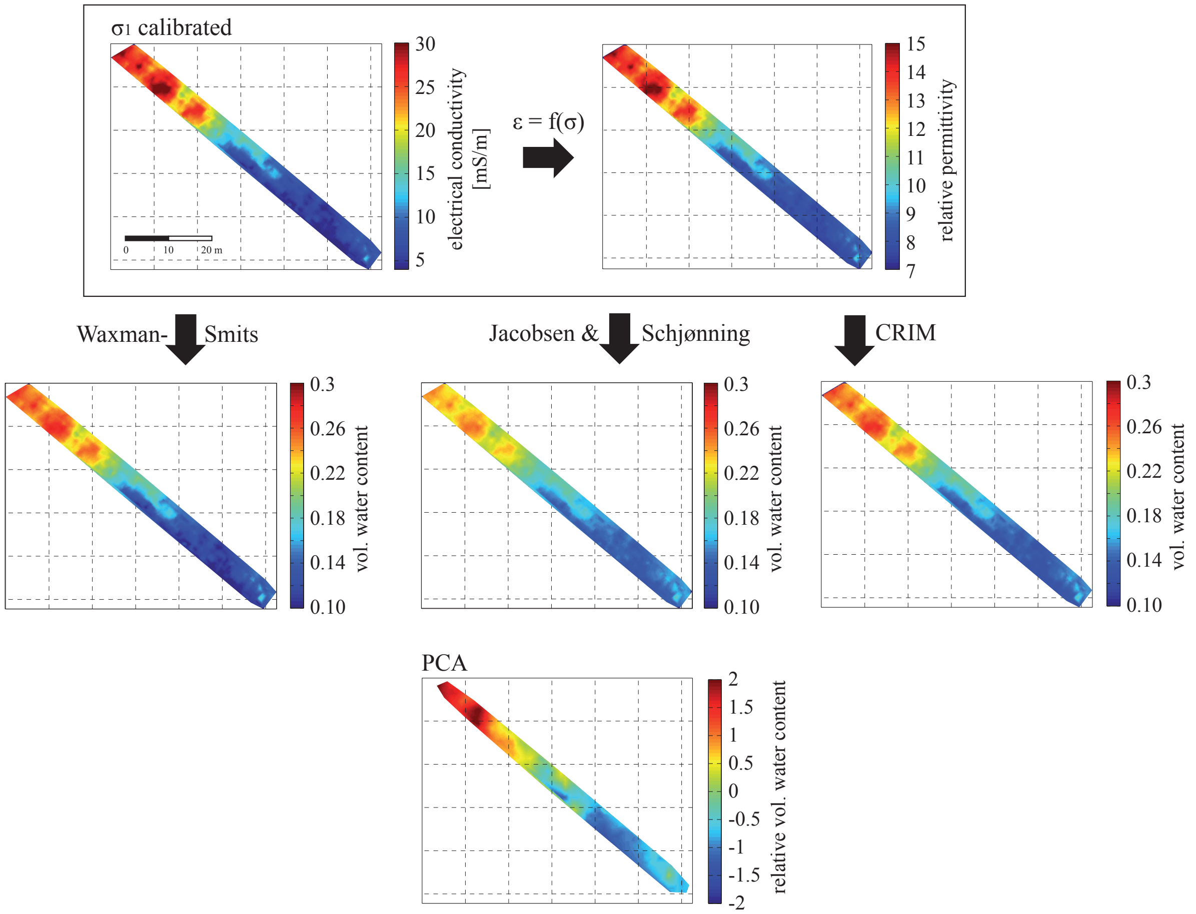

Fig. 6.3: Resulting maps of water content derived from electrical conductivity and permittivity using empirical and volumetric mixing formulas. For comparison the resulting map of the relative water content distribution from PCA is shown.

Unfortunately, the Lany dataset has only little overlapping of measured EMI and GPR data (see Q-map in Fig. 6.5). The map of the quality factor derived from GPR measurements shows a mean value of ≈ 8.6, which is in good agreement with the range found in laboratory measurements for this plot (Q = 6.6-10 for water contents between 0.03-0.18). The outliers result from the small fitting range of the instantaneous frequency. Although the instantaneous frequency traces have not been filtered after their seismic unix calculation, they does not look too noisy (Fig. 6.6). To smooth the data the traces have been spatially averaged over 1m (≈ 50 traces). The resulting imaginary part of relative permittivity is in the range 0-1.6, with very low values in the northwest and highest values in the middle part (Fig. 6.5). The calculated clay content shows very low values close to zero in the northwest, which mainly results from outliers in the quality factor and is not assumed to represent reality. The southeastern part has clay contents between 10-60 % with sharp discontinuities in-between. The representative sample of this plot had a clay content of 25 %, which is only rarely determined. The relative clay content distribution derived from PCA shows only weak correlation with the absolute clay content map. Nevertheless, in this case I assume the relative distribution from the PCA to yield the most reliable result, because the calculation of the clay content distribution from complex permittivity is

highly susceptible to small variations in Q, which is in turn prone to noise. An additional reason is that the water content distribution from PCA seems to be feasible and thus the clay content distribution should be too (under the assumptions made in chapter 5).
The adjacent step in Fig. 6.4 to determine a water content map is not practical due to the above-mentioned problems regarding outliers and noise and is thus not shown here.

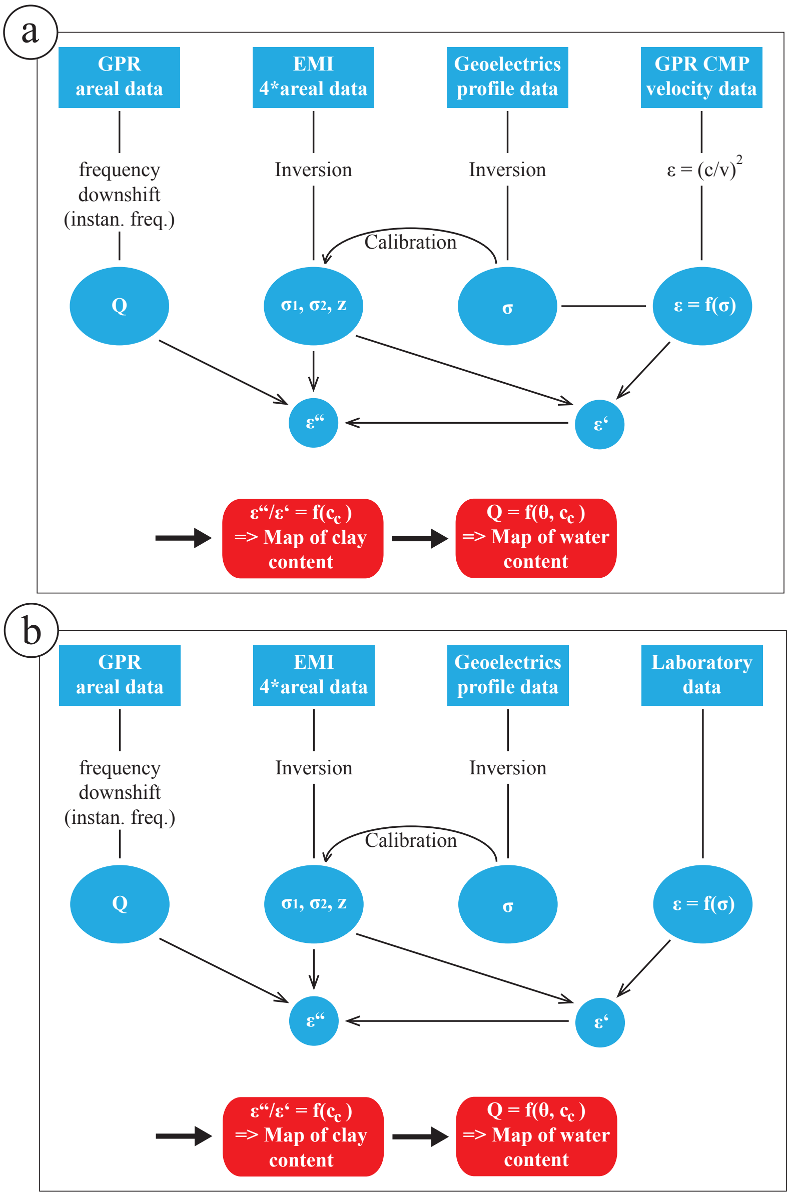

Fig. 6.4: Schematics for the derivation of clay and water content maps from field data (a), optionally using additional information from laboratory measurements (b).

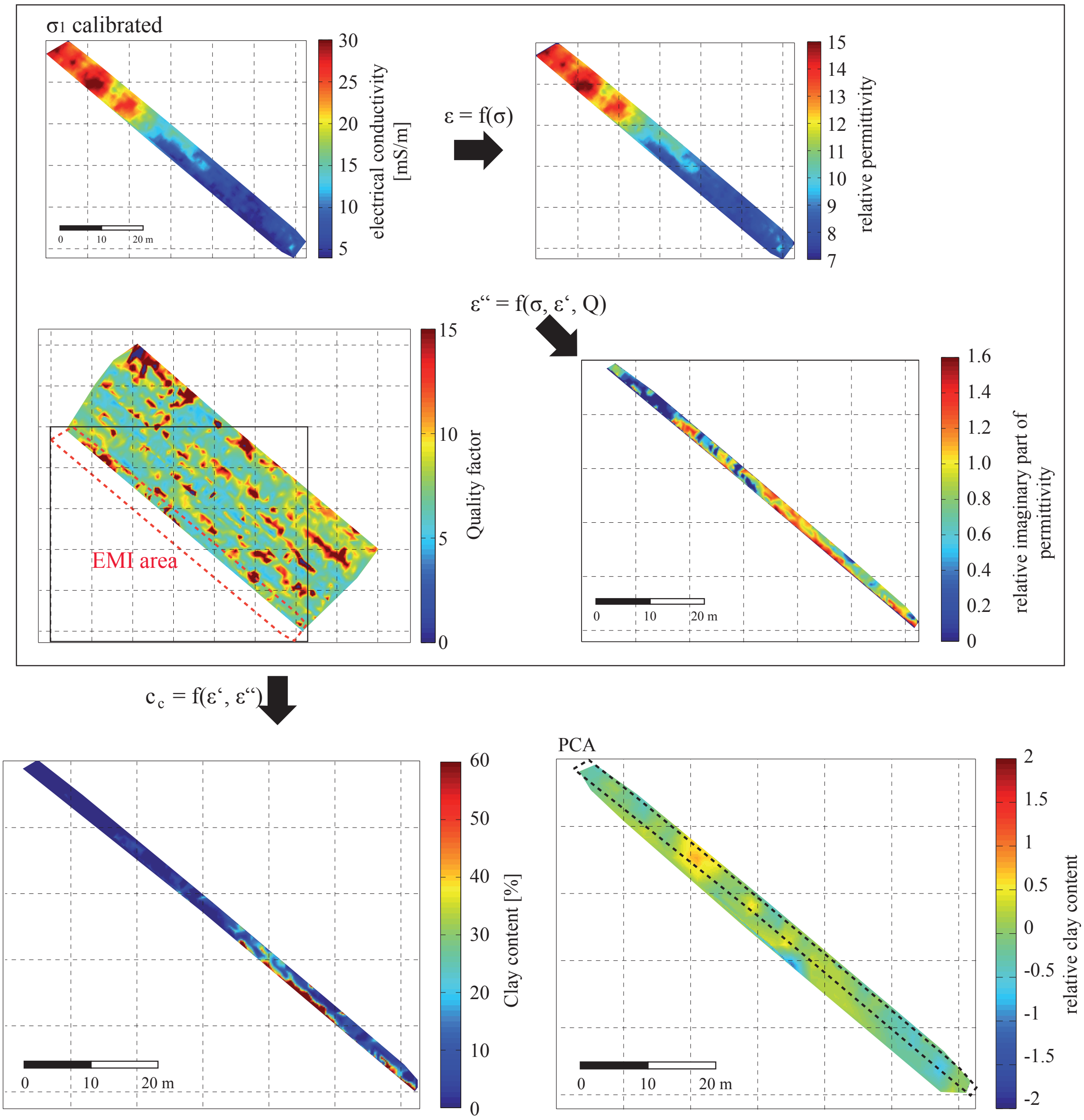

Fig. 6.5: Resulting map of the clay content derived from EMI and GPR field data. For comparison the resulting map of the relative clay content distribution from PCA is shown.

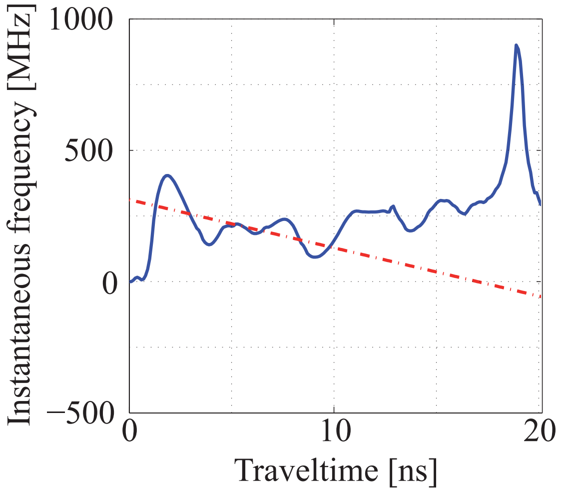

Fig. 6.6: Instantaneous frequency (blue, calculated with Seismic Unix, SU) and fitted linear function between 2 and 10 ns (red dashed).

7. Summary and outlook

As mentioned in the introduction, in agriculture it is important to know the sources of small-scale variability of the soil leading to spatially changing yield. These sources could be e.g. varying clay and water content. Using multi-sensor platforms to conduct high-resolution geophysical measurements large fields can be measured time and cost efficiently. The task is then to transform the spatial variability in geophysical parameters to a variability in soil parameters such as clay and water content. The aim of the work at hand was the development and enhancement of geophysical processing techniques for mapping of clay and water content.

7.1 Summary

GPTFs to link electrical conductivity and permittivity to water content

With respect to the application and comparison of GPTFs there are several functions available in literature relating electrical conductivity and permittivity to water and partly clay content. I focused on the comparison between six empirical, three volumetric mixing formulas and five effective medium models that include pore-scale geometrical features. To evaluate the quality of the predicted water content using these formulas, laboratory measurements under controlled conditions were performed. To investigate also the effect of different clay contents, several soil textures were used. The results showed that for permittivity the simple volumetric mixing formulas gave only slightly worse RMS errors than the more complicated effective medium models. Even the empirical models gave acceptable predictions of water content with partly absolute RMS errors below 0.026. An evaluation of the significance using the F-test showed that several models gave comparable results. For the electrical conductivity the empirical models gave the best results, nevertheless several fitting parameters have to be determined, which is not possible unambiguously. On one hand these findings show that the laboratory measurements were not distorted by mixing and refilling of the soil samples, because the measured values agree with models that were derived from measurements under undisturbed conditions. On the other hand the results confirm the usefulness of the simpler models regarding the reliable prediction of water content. This supports the wide application of these models in soil science. A special case is an effective medium model that describes permittivity and electrical conductivity with the same parameterisation. Although the resulting RMS errors in the prediction of water content were not as good as for the other models, it still yields satisfying agreement between measurements and models. This model can be used to determine e.g. the permittivity if only the electrical conductivity is known. Using laboratory data this worked well, whereas the application to field data strongly under-estimated the permittivity. This means that this sort of application suffers from the violation of underlying assumptions, such as constant porosity or constant clay content. Another approach to predict the permittivity and hence the velocity distribution from a geoelectric profile is the application of a linear relationship between permittivity and electrical conductivity that was observed in laboratory data. It was successfully applied to field data and the resulting velocity distribution showed good agreement to in situ measured CMPs. If no laboratory measurements about the soil at hand are available, the linear relationship can be established using an inverted geoelectric profile and CMP velocity measurements. The resulting velocity distribution of relatively high resolution (compared to single CMP measurements) can be used for migration of radargrams. Nevertheless, this is only useful for strong lateral velocity contrasts. In most cases the application of a one-dimensional or even constant velocity model for the migration is sufficient. Another application of the linear relationship is the conversion of an electrical conductivity map into a map of permittivity, which is discussed later.

Influence of water and clay content on the shape and amplitude of GPR signals

In addition to electrical conductivity and permittivity, the waveforms of GPR reflections were investigated. Their amplitude and shape is strongly dependent on water and clay content. Investigating the reflections in frequency domain in comparison to a reference wavelet reveals a frequency downshift due to attenuation, which can be described with a simple theoretical model. From the spectral ratio of reference and reflection the quality factor Q was determined, which is a measure of the ratio of energy gained and lost. It can be described as a logarithmic function of water and clay content. From this factor the imaginary part of permittivity was derived that represents the energy loss by polarisation relaxation. The relationship between real and imaginary part of permittivity can be described by a linear function. Its slope is only dependent on the clay content. Thus it might be possible to calculate the clay content of a soil if both parts of permittivity are known. This implies for the application to field data that measurements of electrical conductivity, measurements of GPR velocity (to give the real part of permittivity) and measurements of the frequency behaviour of GPR signals (to give the quality factor and thus the imaginary part of permittivity) are needed.

Areal mapping of the electrical conductivity of two layers

Areal mapping of the electrical conductivity, as the basis for the field application of GPTFs, is frequently done using the EM38DD, which measures the apparent electrical conductivity. This is an integrative value over the depth interval between 0 to about 1.5 m depth. Using an inversion procedure it is possible to derive the electrical conductivity of the topsoil layer, which is of most importance to cultivation of crops, the electrical conductivity of the second layer and the depth of the interface between layers. To control the reliability of different inversion approaches synthetic data have been used first. Four observed parameters are needed, which are the apparent electrical conductivities measured in two coil orientations and two heights above ground. Additional a priori information, e.g. the first layer thickness from GPR measurements, can be used to constrain the inversion. Here the reliability and truth of the a priori information as well as the assignment of a weighting factor are of importance. The application to field data yielded good results for sites with a clear conductivity contrast between topsoil and lower layer, whereas ramplike and smooth profiles could not be resolved by the inversion. A further problem is the inversion of topsoil layers thicker than about 1 m, due to the limited sensitivity of the EM38DD in this depth. The successful inversion result was validated by an inverted geoelectric profile showing approximately the same depth of the interface between layers and also the same trends in electrical conductivities of both layers. Nevertheless, the absolute conductivity values between EMI inversion result and geoelectric profile were not comparable. This is not a problem of the inversion, but a general problem of the EM38DD device and its calibration. However, the resulting layer conductivities can be successfully re-calibrated after the inversion using a geoelectric profile. The outcome of this part is the areal mapping of the electrical conductivities of topsoil and subsoil that is a basis for the field application of GPTFs.

Separation of the influences of water and clay content on the electrical conductivity
The electrical conductivity is influenced by several factors, such as clay and water content as main contributors. This means that the observed spatial variability of the electrical conductivity on a field site cannot be uniquely translated into a variation in neither clay content nor water content. To separate the influences of clay and water content in the spatial patterns of the electrical conductivity two decomposition approaches were applied. Additional to the electrical conductivity the radioelement concentrations of Uranium and Thorium are needed. These γ-concentrations are assumed to be dependent on clay content only. The resulting dataset of three variables was decomposed into principal components and so-called eigenimages. Assuming that the electrical conductivity is positively influenced by both clay and water content and the concentrations of Urianum and Thorium are only dependent on the clay content, positively correlating eigenimages were summed to yield the spatial distribution of the clay content. Negatively correlating eigenimages were assigned to the spatial distribution of the water content. For validation of the water content five TDR measurements were available, showing good agreement, but of course this is not significant and has to be verified in the future using additional datasets. To investigate the reliability of the resulting clay content maps I derived the clay content directly from γ-concentrations using a linear regression between Th and clay content. The resulting clay content map shows good agreement to the PCA-based map for Rosslau. In Lany the comparison is bad and only some features are coincident. This comparison might show that there are further mechanisms or dependencies that are not taken into account until now.
The second approach, the independent component analysis, gave similar spatial patterns, but these could not be uniquely assigned to water or clay content due to sparse output information from the algorithm. Additionally, one condition of ICA, the non-Gaussianity of the data, was violated for part of the dataset. Thus the ICA is not feasible for this application.

Application approaches for pedological mapping with geophysical methods
A map of electrical conductivity is the basis for all field applications of the GPTFs. This can be achieved relatively fast with an EM38DD survey. For reliable conductivity values at least one geoelectric profile should be measured in addition and used for re-calibration of the inverted layer conductivities. Using the layer conductivities instead of the measured apparent conductivity has the further advantage that the resulting maps can be assigned to a certain depth interval, e.g. the topsoil only. The second parameter that is needed for the application of GPTFs is the permittivity. To get a map of permittivity the linear relationship between conductivity and permittivity is needed that can be established through CMP velocity measurements and a geoelectric profile or taken from laboratory measurements. With this the map of the topsoil conductivity can be transformed into a map of permittivity of the upper layer.
Application of the tested GPTFs on either conductivity or permittivity map yields a map of the water content. A comparison of several methods had shown that the water content can be predicted reliably on field scale. The difference of water content between different approaches

is maximal 10 %.

For the calculation of a clay content map the linear relationship between real and imaginary part of permittivity can be used. To obtain the imaginary part of permittivity, the areal determination of the quality factor is needed. The quality factor can be determined from continuous zero-offset data using the downshift of the instantaneous frequency. This is not an easy task, because the determination of the instantaneous frequency includes a derivative, which amplifies potentially existing noise and thus has to be processed with care. The filtering process and the investigated time window strongly influence the resulting quality factor as well as the uncertainty concerning the source wavelet. An application to field data showed that the resulting map of clay content is not reliable due to the above-mentioned problems in determining the quality factor.

Concluding remark

The work at hand shows that it is possible to convert high-resolution maps of geophysical parameters into maps of water content using so-called GPTFs. A qualitative determination of a clay content map using PCA is also feasible in some cases. However, for verification of the results ground-truthing at several locations is necessary. This includes the drilling of shallow boreholes to measure the electrical conductivity as a function of depth, the sampling for texture analysis or measuring the water content in-situ by TDR. Nevertheless, the time and cost savings in comparison to conventional extensive soil sampling are high and the resulting high-resolution maps of soil parameters could not be achieved through conventional soil sampling alone.

7.2 Outlook

Although several approaches for pedological mapping using geophysics were introduced, some points remain for further investigation:

(1) Although the laboratory measurements were conducted on a large range of soil textures, the results does not necessarily have to be valid for all soil types. Even different types of clay minerals might be important that were not investigated in this study.

(2) A problem for the determination of the quality factor is the choice of a proper reference wavelet. This is independent of the method (i.e. spectral ratio method or the downshift of the instantaneous frequency). In this study the first derivative of the airwave was used, which does not account for coupling effects. This problem will in particular arise for different antennas, for which the validity of the results has to be tested.

(3) There seem to be unknown mechanisms or dependencies between electrical conductivity, γ-radiation and water and clay content. This might be also dependent on soil type, which is indicated through the use of different radioelements for the correlation with clay content in literature.

(4) The areal determination of Q using the downshift of the instantaneous frequency suffers from the noisy appearance of the instantaneous frequency. Thus the slope of the frequency downshift (and with that Q) is strongly dependent on filtering and the time window used for fitting.

List of abbreviations and symbols

Abbreviations

CEC	Cation exchange capacity
CMP	Common midpoint
C_{org}	Organic carbon content
CRIM	Complex refractive index model
DC	Direct current
DR	Dose Rate
EEG	electroencephalographic
EI	Eigenimage
EMI	Electromagnetic induction
FeC	Fe content
GPR	Ground Penetrating Radar
GPS	Global positioning system
GPTF	Geophysical pedotransfer function
HSL	Hashin-Shtrikman lower bound
HSU	Hashin-Shtrikman upper bound
IC	Independent component
ICA	Independent component analysis
JADE	Joint approximative diagonalisation of eigenmatrices
K	Potassium
LIN	Low induction number
PC	Principal component
PCA	Principal component analysis
RMS	Root mean square
RMSE	Root mean square error
SIP	Spectral induced polarisation
SVD	Singular value decomposition
TDR	Time domain reflectometry
TDS	Total dissolved solids
Th	Thorium
U	Uranium
UFZ	Helmholtz Centre for Environmental Research
VSP	Vertical seismic profiling

Symbols

A	GPR: Amplitude, else: Surface area
α	GPR: Attenuation exponent, else: Mixing exponent
B	EMI: Induction number, else: Equivalent ionic conductance
c	Velocity of light
c_c	Clay content
δ	Skin depth
ε	Dielectric permittivity
f	Frequency
γ	GPR: Width of the Gauss-curve, else: gamma
H	Magnetic field
I	Current
κ_h	Hydraulic permeability
L	Depolarization factor
m	Cementation exponent
μ	Magnetic permeability
n	Saturation exponent
Φ	Porosity
Q	Quality factor
Q_v	Cation exchange capacity (CEC)
R	EMI: Cumulative response, else: Correlation coefficient
ρ	Electrical resistivity
ρ_b	Dry bulk density
S	Saturation

s	Coil spacing
σ	Electrical conductivity
Δt	Traveltime difference
θ	Volumetric water content
T	Temperature
U	Voltage
V	Volume
v	Velocity
η	Volume fraction
w	Regularisation parameter, weight
ω	Angular frequency
z	Depth

Subscripts

a	Air
b	Bulk
d	Dispersed phase
ef	Effective
gr	Grain
p	Pore
r	Relative
s	Solid
w	Water

Bibliography

Abadpour, A., Kasaei, S. (2008): Color PCA eigenimages and their application to compression and watermarking. Image and Vision Computing, 26, 878-890

Archie, G.E. (1942): The electrical resistivity log as an aid in determining some reservoir characteristics. Transactions AIME, 146, 54-62

Arogunjo, A.M., Farai, I.P., Fuwape, I.A. (2004): Dose rate assessment of terrestrial gamma radiation in the delta region of Nigeria. Radiation Protection Dosimetry, Vol. 108, No. 1, 73-77

Bano, M. (1996): Constant dielectric losses of ground-penetrating radar waves. Geophys. J. Int., 124, 279-288

Bano, M. (2004): Modelling of GPR waves for lossy media obeying a complex power law f frequency for dielectric permittivity. Geophys. Prosp., 52, 11-26

Barnes, A.E. (2007): A tutorial on complex seismic trace analysis. Geophysics, Vol. 72, No. 6, W33-W43

Bartlett, M.S., Movellan, J.R., Sejnowski, T.J. (2002): Face recognition by independent component analysis. IEEE Trans. on Neural Networks, Vol. 13, 6, 1450-1464

Bath, M. (1974): Developments in solid Earth geophysics 7, Spectral Analyses in Geophysics, Elsevier Scientific Publication Company, 563

Berg, C.R. (1995): A simple, effective-medium model for water saturation in porous rocks. Geophysics, 60, 1070–1080

Birchak, J.R., Gardner, C.G., Hipp, J.E., Victor, J.M. (1974): High dielectric constant microwave probes for sensing soil moisture. Proc. IEEE, 62(1), 93–98

Bitri, A., Grandjean, G. (1998): Frequency-wavenumber modeling and migration of 2D GPR data in moderately heterogeneous dispersive media. Geophys. Prosp., 46, 287-301

Borchers, B., Uram, T., Hendrickx, J.M.H. (1997): Tikhonov Regularization of Electrical Conductivity Depth Profiles in Field Soils. Soil Sci. Soc. Am. J., 61, 1004-1009

Bradford, J.H., Harper, J.T., Brown, J. (2009): Complex dielectric permittivity measurements from ground-penetrating radar data to estimate snow liquid water content in the pendular regime. Water Resources Res., Vol. 45, W08403

Bronstein, I.N., Semendjajew, K.A., Musiol, G., Mühlig, H. (2001): Taschenbuch der Mathematik. Verlag Harri Deutsch, Thun und Frankfurt am Main

Brovelli, A., Cassiani, G. (2008): Effective permittivity of porous media: a critical analysis of the complex refractive index model. Geophys. Prosp., 56, 715-727

Brovelli, A., Cassiani, G. (2010): A combination of the Hashin-Shtrikman bounds aimed at modelling electrical conductivity and permittivity of variably saturated porous media. Geophys. J. Int., 180, 225-237

Bruggeman, D.A. (1935): Berechnung verschiedener physikalischer Konstanten von heterogenen Substanzen. Annalen der Physik, 24, 5, 636–664

Bussian, A.E. (1983): Electrical conductance in a porous medium. Geophysics, Vol. 48, No. 9, 1258-1268

Cardoso, J.F., Souloumiac, A. (1993): Blind beamforming for non-Gaussian signals. IEE-Proceedings-F, Radar and Signal Proc., Vol. 140, No. 6, 362-370

Cole, K.S., Cole, R.H. (1941): Dispersion and absorption in dielectrics. J. Chem. Phys., 9, 341-351

Comon, P. (1994): Independent component analysis, A new concept? Signal proc., 36, 287-314

Corwin, D.L., Lesch, S.M. (2005): Apparent soil electrical conductivity measurements in agriculture. Computers and Electronics in Agriculture, 46, 11–43

Dai, R., Young, C.T. (1997): Transient Fields of a Horizontal Electric Dipole on a Multilayered Dielectric Medium. IEEE Trans. on antennas and propagation, Vol. 45, No. 6, 1023-1031

De Groot, A.V., van der Graaf, E.R., de Meijer, R.J., Maucec, M. (2009): Sensitivity of in-situ γ-ray spectra to soil density and water content. Nuclear Instruments and Methods in Phys. Res., A600, 519-523

Deidda, G.P., Bonomi, E., Manzi, C. (2003): Inversion of electrical conductivity data with Tikhonov regularization approach: some considerations. Annals of Geophysics, Vol. 46, No. 3, 549-558

Delorme, A., Makeig, S. (2004): EEGLAB: an open source toolbox for analysis of single-trial EEG dynamics including independent component analysis. J. of Neuroscience Methods, Vol. 134, 1, 9-21

Dobson, M.C., Ulaby, F.T., Hallikainen, M.T., El-Rayes, M.A. (1985): Microwave dielectric behavior of wet soils: II. Dielectric mixing models. IEEE Trans. on Geoscience and Remote Sensing, 23, 35-46

Dunteman, G.H. (1989): Principal Components Analysis. Quantitative applications in the social sciences, Vol. 69, SAGE Publications, Inc.

Endres, A.L., Redman, J.D. (1996): Modelling the electrical properties of porous rocks soil containing immiscible contaminants. J. of Env. and Eng. Geophys., 1, 105-112

Feng, S., Sen, P.N. (1985): Geometrical model of conductive and dielectric properties of partially saturated rocks. J. of Applied Phys., 58, 3236-3243

Freire, S.L.M., Ulrych, T.J. (1988): Application of singular value decomposition to vertical seismic profiling. Geophysics, Vol. 53, No. 6, 778-785

Friedman, S.P. (2005): Soil properties influencing apparent electrical conductivity: a review. Computers and Electronics in Agriculture, 46, 45–70

Forbriger, T. (2003): Inversion of shallow-seismic wavefields: II—Inferring subsurface properties from wavefield transforms. Geophys. J. Int., 153, 735–752

Gebbers, R., Lück, E., Heil, K. (2007): Depth sounding with the EM38 - detection of soil layering by inversion of apparent electrical conductivity measurements. Precision agriculture, 95-102

Gränicher, W.H.H. (1994): Messung beendet - was nun? Hochschulverlag AG an der ETH Zürich und B.G. Teubner Stuttgart

Grandjean, G., Gourry, J.C., Bitri, A. (2000): Evaluation of GPR techniques for civil-engineering applications: study on a test site. J. of Appl. Geophys., 45, 141-156

Hanai, T. (1960): Theory of the dielectric dispersion due to the interfacial polarisation and its application to emulsions. Kolloid-Zeitschrift, 171, 23–31

Hansen, P.C. (2001): The L-curve and its use in the numerical treatment of inverse problems. Computational inverse problems in electrocardiology, WIT Press, Southampton, 119–142

Hashin, Z., Shtrikman, S. (1962): A variational approach to the theory of the effective magnetic permeability of multiphase materials. J. of Appl. Phys., 33 (10), 3125–3131

Hesselbo, S.P. (1996): Spectral gamma-ray logs in relation to clay mineralogy and sequence stratigraphy, cenozoic of the atlantic margin, offshore New Jersey. In: Proceedings of the Ocean Drilling Program, Scientific Results, Mountain, G.S., Miller, K.G., Blum, P., Poag, C.W., Twichell, D.C. (Eds.), Vol. 150, 411-422

Hendrickx, J.M.H., Borchers, B., Corwin, D.L., Lesch, S.M., Hilgendorf, A.C., Schlue, J. (2002): Inversion of Soil Conductivity Profiles from Electromagnetic Induction Measurements: Theory and Experimental Verification. Soil Sci. Soc. Am. J., 66, 673-685

Hilhorst, M.A. (2000): A pore water conductivity sensor. Soil Sci. Soc. Am. J., 64, 1922–1925

Hollender, F., Tillard, S. (1998): Modeling ground-penetrating radar wave propagation and reflection with the Jonscher parameterization. Geophysics, Vol. 63, No. 6, 1933-1942

Hyvärinen, A., Oja, E. (2000): Independent component analysis: algorithms and applications. Neural Networks, 13, 411-430

Irving, J.D., Knight, R.J. (2003): Removal of wavelet dispersion from ground-penetrating radar data. Geophysics, Vol. 68, No. 3, 960-970

Jackson, J.E. (1991): A User‘s Guide to Principal Components. John Wiley & Sons, Inc.

Jacobsen, O.H., Schjønning, P. (1993): A laboratory calibration of time domain reflectometry for soil water measurements including effects of bulk density and texture. J. of Hydrol., 245, 48-58

Jonscher, A.K. (1977): The ‘universal’ dielectric response. Nature, 267, 673-679

Kaarna, A. (2001): Integer PCA and wavelet transforms for multispectral image compression. IEEE International Geoscience and Remote Sensing Symposium, 1853-1855

Karlsen, B., Larsen, J., Sørensen, H.B.D., Jakobsen, K.B. (2001): Comparison of PCA and ICA based clutter reduction in GPR systems for anti-personal landmine detection. Proceedings of the 11th IEEE Signal Processing Workshop on Statistical Signal Processing, 146-149

Kitchen, N.R., Sudduth, K.A., Myers, D.B., Drummond, S.T., Hong, S.Y. (2005): Delineating productivity zones on claypan soil fields using apparent soil electrical conductivity. Computers and Electronics in Agriculture, Vol. 46, 285-308

Klitzsch, N. (2004): Ableitung von Gesteinseigenschaften aus Messungen der spektralen induzierten Polarisation (SIP) an Sedimentgesteinen. Dissertation, Leipzig University

Knight, R.J., Endres, A.L. (2005): Introduction to Rock Physics Principles for Near-Surface Geophysics. In Near Surface Geophysics, D.K. Butler, Ed. SEG, 31-70

Koefoed, O., Ghosh, D.P., Polman, G.J. (1972): Computation of type curves for electromagnetic depth sounding with a horizontal transmitter by means of a digital linear filter. Geophys. Prosp., 20, 406-420

Köster, H.W., Keen, A., Pennders, R.M.J., Bannink, D.W., de Winkel, J.H. (1988): Linear regression models for the natural radioactivity (238U, 232Th and 40K) in dutch soils: A key to anomalies. Radiation Protection Dosimetry, Vol. 24, No. 1-4, 63-68

Lesch, S.M., Corwin, D.L., Robinson, D.A. (2005): Apparent soil electrical conductivity mapping as an agricultural management tool in arid zone soils. Computers and Electronics in Agriculture, Vol. 46, 351-378

Lichtenecker, K., Rother, K. (1931) Die Herleitung des logarithmischen Mischungsgesetzes aus allgemeinen Prinzipien der stationären Strömung. Physikalische Zeitschrift, 32, 255-260

Linford, N. (2006): The application of geophysical methods to archaeological prospection. Reports on Progress in Physics, Vol. 69, 2205-2257

Liu, L., Lane, J.W., Quan, Y. (1998): Radar attenuation tomography using the centroid frequency downshift method. J. of Appl. Geophys., 40, 105-116

Loke, M.H. (2006): EM34 modeling program FreqEM. Geotomo Software, Malaysia (http://www.geoelectrical.com)

Loke, M.H. (2011): Res2DInv Manual: Rapid 2-D Resistivity & IP inversion using the least-squares method, Geotomo Software, Malaysia (http://www.geoelectrical.com)

Malicki, M.A., Walczak, R.T. (1999): Evaluating soil salinity status from bulk electrical conductivity and permittivity. Europ. J. of Soil Sci., 50, 505-514

McNeill, J.D. (1980): Electromagnetic terrain conductivity measurement at low induction numbers. Technical Note TN-6, Geonics Limited

Menke, W. (1989): Geophysical Data Analysis: Discrete Inverse Theory. International Geophysics Series, Vol. 45, Academic Press, Inc.

Mester, A., van der Kruk, J., Zimmermann, E., Vereecken, H. (2011): Quantitative two-layer inversion of multi-configuration electromagnetic induction measurements. Vadose Zone J., 10(4), 1319-1330

Nadler, A., Dasberg, S., Lapid, I. (1991): Time domain reflectometry measurements of soil water content and electrical conductivity of layered soil columns. Soil Sci. Soc. Am. J., 55, 938-943

Nüsch, A.K., Dietrich, P., Werban, U., Behrends, T. (2010): Acquisition an reliability of geophysical data in soil science. 19th World Congress of Soil Science, Soil Solutions for a Changing World, 1–6 August 2010, Brisbane, Australia

Peplinski, N.R., Ulaby, F.T., Dobson, M.C. (1995): Dielectric Properties of Soils in the 0.3-1.3 GHz Range. IEEE Trans. on Geoscience and Remote Sensing, Vol. 33, Nor. 3, 803-807

Persson, M. (2002): Evaluating the linear dielectric constant-electrical conductivity model using time-domain reflectometry. Hydrol. Sci. J., 47, 2, 269-277

Petersen, H., Wunderlich, T., al Hagrey, S.A., Rabbel, W. (2012): Characterization of some Middle European soil textures by gamma-spectrometry. Journal of Plant Nutrition and Soil Science, submitted

Powers, M.H. (1997): Modeling frequency-dependent GPR. The Leading Edge, 1657-1662

Pracilio, G., Adams, M.L., Smettem, K.R.J., Harper, R.J. (2006): Determination of spatial distribution patterns of clay and plant available potassium contents in surface soils at the farm scale using high resolution gamma ray spectrometry. Plant and Soil, Vol. 282, 67-82

Press, W.H., Teukolsky, S.A., Vetterling, W.T., Flannery, B.P. (2002): Numerical Recipes in C++. Cambridge University Press, Cambridge

Roth, C.H., Malicki, M.A., Plagge, R. (1992): Empirical evaluation of the relationship between soil dielectric constant and volumetric water content as the basis for calibrating soil moisture measurements by TDR. J. of Soil Sci., 43, 1-13

Roth, K., Schulin, R., Flühler, H., Attinger, W. (1990): Calibration of time domain reflectometry for water content measurements using a composite dielectric approach. Water Resources Res., 26, 2267-2273

Saey, T., Simpson, D., Vermeersch, H., Cockx, L., Van Meirvenne, M. (2009): Comparing the EM38DD and DUALEM-21S sensors for depth-to-clay mapping. Soil Sci. Soc. Am. J., Vol. 73, No. 1, 7-12

Schwartz, R.C., Evett, S.R., Pelletier, M.G., Bell, J.M. (2009): Complex permittivity model for time domain reflectometry soil water content sensing: I. Theory. Soil Sci. Soc. Am. J., Vol. 73, No. 3, 886-897

Sen, P.N. (1981): Relation of certain geometrical features to the dielectric anomaly of rocks. Geophysics, Vol. 46, No. 12, 1714-1720

Sen, P.N., Scala, C., Cohen, M.H. (1981): A self-similar model for sedimentary rocks with application to the dielectric constant of fused glass beads. Geophysics, 46, 781-795

Spies, B.R., Frischknecht, F.C. (1991): Electromagnetic Sounding. In: Electromagnetic Methods in Applied Geophysics, Vol. 2, Nabighian, M.N. (Editor), Soc. of Exploration Geophysicists

Steelman, C.M., Endres, A.L. (2011): Comparison of petrophysical relationships for soil moisture estimation using GPR ground waves. Vadose Zone J., 10, 1-16

Taner, M.T., Koehler, F., Sheriff, R.E. (1979): Complex seismic trace analysis. Geophysics, 44, 1041-1063

Taylor, M.J., Smettem, K., Pracilio, G., Verboom, W. (2002): Relationships between soil properties and high-resolution radiometrics, central eastern wheatbelt, Western Australia. Exploration Geophys., Vol. 33, No. 2, 95-102

Taylor, S., Barker, R. (2006): Modelling the DC electrical response of fully and partially saturated Permo-Triassic sandstone. Geophys. Prosp., 54, 351-367

Tonn, R. (1988): Die Bestimmung der seismischen Güte Q: Ein Vergleich unterschiedlicher Berechnungsmethoden. PhD Thesis, University of Kiel, Germany

Tonn, R. (1991): The determination of the seismic quality factor Q from VSP data: A comparison of different computational methods. Geophys. Prosp., 39, 1-27

Topp, G.C., Davis, J.L., Annan, A.P. (1980): Electromagentic determination of soil water content: Measurements in coaxial transmission lines. Water Resources Res., 16, 574-582

Turner, G., Siggins, A.F. (1994): Constant Q attenuation of subsurface radar pulses. Geophysics, Vol. 59, No. 8, 1192-1200

Tzanis, A. (2010): matGPR Release 2: A freeware MATLAB® package for the analysis & interpretation of common and single offset GPR data, FastTimes, 15 (1), 17–43

Van der Klooster, E., van Egmond, F.M., Sonneveld, M.P.W. (2011): Mapping soil clay contents in Dutch marine districts using gamma-ray spectrometry. Europ. J. of Soil Sci., Vol. 62, 743-753

Van der Kruk, J., Slob, E. (2002): Effective Source Wavelet Determination. Proceedings 9th international conference on Ground Penetrating Radar, Santa Barbara, USA, April 29-May2, 2002, 144-149

Von der Osten-Woldenburg, H. (2005): Applications of Ground-Penetrating Radar, magnetic and electrical mapping, and electromagnetic induction methods in archaeological investigations. In: D. K. Butler, ed., Near-surface geophysics: SEG, 621–626

Vrabie, V.D., Mars, J.I., Lacoume, J.-L. (2004): Modified singular value decomposition by means of independent component analysis. Signal Processing, 84, 645-652

Wang, J.R., Schmugge, T.J. (1980): An empirical model for the complex dielectric permittivity of soils as a function of water content. IEEE Trans. on Geoscience and Remote Sensing, Vol. GE-18. No. 4, 288-295

Waxman, M.H., Smits, L.J.M. (1968): Electrical conductivities in oil-bearing shaly sands. SPE J. paper lX63A, SPE 42nd Annual Fall meeting Houston, 107-122

Worthington, P.F. (1993): The uses and abuses of the Archie equations, 1: The formation factor-porosity relationship. J. of Appl. Geophys., 30, 215-228

Yelf, R., Yelf, D. (2006): Where is True Time Zero? Electromagnetic Phenomena, Vol. 7, No. 1 (18), 159-163

Zhang, L., Hao, T., Jiang, W. (2009): Separation of potential field data using 3-D principal component analysis and textural analysis. Geophys. J. Int., 179, 1397-1413

Appendix

Point	Clay content [%]	K [%]	U [ppm]	Th [ppm]	Dose rate [nGy/h]
1	45.23	0.77	1.89	7.00	38.29
2	49.53	0.59	2.12	6.72	36.86
3	45.19	0.65	1.96	7.54	38.50
4	39.67	0.68	2.70	6.94	39.31
5	48.12	0.74	2.46	7.60	42.23
6	49.45	0.43	1.34	7.05	30.58
7	46.85	0.63	2.25	7.59	39.67
8	52.57	0.30	1.41	5.89	25.81
9	10.16	0.57	0.75	1.94	17.33
10	9.31	0.59	1.01	2.44	19.23
11	36.16	0.51	1.54	5.13	29.15
12	39.54	0.84	1.85	7.74	42.09
13	50.00	0.49	1.98	5.88	33.42
14	8.77	0.53	1.62	2.63	22.53
15	37.85	0.74	2.91	7.29	45.40
16	27.72	0.86	1.71	7.08	38.33
17	3.31	0.56	0.73	0.85	12.80
18	39.90	0.60	2.03	5.39	32.81
19	38.91	0.87	2.35	8.03	44.28
20	46.21	0.69	3.22	7.62	44.90
21	6.63	0.63	0.68	2.02	17.44
22	38.38	0.47	2.09	3.52	27.03
23	12.39	0.66	0.62	3.53	20.06
24	54.85	0.31	1.69	5.22	28.65
25	48.15	0.19	1.45	4.33	21.51
26	50.35	0.55	2.24	5.41	32.15
27	39.16	0.38	1.91	6.49	31.63
28	50.41	0.60	1.72	7.45	36.79
29	46.11	0.66	1.90	7.08	36.64
30	44.43	0.63	1.91	5.98	33.20
31	50.24	0.59	2.78	7.03	41.47
32	40.19	0.72	2.59	7.09	41.85
33	42.83	0.64	2.97	6.77	42.54
34	53.38	0.78	2.05	7.55	41.53
35	48.50	0.75	2.32	6.57	39.90
36	38.22	0.92	1.65	7.06	38.71
37	48.41	0.87	2.97	6.47	44.99
38	41.15	0.86	2.08	8.63	45.45
39	3.71	0.66	0.63	1.79	16.17

Tab. A1: Sampling points from Rosslau with clay content and γ-concentrations (cont. on next page)

Point	Clay content [%]	K [%]	U [ppm]	Th [ppm]	Dose rate [nGy/h]
40	52.52	0.42	1.49	4.50	28.18
41	45.14	0.41	2.24	6.04	33.15
42	41.25	0.60	2.39	5.21	35.38
43	32.51	0.63	1.77	3.15	25.65
44	44.65	0.78	2.24	8.31	43.28
45	45.92	0.81	1.84	7.92	41.44
46	38.33	0.69	2.71	7.06	41.94
47	39.94	0.93	2.18	7.90	44.93
48	39.16	0.94	2.15	6.90	41.73
49	4.53	0.65	0.88	1.34	16.71
50	42.84	0.72	2.91	7.21	43.23
51	39.68	0.62	2.42	7.47	41.17
52	46.91	0.47	2.23	5.09	31.33

(Tab. A1 continued)

Acknowledgement

First of all, I would like to thank Prof. Dr. Wolfgang Rabbel for his encouragement and motivation during this thesis. It was always very helpful to discuss new results and after the meetings my head was full of new ideas.

I would also like to thank Prof. Dr. Hans-Jürgen Götze for acting as co-referee.

The results of this study are based on hundreds of hours of measurements. These would not have been possible without the help of my colleagues in the iSOIL project Hauke Petersen, Michael Lay and Thorsteinn Gudjonsson. Thank you! Also thanks to Said Attia al Hagrey for inviting me to work in the iSOIL project.

Thanks to Dr. Harald Stümpel for changing his software every time I asked him for a new and very special version, for helpful discussions especially with respect to programming and data interpretation and of course for the tea in the morning!

I would like to thank Ercan Erkul, who always found time for me and my problems. Çok teşekkürler!

Thanks to Manfred Wenk for constructing the measurement equipment (such as the „Fallgewicht-Bodenverdichtungs-Stampfer“ or the „Backblech“).

I would like to thank my colleagues from the third and fourth floor for professional and non-professional distraction during lunchtime. Special thanks go to Katja and Eva who were always there for spontaneous discussions and to Dennis for thinking about my inversion problems.

I would like to thank Clemens for his encouragement and being there for me.

Thanks to my parents Elke and Uwe for their everlasting support and motivation.

iSOIL (Interactions between soil related sciences - Linking geophysics, soil science and digital soil mapping) is a Collaborative Project (Grant Agreement number 211386) co-funded by the Research DG of the European Commission within the RTD activities of the FP7 Thematic Priority Environment.

In addition I would like to thank the Helmholtz Centre for Environmental Research (UFZ) in Leipzig for lending GPR antennas and providing the texture analyses of the soil samples.

Curriculum vitae

Name: Tina Wunderlich
Date and Place of Birth: August 17, 1983 in Achim
Nationality: German

Education

1990-1994	Grundschule Hogenkamp, Oldenburg
1994-1996	Orientierungsstufe, Schulzentrum Eversten, Oldenburg
1996-2003	Gymnasium Eversten, Oldenburg
2003	Abitur
2003-2008	Study of Geophysics at Christian-Albrechts-University of Kiel
2008	Diploma (Thesis: ’Anwendung von Potentialmethoden zur Verbesserung des Nutzsignals und der Interpretation magnetischer Feldmessungen in der Archäometrie’)
since 2008	PhD student at Christian-Albrechts-University of Kiel

Hiermit erkläre ich, dass die vorliegende Arbeit abgesehen von der Beratung durch den Betreuer nach Inhalt und Form meine eigene Arbeit ist, die ich ohne unzulässige Hilfe Dritter und ohne Benutzung anderer als der angegebenen Hilfsmittel angefertigt habe. Die aus anderen Quellen direkt oder indirekt übernommenen Daten und Konzepte sind unter Angabe der Quelle gekennzeichnet.

Diese Arbeit wurde in gleicher oder ähnlicher Form keiner anderen Prüfungsbehörde vorgelegt oder veröffentlicht.

Die Arbeit entstand unter Einhaltung der Regeln guter wissenschaftlicher Praxis der Deutschen Forschungsgemeinschaft.

Tina Wunderlich